



TEZ ŞABLONU ONAY FORMU
THESIS TEMPLATE CONFIRMATION FORM

1. Şablonda verilen yerleşim ve boşluklar değiştirilmemelidir.
2. **Jüri tarihi** Başlık Sayfası, İmza Sayfası, Abstract ve Öz'de ilgili yerlere yazılmalıdır.
3. İmza sayfasında jüri üyelerinin unvanları doğru olarak yazılmalıdır. Tüm imzalar **mavi pilot kalemlerle** atılmalıdır.
4. **Disiplinlerarası** programlarda görevlendirilen öğretim üyeleri için jüri üyeleri kısmında tam zamanlı olarak çalıştıkları anabilim dalı başkanlığının ismi yazılmalıdır. Örneğin: bir öğretim üyesi Biyoteknoloji programında görev yapıyor ve biyoloji bölümünde tam zamanlı çalışıyorsa, İmza sayfasına biyoloji bölümü yazılmalıdır. İstisnai olarak, disiplinler arası program başkanı ve tez danışmanı için disiplinlerarası program adı yazılmalıdır.
5. Tezin **son sayfasının sayfa** numarası Abstract ve Öz'de ilgili yerlere yazılmalıdır.
6. Bütün chapterlar, referanslar, ekler ve CV sağ sayfada başlamalıdır. Bunun için **kesmeler** kullanılmıştır. **Kesmelerin kayması** fazladan boş sayfaların oluşmasına sebep olabilir. Bu gibi durumlarda paragraf (¶) işaretine tıklayarak kesmeleri görünür hale getirin ve yerlerini **kontrol edin**.
7. Figürler ve tablolar kenar boşluklarına taşmamalıdır.
8. Şablonda yorum olarak eklenen uyarılar dikkatle okunmalı ve uygulanmalıdır.
9. Tez yazdırılmadan önce PDF olarak kaydedilmelidir. Şablonda yorum olarak eklenen uyarılar PDF dokümanında yer almamalıdır.
10. Tez taslaklarının kontrol işlemleri tamamlandığında, bu durum öğrencilere METU uzantılı öğrenci e-posta adresleri aracılığıyla duyurulacaktır.
11. Tez yazım süreci ile ilgili herhangi bir sıkıntı yaşarsanız, [Sıkça Sorulan Sorular \(SSS\)](#) sayfamızı ziyaret ederek yaşadığınız sıkıntıyla ilgili bir çözüm bulabilirsiniz.

1. Do not change the spacing and placement in the template.
2. Write **defense**
3. **date** to the related places given on Title page, Approval page, Abstract and Öz.
4. Write the titles of the examining committee members correctly on Approval Page. **Blue ink** must be used for all signatures.
5. For faculty members working in **interdisciplinary programs**, the name of the department that they work full-time should be written on the Approval page. For example, if a faculty member staffs in the biotechnology program and works full-time in the biology department, the department of biology should be written on the approval page. Exceptionally, for the interdisciplinary program chair and your thesis supervisor, the interdisciplinary program name should be written.
6. Write **the page number of the last page** in the related places given on Abstract and Öz pages.
7. All chapters, references, appendices and CV must be started on the right page. **Section Breaks** were used for this. **Change in the placement** of section breaks can result in extra blank pages. In such cases, make the section breaks visible by clicking paragraph (¶) mark and **check their position**.
8. All figures and tables must be given inside the page. Nothing must appear in the margins.
9. All the warnings given on the comments section through the thesis template must be read and applied.
10. Save your thesis as pdf and Disable all the comments before taking the printout.
11. This will be announced to the students via their METU students e-mail addresses when the control of the thesis drafts has been completed.
12. If you have any problems with the thesis writing process, you may visit our [Frequently Asked Questions \(FAQ\)](#) page and find a solution to your problem.

Yukarıda bulunan tüm maddeleri okudum, anladım ve kabul ediyorum. / I have read, understand and accept all of the items above.

Name : Amirhossein
Surname : Fathipour
E-Mail : amirhossein.fathipour@metu.edu.tr
Date : 01/09/2022
Signature : _____

EXPERIMENTAL INVESTIGATION OF HEMODYNAMICS IN ABDOMINAL
AORTIC ANEURYSM

A THESIS SUBMITTED TO
THE GRADUATE SCHOOL OF NATURAL AND APPLIED SCIENCES
OF
MIDDLE EAST TECHNICAL UNIVERSITY

BY

AMIRHOSSEIN FATHIPOUR

IN PARTIAL FULFILLMENT OF THE REQUIREMENTS
FOR
THE DEGREE OF MASTER OF SCIENCE
IN
MECHANICAL ENGINEERING

SEPTEMBER 2022

Approval of the thesis:

**EXPERIMENTAL INVESTIGATION OF HEMODYNAMICS IN
ABDOMINAL AORTIC ANEURYSM**

submitted by **AMIRHOSSEIN FATHIPOUR** in partial fulfillment of the requirements for the degree of **Master of Science in Mechanical Engineering, Middle East Technical University** by,

Prof. Dr. Halil Kalıpçılar
Dean, Graduate School of **Natural and Applied Sciences** _____

Prof. Dr. M. A. Sahir Arıkan
Head of the Department, **Mechanical Engineering** _____

Prof. Dr. M. Metin Yavuz
Supervisor, **Mechanical Engineering, METU** _____

Examining Committee Members:

Assoc. Prof. Dr. Sezer Özerinç
Mechanical Eng, METU _____

Prof. Dr. M. Metin Yavuz
Mechanical Eng, METU _____

Prof. Dr. Murat Köksal
Mechanical Eng, Hacettepe University _____

Assist. Prof. Dr. Ali Karakuş
Mechanical Eng, METU _____

Assist. Prof. Dr. Altuğ Özçelikkale
Mechanical Eng, METU _____

Date: 01.09.2022

I hereby declare that all information in this document has been obtained and presented in accordance with academic rules and ethical conduct. I also declare that, as required by these rules and conduct, I have fully cited and referenced all material and results that are not original to this work.

Name Last name: Amirhossein Fathipour

Signature:

ABSTRACT

EXPERIMENTAL INVESTIGATION OF HEMODYNAMICS IN ABDOMINAL AORTIC ANEURYSM

Fathipour, Amirhossein
Master of Science, Mechanical Engineering
Supervisor: Prof. Dr. Mehmet Metin Yavuz

September 2022, 113 pages

Abdominal aortic aneurysm (AAA), the enduring enlargement of the aorta, is a serious clinical condition with a very high mortality rate when it ruptures. Even though the precise causes of the dilation and rupture mechanisms of the aorta are still unknown, flow-related structures inside the AAA, including vortex formations and wall shear stresses, are associated with these mechanisms. The present study aims to characterize the flow patterns and their evolutions in two aneurysm models, simplified elliptic geometry and patient-specific geometry, under physiological flows. For the characterization, an optical velocity measurement technique, 2-D planar Particle Image Velocimetry (PIV), was employed in an In-vitro physiological flow set-up. For the simple model, the center plane was used for the measurement plane, whereas for the patient-specific model, due to its complex geometry, the flow fields at three different planes were quantified. The phase-averaged velocity, vorticity, and swirling strength (λ_{ci}) contours were constructed along with the streamline patterns. The results indicate that a vortex ring and the formation of two additional vortical structures are apparent in the simplified aneurysm model during the physiological cycle. In the patient-specific aneurysm model, the flow is highly 3-D, and relatively weak vortex formations are evident without a clear indication of a vortex ring. Different recirculation regions at different instants of the physiological

cycle are also apparent. Further studies are needed for a complete understanding of flow structure in the patient-specific aneurysm model.

Keywords: Abdominal Aortic Aneurysm, Vortex, PIV (Max. 5 keywords)

ÖZ

ABDOMİNAL AORTİK ANEVRİZMADA HEMODİNAMİĞİN DENEYSEL İNCELENMESİ

Fathipour, Amirhossein
Yüksek Lisans, Makina Mühendisliği
Tez Yöneticisi: Prof. Dr. Mehmet Metin Yavuz

Eylül 2022, 113 sayfa

Aortun kalıcı genişlemesi olan abdominal aort anevrizması (AAA), yırtıldığında ölüm oranı çok yüksek olan ciddi bir klinik durumdur. Aortun genişleme ve yırtılma mekanizmalarının kesin nedenleri hala bilinmemekle birlikte, girdap oluşumları ve duvar kayma gerilmeleri dahil olmak üzere AAA içindeki akışla ilgili yapılar bu mekanizmalarla ilişkilidir. Bu çalışma, fizyolojik akışlar altında, basitleştirilmiş eliptik geometri ve hastaya özel geometri olmak üzere iki anevrizma modelinde akış paternlerini ve evrimlerini karakterize etmeyi amaçlamaktadır. Karakterizasyon için, bir in vitro fizyolojik akış düzeneğinde bir optik hız ölçüm tekniği, 2-D düzlemsel Parçacık Görüntü Hızı (PIV) kullanıldı. Basit model için, ölçüm düzlemi için merkez düzlem kullanılırken, hastaya özel model için karmaşık geometrisi nedeniyle, üç farklı düzlemdeki akış alanları ölçülmüştür. Faz ortalamalı hız, girdap ve dönme kuvveti (λ_{ci}) konturları, akım çizgisi desenleriyle birlikte oluşturulmuştur. Sonuçlar, fizyolojik döngü sırasında basitleştirilmiş anevrizma modelinde bir girdap halkasının ve iki ek girdap yapısının oluşumunun belirgin olduğunu göstermektedir. Hastaya özel anevrizma modelinde, akış yüksek oranda 3 boyutludur ve bir girdap halkasının açık bir göstergesi olmadan nispeten zayıf girdap oluşumları belirgindir. Fizyolojik döngünün farklı anlarında farklı devridaim bölgeleri de belirgindir. Hastaya özel

anevrizma modelinde akış yapısının tam olarak anlaşılması için daha ileri çalışmalara ihtiyaç vardır.

Anahtar Kelimeler: Abdominal Aort Anevrizması, Girdap, PIV

To my wife and my family

ACKNOWLEDGMENTS

This thesis has been conducted in collaboration with Qatar University under Qatar University International Research Collaboration Co-Funds (IRCC) Program (IRCC 2020-002).

I express my most profound appreciation to my supervisor, Prof. Dr. Mehmet Metin Yavuz, for his guidance, advice, criticism, encouragement, and insight in confronting obstacles and setbacks throughout this research.

I also would like to pay my eternal gratitude to my family for their unlimited support. Foremost, I wish to thank my wife, Sana Sadreddini. Words cannot express my gratitude for her support along this journey.

I would like to extend my sincere thanks to my friends in the laboratory group, significantly, Mehmet Anil Susar, Kerem Tuğ Gökçek, and Oğuzhan Yılmaz.

Lastly, I acknowledge Mr. Mehmet Özçiftçi for his technical assistance.

TABLE OF CONTENTS

ABSTRACT.....	v
ÖZ vii	
ACKNOWLEDGMENTS	x
TABLE OF CONTENTS.....	xi
LIST OF TABLES.....	xiii
LIST OF FIGURES	xiv
LIST OF ABBREVIATIONS.....	xviii
LIST OF SYMBOLS	1
1 INTRODUCTION	2
1.1 The aim of the study	3
1.2 The Outline of the Thesis.....	4
2 LITERATURE REVIEW	5
2.1 Abdominal Aortic Aneurysm.....	5
2.1.1 Rheology	9
2.1.2 Vessel Structure	11
2.1.3 Rupture and Statistics	12
2.1.4 Symptoms, Diagnosis, and Repair	13
2.2 Experimental setup.....	15
2.2.1 <i>in- Vitro</i> Phantom.....	15
2.2.2 Blood Mimicking Fluid.....	18
2.3 Determining Factors for Flow Structure	24
2.3.1 Reynolds Number	24

2.3.2	Womersley Number.....	24
2.4	Vortex Characterization of Flow	26
2.4.1	Streamlines	27
2.4.2	Vorticity Magnitude	28
2.4.3	Swirling Strength Criterion	29
2.5	Previous Investigations.....	31
3	EXPERIMENTAL SETUP AND MEASUREMENT TECHNIQUES	39
3.1	Flow Circulatory Setup.....	39
3.1.1	AAA models.....	41
3.1.2	Working fluid	43
3.2	Experimental Matrices.....	44
3.2.1	Measurement planes	44
3.2.2	Flow Arrangements	47
3.3	Pressure Measurements	49
3.4	Velocity Measurement System: Particle Image Velocimetry (PIV)	50
3.4.1	Phase Averaging Method	52
3.5	Processing and Post-Processing	54
4	RESULTS AND DISCUSSION.....	61
4.1	Simple Model	61
4.2	Patient-Specific Model	74
4.3	Comparison of flow characteristics is SM and PSM.....	106
5	CONCLUSION	107
5.1	Future work	108
	REFERENCES	109

LIST OF TABLES

TABLES

Table 2.1 Properties of water-glycerol-NaI and BMF [22]	21
Table 2.2 Features of the Newtonian solutions of Water-Glycerol with an additive of Urea and NaI with three different viscosity ranges [27].....	22
Table 3.1 Property of the blood mimicking fluid	43
Table 3.2 Flow properties	47
Table 3.3 Deformation amount of models under physiological flow conditions....	48

LIST OF FIGURES

FIGURES

Figure 1.1. Abdominal Aortic Aneurysm.....	2
Figure 2.1. Internal view of the heart	6
Figure 2.2. Pulmonary and Systemic Circulation.....	7
Figure 2.3. A) Aorta parts, B) TAA, C)AAA.....	8
Figure 2.4. Blood components.....	9
Figure 2.5. Effects of a different kind of exercise on blood viscosity measured at several shear rates in the same trained subject [6]	10
Figure 2.6. Three layers of the aorta.....	12
Figure 2.7. Endovascular surgery A: An artery in the groin is used to place a catheter (upper thigh). The stent graft is released from the catheter after it has been threaded to the abdominal aorta. B: Blood can pass through the aneurysm through the stent graft.	15
Figure 2.8. Lost-core casting- the casting box's surfaces are arranged in a way to increase optical access to vital areas [20].....	17
Figure 2.9. matching refractive index's impact on optical access, A)no match, B)close match, C)perfect match [22].....	18
Figure 2.10. The PDMS polymer (Sylgard 184) refractive indices of the samples with varied A: B mixed agent ratios: a) curing conditions at 65°C for two h, b) at room temperature for seven days [23].....	19
Figure 2.11. Oscillatory elasticity (a–c) and Oscillatory viscosity (d–f) were measured in the low, medium, and high water–glycerol ratios with the addition of urea and NaI. The xanthan gum concentrations were 0.02 (a–d), 0.04 (b–e), and 0.06 (c–f) [27].....	23
Figure 2.12. Velocity profiles of steady parabolic and plug-like flows and peak velocity profiles of five different Womersley flows [32].....	26
Figure 2.13. Streamline of a vortex in three different reference frames: a) vortex core, b) inside the core, c) out of the core [34].....	28

Figure 2.14. Swirling motion of the fluid [37].....	31
Figure 2.15. Complex flows at the anterior half of the infrarenal aorta [38].....	32
Figure 2.16. Velocity vectors in the bulge portion under a steady flow of $Re=1000$ [39].....	33
Figure 2.17. Dimensions of the glass AAA models [40].....	34
Figure 2.18. Flow progress during a cycle of physiological flow with $Re_{mean}=289$ and $\alpha=4.07$ in the model [40].....	34
Figure 2.19. AAA axisymmetric sylgard 184 model. Dimensions in mm [41].....	35
Figure 2.20. Axial velocity contours and streamline at steady flow a) $Re=584$ b) $Re=690$ [41].....	36
Figure 2.21. Plane definitions in the symmetric AAA model a)Vertical plane b)Horizontal plane [42].....	36
Figure 2.22. Comparison of the swirling strength (λ_{ci}) in rigid and compliant models in a) vertical plane, b) horizontal plane [42]	37
Figure 3.1. Schematic configuration of the setup in this study.....	40
Figure 3.2. Flow circulatory system in Fluid Mechanics Laboratory, METU	40
Figure 3.3. Dimension of the simple model (SM) in mm.....	41
Figure 3.4. The patient-specific model: upper: 3D view, lower: the schematic view, dimensions in mm	42
Figure 3.5. The simple model A) Empty B) Filled with blood mimicking fluid, The patient-specific model C) Empty D) Filled with blood mimicking fluid.....	44
Figure 3.6. Measurement plane at SM	45
Figure 3.7. Measurement planes at PSM	45
Figure 3.8. The measurement regions at PSM in; a)plane #1, b)plane #2, c)plane #3	46
Figure 3.9. Flow rates in the physiological flow of SM	47
Figure 3.10. Flow rates in the physiological flow of PSM	48
Figure 3.11. Pressure at the inlet (PT1) and outlet (PT2) in one cycle (1sec), SM	49
Figure 3.12. Pressure at the inlet (PT1) and outlet (PT2) in one cycle (1sec), PSM	50

Figure 3.13. Principle of planar PIV (2D PIV)	51
Figure 3.14. Measurement instants of physiological flow in SM.....	53
Figure 3.15. Measurement instants of physiological flow in PSM	54
Figure 3.16. A sample of raw image	55
Figure 3.17. The calibration reference in SM (inlet with a diameter of 18.4 mm) .	55
Figure 3.18. The sample image after background subtraction	56
Figure 3.19. The selected mask as the processing area	57
Figure 3.20. Particles in the interrogation area, two frames of an image pair.....	57
Figure 3.21. Velocity fields generated from an image pair	58
Figure 3.22. The averaged velocity map	59
Figure 4.1. Axial velocity contours at the acceleration part, SM	62
Figure 4.2. Axial velocity contours at the deceleration part, SM.....	64
Figure 4.3. Streamline patterns at the acceleration part, SM.....	65
Figure 4.4. Streamline patterns at the deceleration part, SM	67
Figure 4.5. Vorticity contours at the acceleration part, SM	68
Figure 4.6. Vorticity contours at the deceleration part, SM	69
Figure 4.7. Swirling strength (λ_{ci}) at the acceleration part, SM	71
Figure 4.8. Swirling strength (λ_{ci}) at the deceleration part, SM	72
Figure 4.9. a) Swirling strength of the flow filed in the first phase b) Q criteria of the flow filed in the first phase in SM	73
Figure 4.10. Axial velocity contours at the acceleration part, PSM, plane #1	75
Figure 4.11. Axial velocity contours at the deceleration part, PSM, plane #1	76
Figure 4.12. Streamline patterns at the acceleration part, PSM, plane #1	78
Figure 4.13. Streamline patterns at the deceleration part, PSM, plane #1	79
Figure 4.14. Vorticity contours at the acceleration part, PSM, plane #1	81
Figure 4.15. Vorticity contours at the deceleration part, PSM, plane #1	82
Figure 4.16. Swirling strength (λ_{ci}) at the acceleration part, PSM, plane #1	84
Figure 4.17. Swirling strength (λ_{ci}) at the deceleration part, PSM, plane #1	85
Figure 4.18. a) Swirling strength of the flow filed in the first phase b) Q criteria of the flow filed in the first phase in PSM.....	86

Figure 4.19. Axial velocity contours at the acceleration part, PSM, plane #2.....	88
Figure 4.20. Axial velocity contours at the deceleration part, PSM, plane #2	89
Figure 4.21. Streamline patterns at the acceleration part, PSM, plane #2	90
Figure 4.22. Streamline patterns at the deceleration part, PSM, plane #2	91
Figure 4.23. Vorticity contours at the acceleration part, PSM, plane #2	92
Figure 4.24. Vorticity contours at the deceleration part, PSM, plane #2.....	93
Figure 4.25. Swirling strength (λ_{ci}) at the acceleration part, PSM, plane #2.....	95
Figure 4.26. Swirling strength (λ_{ci}) at the deceleration part, PSM, plane #2.....	96
Figure 4.27. Axial velocity contours at the acceleration part, PSM, plane #3.....	98
Figure 4.28. Axial velocity contours at the deceleration part, PSM, plane #3	99
Figure 4.29. Streamline patterns at the acceleration part, PSM, plane #3	100
Figure 4.30. Streamline patterns at the acceleration part, PSM, plane #3	101
Figure 4.31. Vorticity contours at the acceleration part, PSM, plane #3	102
Figure 4.32. Vorticity contours at the deceleration part, PSM, plane #3	103
Figure 4.33. Swirling strength (λ_{ci}) at the acceleration part, PSM, plane #3	104
Figure 4.34. Swirling strength (λ_{ci}) at the deceleration part, PSM, plane #3.....	105

LIST OF ABBREVIATIONS

ABBREVIATIONS

AAA	Abdominal Aortic Aneurysm
TAA	Thoracic Aortic Aneurysm
WSS	Wall Shear Stress
RBC	Red Blood Cell
PDMS	Polydimethylsiloxane
BMF	Blood Mimicking Fluid
RI	Refractive Index
PIV	Particle Image Velocimetry
XG	Xanthan Gum
SM	Simple Model
PSM	Patient-Specific Model
Ph	Physiological
PT	Pressure Transducer
ILT	Intraluminal thrombus
Stk	Stokes number

LIST OF SYMBOLS

SYMBOLS

Re	Reynolds Number
$\mu(\dot{\gamma})$	effective fluid viscosity
μ_o	low shear viscosity
μ_∞	high shear viscosity
λ	shear time constant
η'	oscillatory viscosity
η''	oscillatory elasticity
u_m	average velocity at aneurysm inlet
D	diameter of the model at the inlet
μ	dynamic viscosity
ρ	density
ω	angular frequency
ω	vorticity vector
$x, y, \text{ and } z$	coordinates
$u, v, \text{ and } w$	velocity component
λ_{ci}	Swirling strength

CHAPTER 1

INTRODUCTION

The abdominal aortic aneurysm (AAA) refers to the expansion of the aorta at the abdomen part of the body, as shown in Figure 1.1, more than half of its standard diameter.

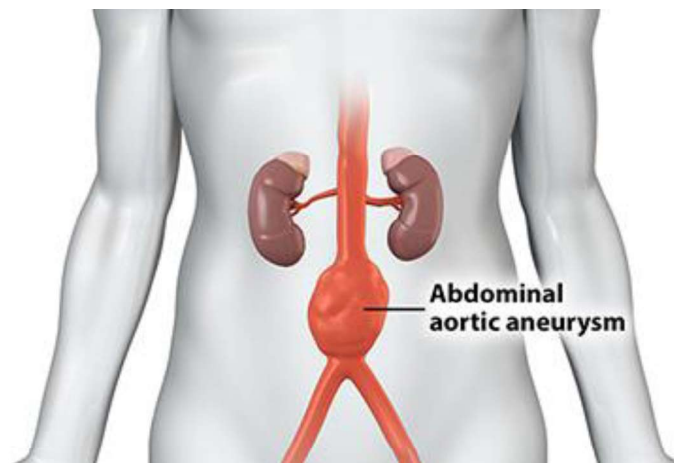


Figure 1.1. Abdominal Aortic Aneurysm

In some cases, if left untreated, the aneurysm can expand farther to the point of rupture. The aneurysm growth rate can predict the risk factor for patients. Aneurysm rupture is a catastrophic incident that leads to overall mortality of 80%. The biggest obstacle for this disease is its asymptomatic property; most cases are diagnosed by chance.

The leading causes of the aneurysms' creation, expansion, and rupture remain unrevealed. Some reported reasons can be related to smoking, age, sex, and family

background, but it is believed that the vessel's blood flow structure can help us develop our knowledge and treatment techniques further.

Intraluminal thrombus (ILT) is the blood clot that forms in the aneurysm. It is reported that rupture points in real cases are related to the locations with low wall shear stresses (WSS). These locations are also consistent with the formed thrombus zones [1]. The low shear stresses mainly occur in the areas where a vortex appears. The swirling motion of the fluid affects the velocity gradient distribution in the bulge. This effect makes the WSS and related indexes like time average WSS gradient and oscillatory shear index dependent on the formed vortical flow structure. Hence, identifying the whirling structures inside the aneurysm can assist us in understanding their effect on the hemodynamics in AAA.

1.1 The aim of the study

The purpose of the current research is to characterize the flow patterns and their changes in two aneurysm models: simple elliptic geometry and patient-specific geometry. For this matter, the planar Particle Image Velocimetry technique is employed to compute the velocity maps in the target planes.

The measuring plane for the simple model was the central plane, but because of its intricate geometry, the flow fields at three separate planes were measured for the patient-specific model. The constructed phase averaged velocities of the flow field, streamlines, vorticity magnitudes, and swirling strength criteria are studied to characterize the flow behaviors in these models. Moreover, a comparison is made between the applied Q criterion and the swirling strength criterion in the flow fields.

1.2 The Outline of the Thesis

This study includes five chapters.

The first chapter, “Introduction”, briefly explains the motivation and the aim of the study.

The second chapter, “Literature Reviews”, explains the abdominal aortic aneurysm. Then the blood mimicking fluid and the aneurysm phantoms are described. The flow parameters and vortex identification methods are also summarized. Finally, the results from previous studies are discussed.

The third chapter, “Experimental Set Up and Measurement Techniques”, explains the blood circulatory system and utilizes models and blood mimicking fluid in this study. The experimental matrices are also presented in detail.

The fourth chapter, “Results and Discussion”, includes the result of the experiments in detail. Streamline patterns and velocity, vorticity, and swirling strength(λ_{ci}) contours of the studied planes are presented, and the flow patterns are discussed in detail.

The fifth chapter, “Conclusion”, briefly states the findings of this investigation and suggests some future inquiries.

CHAPTER 2

LITERATURE REVIEW

This chapter summarizes the general problem and the previous studies about AAA and vortex identification methods.

2.1 Abdominal Aortic Aneurysm

The heart, blood vessels, and the approximately 5 liters of blood which the blood vessels convey make up the cardiovascular system. The movement of nutrients, cellular waste products, hormones, and oxygen throughout the body is the responsibility of this system [2].

The heart is a muscular pumping organ in the thoracic region of the body, medial to the lungs, and along the body's midline. The heart is rotated to the left at its lowest tip, or apex, so roughly two-thirds of it is on the left side of the body, and the other third is on the right. The base of the heart is placed at the top of the heart and is connected via the aorta, vena cava, pulmonary trunk, and pulmonary veins. Figure 2.1 shows the structure of the heart [3].

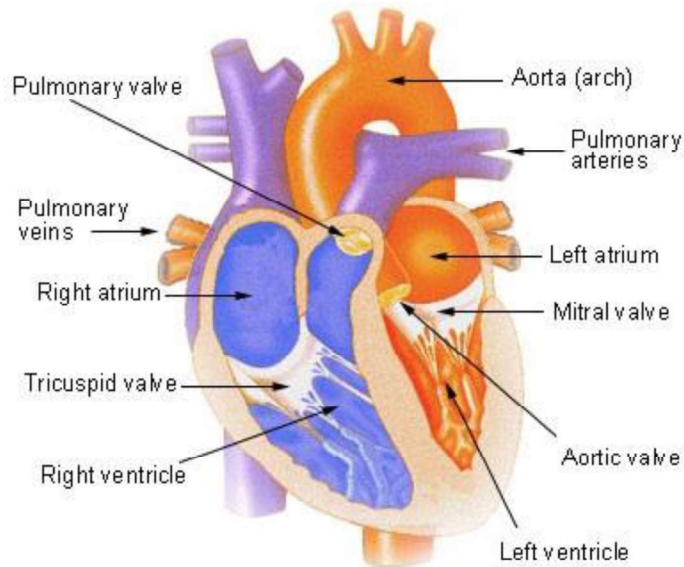


Figure 2.1. Internal view of the heart

The pulmonary and systemic circulation loop are the two main circulatory loops in the human body. The heart is about the size of a closed fist and drives the circulatory system; deoxygenated blood is sent from the right side to the lungs, picking up oxygen before returning to the left side of the heart. All of the body's tissues receive highly oxygenated blood through systemic circulation from the left side of the heart. Through systemic circulation, wastes from bodily tissues are eliminated, and deoxygenated blood is sent back to the right side of the heart. These loops are shown in Figure 2.2.

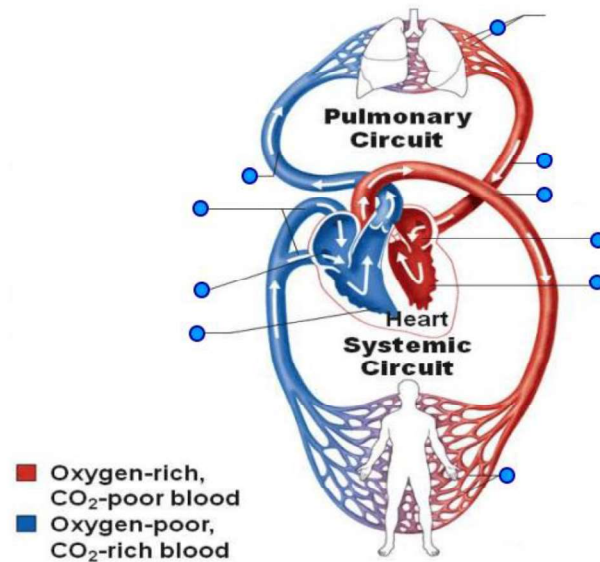


Figure 2.2. Pulmonary and Systemic Circulation

The blood vessels can generally be divided into arteries, which begin with the aorta and carry out the oxygen-rich blood away from the heart to all tissues, and capillaries, which are the thin and small blood vessels connecting Arteries and Veins and passing the necessary elements to organ's cells and take the waste products from them and Veins, which took the oxygen-poor and rich in waste blood back to the heart [4].

Aorta is the most prominent artery in the human body. Its diameter varies between 2-3 cm. It is divided into four parts; the ascending aorta, the aortic arch, the thoracic (descending) aorta, and the abdominal aorta [3].

An aneurysm is a weak spot in the blood vessel wall that causes an abnormal enlargement or ballooning of a section of an artery. Aneurysms can develop in various locations throughout your body, including the chest, abdomen, and brain.

Two different types of aortic aneurysm can occur:

- 1- Abdominal Aortic Aneurysm (AAA)
- 2- Thoracic Aortic Aneurysm (TAA)

Figure 2.3 exhibits our different sections of the aorta and the location of AAA and TAA

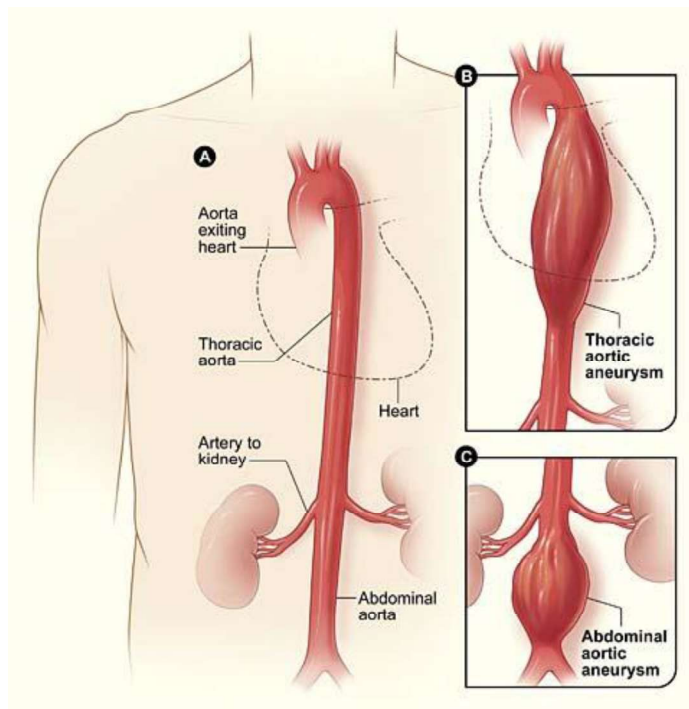


Figure 2.3. A) Aorta parts, B) TAA, C)AAA

Abdominal aortic aneurysms are aneurysms that develop in the aorta's portion that runs through the abdomen. Three out of every four aortic aneurysms are AAAs. Because computerized tomography scans are performed for other medical issues, they are discovered more frequently than in the past.

2.1.1 Rheology

Blood is a complex non-Newtonian fluid that exhibits various non-Newtonian rheological characteristics, including shear thinning, yield stress, and viscoelasticity [5]. Increasing the shear rate decreases the blood viscosity exponentially. This viscosity is affected by both hematocrit (Volume percentage of red blood cells (RBCs) in the blood) and plasma viscosity [6]. Plasma comprises 55% of the blood and 90% water. Figure 2.2 shows the components of human blood.

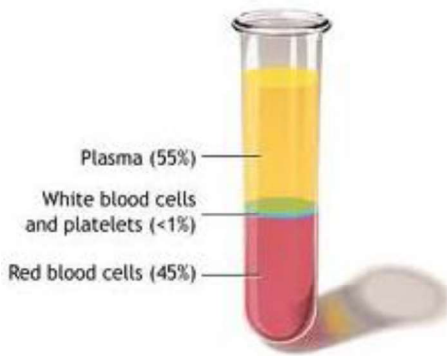


Figure 2.4. Blood components

Plasma is a Newtonian fluid, meaning its viscosity does not vary with shear rate [7], so the shear thinning effect is mainly caused by RBC rheological qualities. RBCs' deformable properties cause these qualities.

Some studies have investigated this property of the blood for different conditions. Nader et al. (2019) investigated the shear thinning behavior of the blood under other exercise cases. An increased heart rate due to exercise results in a rise in hematocrit. This rise also elevates blood viscosity.

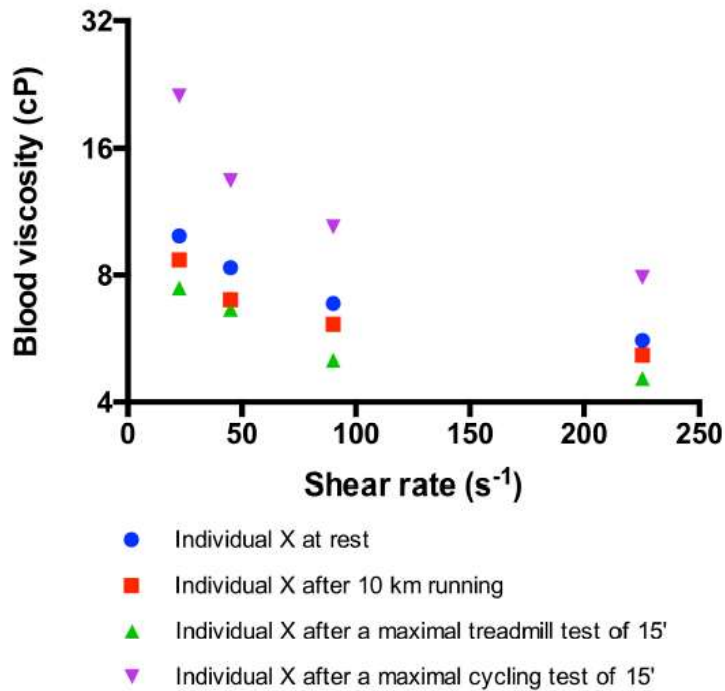


Figure 2.5. Effects of a different kind of exercise on blood viscosity measured at several shear rates in the same trained subject [6]

Figure 2.5. reveals the exponential decrease in shear rate under a reduction in blood viscosity [6]. This behavior is negligible above 300 s^{-1} shear rates.

Blood's non-Newtonian behavior is caused by various parameters like shear thinning, yield stress, and viscoelasticity. Different rheological models have been suggested to model blood rheology. One of these is the Cross model of shear thinning property of the blood was presented in 1979 [5]. This model can be formulated as equation (2.1):

$$\mu(\dot{\gamma}) = \mu_{\infty} + \frac{\mu_0 - \mu_{\infty}}{1 + (\lambda \dot{\gamma})^n} \quad (2.1)$$

Where :

$\mu(\dot{\gamma})$ is the effective fluid viscosity

μ_o is low shear viscosity,

μ_∞ is the high shear viscosity,

λ is the shear time constant,

And $n \in (0,1)$ is the power index with values less than unity, indicating shear thinning behavior [8].

Different non-Newtonian rheological behavior, and consequently different flow modeling approaches, should apply to the various parts of the circulatory system since the influence of the non-Newtonian effects largely relies on the form and size of the flow conduits. Small blood vessels, which typically encompass capillaries and potentially arterioles, large blood vessels, which mainly refer to arteries and veins, and porous tissue, which generally refers to the heart and muscles, are the parts that can be divided and investigated separately [5].

In large vessels, like the aorta, the blood's exposure to high shear rates decreases the non-Newtonian effects. So the blood acts like a Newtonian fluid [9].

2.1.2 Vessel Structure

Due to the deformation in the aorta in AAA, vessel structure in its layer changes. These layers are:

1. The adventitia, or outside layer, gives the vessel structure and shape.
2. The tunica medium, or middle layer, controls the vessel's internal diameter and comprises elastic and muscular tissue.
3. The tunic intima, an inner layer, is lined with endothelial cells, allowing blood to flow without resistance [10].

Figure 2.6 shows the orientation of these layers

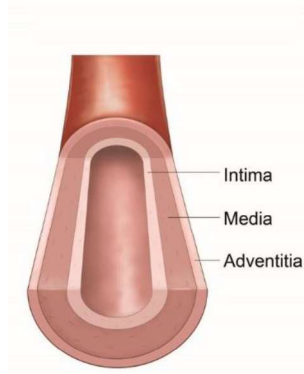


Figure 2.6. Three layers of the aorta

The disturbance in these layers, due to AAA, reduces the vessel wall resistance; hence, it can not adapt to the oscillation of physiological flow. This reduction increases the danger of rupture of the aneurysm.

2.1.3 Rupture and Statistics

Abdominal aortic aneurysm carries a risk of rupture if left untreated. The size, enlargement rate, continuous smoking, and chronic hypertension affect an aneurysm's propensity to rupture.

One of the best indicators of the likelihood of a rupture is the size of the aneurysm, with the risk rising sharply at aneurysm sizes bigger than 5.5 cm. Aneurysms bigger than 5.0 cm have an overall cumulative rupture rate of 25 percent to 40 percent over five years, compared to 1 percent to 7 percent for aneurysms 4.0 cm to 5.0 cm in diameter. An annual rupture rate risk according to AAA diameters is reposted as follows: [11]

- 0% at less than 4.0 cm
- 0.5% to 5% at 4.0-4.9 cm
- 3% to 15% at 5.0-5.9 cm
- 10% to 20% at 6.0-6.9 cm

- 20% to 40% at 7.0-7.9 cm
- 30% to 50% at 8.0 cm or more

After the age of 60, the risk of AAAs rapidly rises. Approximately 1% of males between the ages 55 and 64 have clinically significant aneurysms (greater than 4 cm in diameter), and the prevalence increases by 2% to 4% per decade. Men experience AAAs four to six times more frequently than women. Additionally, AAAs appear roughly ten years later in women than in men [12–14].

2.1.4 Symptoms, Diagnosis, and Repair

It can be challenging to diagnose abdominal aortic aneurysms because they frequently develop slowly and without apparent symptoms. Some aneurysms do not rupture. AAA, in many people, starts small and doesn't grow. Others expand over time, occasionally quickly. Below are some of the general symptoms [15]:

- Deep, constant pain in the belly area or side of the abdomen
- Back pain
- A pulse near the bellybutton

Accidental detection of the vascular disease accounts for 30% of cases during regular physical examinations when a pulsatile mass is present. Ultrasonography (USG), abdominal computed tomography (CT), and magnetic resonance imaging (MR) used for other purposes can also result in the unintentional discovery of some cases. Additionally, certain X-ray scans may identify calcification and covertly reveal the aneurysm. Even however, this method of identification is unreliable since not all aneurysm occurrences lead to sufficient calcification [11].

In the case of a large AAA, surgery to reinforce it with a piece of synthetic tubing (a graft) is typically advised because the risk of it bursting outweighs the risk of surgical complications.

For a AAA, there are two primary surgical approaches:

- Endovascular surgery: The graft is carefully passed up into the aorta after being implanted into a blood artery in the groin.
- Open surgery: Through a belly cut, the transplant is implanted in the aorta.

The chance of a AAA bursting can be reduced with either method, but each has advantages and disadvantages of its own.

Through tiny incisions in the groin, a stent graft, a fabric tube supported by metal wire stents that strengthen the aorta's weak spot, is placed into the aneurysm during Endovascular surgery, which is shown in Figure 2.7. Endovascular repair of aneurysms provides a significantly faster recovery period than the traditional open surgical procedure and does not need a major incision. Not all aneurysms, however, can be repaired endovascularly [16, 17].

Endovascular surgery is becoming more and more popular since it is thought to have significant short-term benefits in terms of morbidity and mortality. Because it is challenging to monitor patients for an extended period following surgery, there are still few results about the long-term effects of the two approaches. The patient profiles for whom the two approaches are typically used have different risk groups, making it even harder to discern between the two.

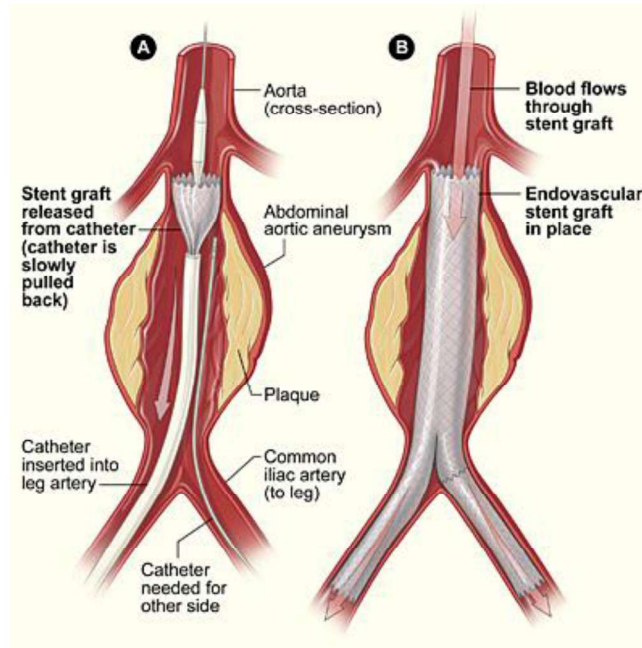


Figure 2.7. Endovascular surgery A: An artery in the groin is used to place a catheter (upper thigh). The stent graft is released from the catheter after it has been threaded to the abdominal aorta. B: Blood can pass through the aneurysm through the stent graft.

2.2 Experimental setup

2.2.1 *in-Vitro* Phantom

An *in-vitro* study of AAA can be divided into one rigid model and one compliant model. The material, thickness of the wall, and method used for the production of the model specify this quality of the model.

The materials used for manufacturing these models can generally be divided into glass and silicon elastomers. Glass results in a rigid model with resistance to the pressure fluctuation caused by physiological flow. However, using silicone elastomers can result in both rigid and compliant models. Compliant models deform under pressure variation.

The silicone elastomers are mostly used for prototyping compliance phantoms. The biggest advantage of these models is the fact that they are more realistic and can be used to prototype patient-specific models [18].

Polydimethylsiloxane (PDMS), a silicone-based elastomeric polymer, is typically cured by heating a mixture of a PDMS base and a crosslinking agent. Depending on the mixing ratio and heating conditions, the material properties of PDMS vary [19]. RTV 3040, RTV 615, and Sylgard 184 are some examples of PDMS.

The main benefits of using PDMS to prototype AAA models include being inexpensive, optically transparent across the visible spectrum down to 240 nm, having a low shrinkage rate, and being simple to fabricate quickly. Due to its excellent elastic characteristics, Sylgard 184 has also been employed for compliant phantom construction. However, temperature and the cross-linking agent significantly impact its mechanical properties [18].

To produce a rigid model using silicone elastomers, it is suggested in many studies to use lost-core casting techniques. In this technique, a male core is molded or die cast in the shape of the cavity (aneurysm) specified for the molded component. Next, the male mold is placed in a casting box, as shown in Figure 2.8. Finally, the silicone elastomer is poured into the casting box and shapes the cavity [20].

It's also important to produce the casting box's surface smooth enough to decrease the optical distortion. The orientation of the surfaces is also important to first, match our region of interest and second, decrease the amount of material we need due to their high prices [18].



Figure 2.8. Lost-core casting- the casting box's surfaces are arranged in a way to increase optical access to vital areas [20]

It is difficult to accurately reproduce the compliance of the artery wall while capturing fluid-structure interaction. Failure to replicate arterial compliance diminishes the model's accuracy [21], which in turn limits the usefulness of the findings for clinical application and therapeutic optimization. To produce a compliant model using silicone elastomers, several methods can be applied. One is to use male and female molds to shape the wall thickness precisely, especially for patient-specific models. In this method, The female mold must surround the male mold precisely. The cavity is filled with silicone, which is then cured. The molds for the male and female are then taken out. The stiff phantom removal procedures can also be utilized to remove the male mold. Female molds are typically simply unbolted and don't need to be removed destructively [18].

In summary, the compiling precision of the manufactured models is affected by; material, curing temperature and time, mixing ratios of curing agent and PDMS silicone, and wall thickness. Several studies have been conducted to investigate the effect of these parameters on compliance.

2.2.2 Blood Mimicking Fluid

Blood is a complex non-Newtonian fluid. Due to the shear thinning property, blood's viscosity changes under different shear rates. Simulating its properties carries great importance for experimental studies. To obtain close to real flow structures it is also vital to match the density and dynamic viscosity of the blood for our blood mimicking fluid (BMF).

The other vital parameter for optical measurement methods that should be considered is the phantom's Refractive Index (RI). Mismatching RI between the solution and model results in distortion in near-wall regions. Since these measurements are based on optical tracking of the particles floating inside the solution, this distortion will affect the results.

Figure 2.9. exhibits a model filled with three different solutions. The solution's refractive index in part B is only 0.003 away from the model's material.

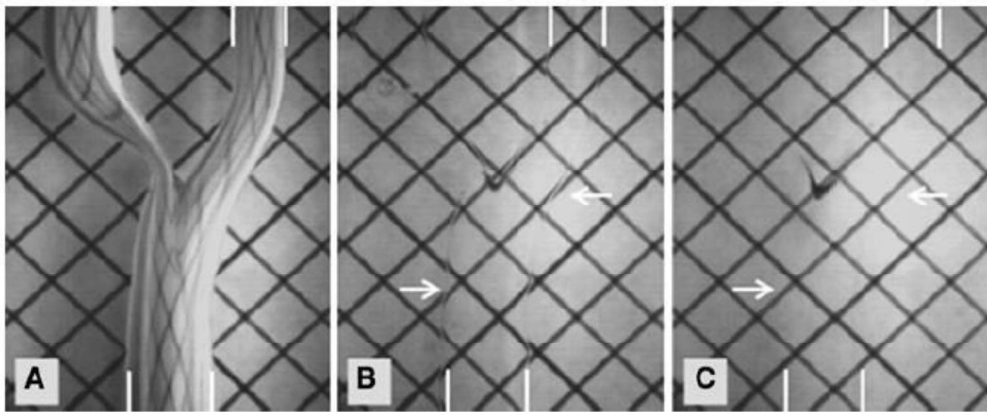


Figure 2.9. matching refractive index's impact on optical access, A)no match, B)close match, C)perfect match [22]

The reported RI of the material used in AAA phantoms in literature is mainly for the wavelength of 589 nm. Several types of research have been conducted to investigate the RI of these materials more specifically. Glass has a general RI of 1.47, but the RI

of silicone elastomers varies between 1.40-1.44 based on their material, mixing ratio, and production method [23].

Yousif et al. (2009) measured the RI of PDMS Sylgard184, 1.414 at room temperature (22.2 ± 0.0 °C) [22].

Prajzler et al. (2017) reported that the RI of PDMS Sylgard 184 modifying the deposition circumstances (hardening temperature and/or A: B mixed agent ratios) could vary refractive indices. He also reported these RI's in five different wavelengths [23]. Figure 2.10. compares the RI of Sylgard 184 samples at different deposition conditions.

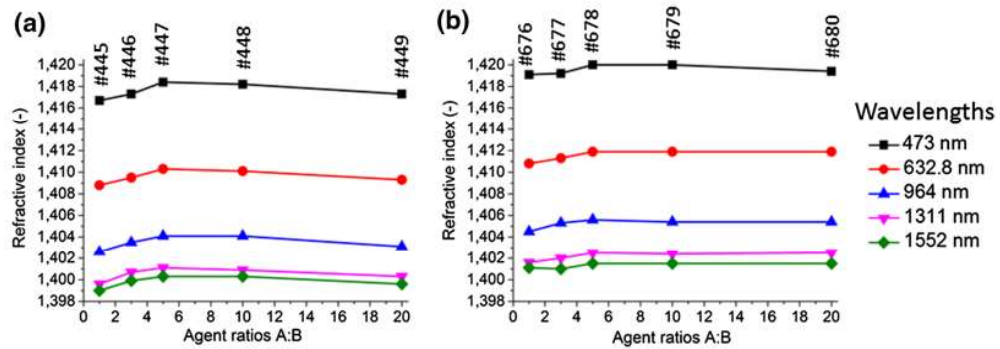


Figure 2.10. The PDMS polymer (Sylgard 184) refractive indices of the samples with varied A: B mixed agent ratios: a) curing conditions at 65°C for two h, b) at room temperature for seven days [23]

As mentioned before, due to shear stresses above 300 s^{-1} blood acts almost like a Newtonian fluid. However, some results challenge this assumption and report a significant difference in flow structure in abdominal aortic aneurysms.

Blood viscosity changes according to gender, age, health, and shear rate. Mayer et al. examined the viscosity of human blood in a variety of patients, both healthy and suffering from chronic coronary heart disease. According to the findings, viscosity ranges from 2.96 mPas in healthy children to 3.72 mPas in healthy men aged 21 to 26. However, the measured viscosity in people with chronic coronary heart disease was 3.98 and 3.60 mPa s, respectively [24].

Rosenson et al. tested the blood viscosity of 126 healthy adult males and females. Viscosity was shown to be 3.26, 4.37, and 5.46 mPa s, respectively, for shear rates of 100, 50, and 1 s^{-1} [25].

It is difficult to choose the working fluid for these studies that has blood density, viscosity, and PDMS index of refraction (RI). A water-glycerol solution has been widely used to match the RI of PDMS Sylgard 184 in literature. But, this solution does not match the blood's dynamic viscosity. Yousif et al.(2009) reported a replacement for this solution with an additive of NaI (sodium iodide), which has a better match of blood properties. Table 2.1 exhibits the properties of the water, glycerol, and the respective BMFs [22]. Furthermore, by changing the additive percentage of NaI, the solution's refractive index can be matched with the phantom without a significant change in density and dynamic viscosity.

A study on the RI of NaI solution for index matching in PIV was done by Bai and Katz et al.(2014). According to their reports, the NaI solution may span the RI range of 1.333–1.51 [26].

Table 2.1 Properties of water-glycerol-NaI and BMF [22]

Fluid	Ratio (Weight percent)	RI	$\rho(\text{kg}/\text{m}^3)$	Dynamic viscosity (mPa)
Blood	-	-	1060@ 37°C	2.9-4.37
Water @ 20°C	-	1.333	998.2	1.0016
Glycerol @ 20°C	-	1.474	1261.08	1.76
Water- Glycerol- NaI	47.38- 36.94- 15.68	1.414	1244	4.31
Water Glycerol	61-39	1.417	1156.6	10.6

However, the most challenging part of using NaI in BMF is the corrosive quality of it that over time, can cause parts of the flow system to degenerate [18].

NaI is pricey, has safety and material concerns, and has been observed to alter the behavior of non-Newtonian fluids [27]. Brindise et al.(2018) suggested an alternative mixture of Water-Glycerol-Urea to overcome this quality of the Water- Glycerol-Na solution. Urea is around 5–15 times cheaper than NaI, safe and straightforward to use, optically transparent, and doesn't discolor. Table 2.2 compares the properties of Water-Glycerol-Urea and Water-Glycerol-NaI solutions with blood and PDMS Sylgard 184.

Table 2.2 Features of the Newtonian solutions of Water-Glycerol with an additive of Urea and NaI with three different viscosity ranges [27]

Starting Viscosity	Material	Wt% water	Wt% Glycerol	Wt% additive	Refractive Index	Viscosity (Pa-s × 10 ⁻³)	Density (kg/m ³)
	Blood; PDMS	-	-	-	1.4118	2.81-5	1060
Low	Urea	45.64	28.77	25.58	1.4118	3.564	1130
	NaI	45.51	28.70	25.79	1.4138	3.117	1229
Medium	Urea	44.07	34.52	21.41	1.4124	4.184	1114
	NaI	44.07	34.52	21.41	1.4143	3.898	1221
High	Urea	43.21	39.96	16.83	1.4143	5.178	1141
	NaI	43.21	39.96	16.82	1.4131	4.616	1211

For some cases (like small vessels with a diameter less than 0.6 mm [28]), the non-Newtonian behavior should be considered too. Adding Xanthan gum (XG) to BMF has been utilized to simulate this property. But it has been reported that XG addition to salt-based fluids like Water-Glycerol NaI decreases the shear thinning property.

Brindise et al. (2018) also examined the effect of 0.02, 0.04, and 0.06 weight percent additive to the Water-Glycerol-Urea solution. Figure 2.11 compares the properties of these mixtures in detail [27].

For evaluating the non-Newtonian property, oscillatory viscosity and elasticity parameters can be considered. The complex viscosity can be formulated as equation 2.2, where η' is the oscillatory viscosity, and η'' is the oscillatory elasticity

$$\eta = \eta' - i\eta'' \quad (2.2)$$

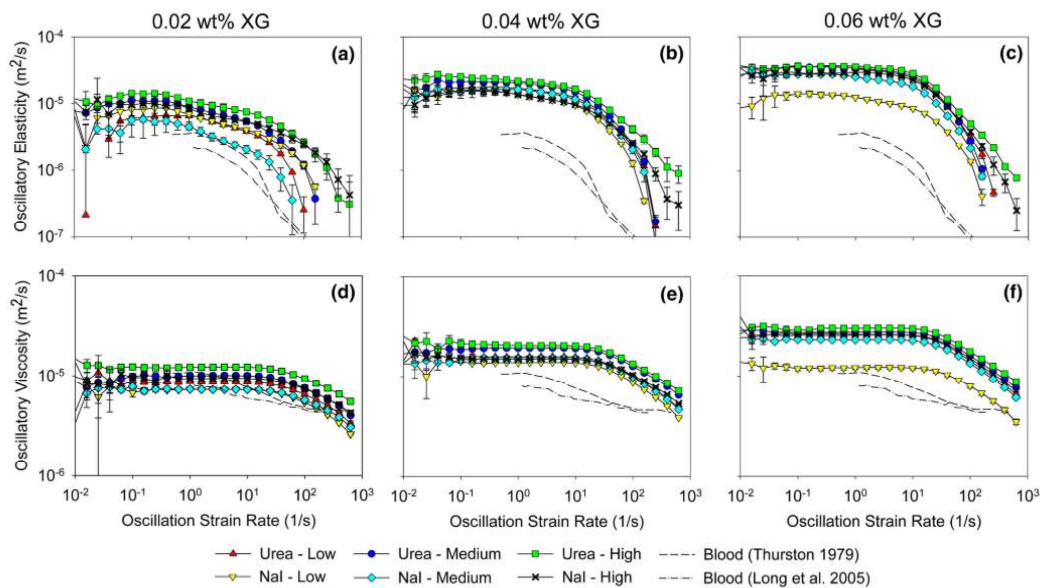


Figure 2.11. Oscillatory elasticity (a–c) and Oscillatory viscosity (d–f) were measured in the low, medium, and high water–glycerol ratios with the addition of urea and NaI. The xanthan gum concentrations were 0.02 (a–d), 0.04 (b–e), and 0.06 (c–f) [27]

As it can be observed in Figure 2.11, a 2% additive of XG results in the best non-Newtonian behavior match with blood [27].

2.3 Determining Factors for Flow Structure

2.3.1 Reynolds Number

The Reynolds number is the ratio of inertial forces to viscous forces. The Reynolds number is a dimensionless number used to categorize the fluids systems in which the effect of viscosity is important in controlling the velocities or the flow pattern of fluid [29].

Reynolds number can be formulated as equation 2.3 for aneurysm phantoms.

$$Re = \frac{\rho u_m D}{\mu} \quad (2.3)$$

Where:

u_m : average velocity at aneurysm inlet (m/s)

D : diameter of the model at the inlet (m)

μ : the dynamic viscosity (Pa.s)

ρ : density (kg/m³)

2.3.2 Womersley Number

The ratio of oscillatory inertia to viscous effects for fluid in pulsatile flow is known as the Womersley Number, and it is crucial for studying and quantifying pulsatile flow [30].

Womersley number can be formulated as equation 2.3 for aneurysm phantoms.

$$\alpha = \frac{D}{2} \sqrt{\frac{\rho\omega}{\mu}}$$

Where:

ω : angular frequency (rad/s)

D : diameter of the model at the inlet (m)

μ : the dynamic viscosity (Pa.s)

ρ : density (kg/m³)

The Womersley number affects how the velocity profile looks, and for high values, an oscillating plug flow is frequently seen, making it clear that inertia is the dominant force in the flow. According to the ratio of oscillatory inertia, viscous forces and the driving pressure gradient are in equilibrium for small Womersley values[30].

Figure 2.12 exhibits the effect of the Womersley number on the velocity profile for pulsatile flows in a straight tube. It is also reported that the Womersley number varied between 12-16 for the aorta in the human body [31].

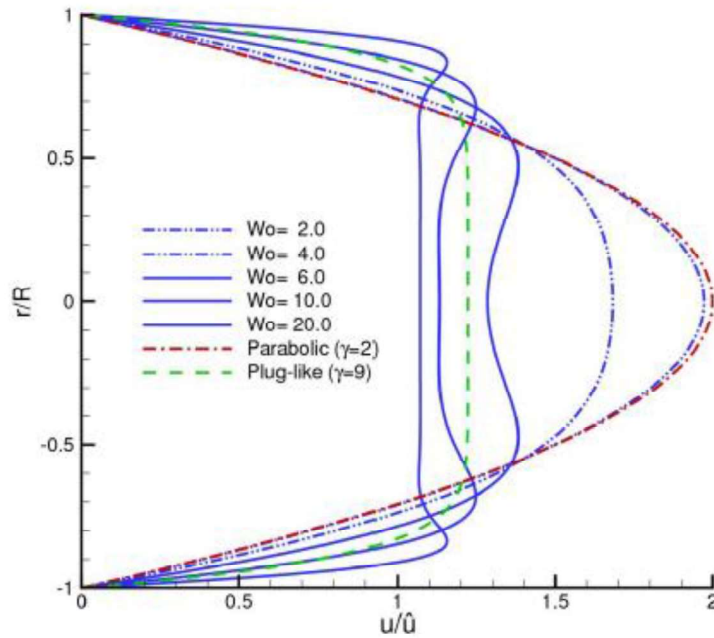


Figure 2.12. Velocity profiles of steady parabolic and plug-like flows and peak velocity profiles of five different Womersley flows [32]

2.4 Vortex Characterization of Flow

A vortex is frequently thought of as a fluid motion that rotates around a shared centerline. It is determined by the fluid's vorticity, which quantifies the speed of regional fluid rotation. The fluid typically moves around the vortex, speeding up as it gets closer and releasing pressure as it does so. Vortices appear in a wide range of sizes for both natural and technological uses [33].

Vortices play a vital role in the location of the thrombus and aneurysm expansion. Various methods have been utilized to identify vortex locations. These methods can be categorized in two ways; First, Eulerian or Lagrangian, and second, Local or non-local.

In the Eulerian method, an observer tracking a fluid particle as it moves across space and time investigates the flow field. In contrast, the observer examines particular areas and the fluid particles moving across them, such as pathlines.

In local methods, every point of the flow field is studied for vortical flow characterization. On the other hand, in non-local approaches, the whole field flow investigation is done.

Jeong & Hussain et al.(1995) Proposed two requirements for vortex identification methods: [34]

- (i) Net vorticity is necessary for a vortex core (hence, net circulation). As a result, vortex cores are not affected by potential flow areas, which are defined as vortices with zero cross-section.
- (ii) The detected vortex core's geometry must be Galilean invariant.

Inertial frames are all reference frames that are moving with a constant speed about an inertial reference. Because no particular inertial frame is preferred over another, Newton's Laws of Nature hold in all inertial frames of reference, making it impossible to determine absolute velocity. Galilean invariance describes this [35].

In this section, some of the vortex identification methods are presented.

2.4.1 Streamlines

A closed or spiral streamline could be an observant of a vortex. But this method is not completely reliable since it does not satisfy requirement (ii). The other challenging fact is that the particle may not fully circulate in the vortex core. This problem is illustrated in Figure 2.13.

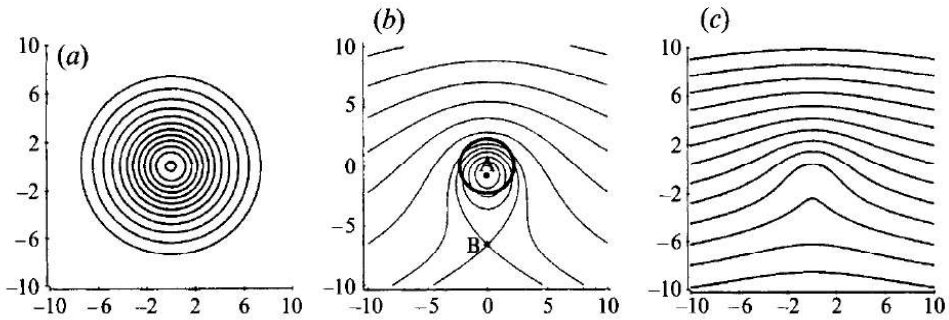


Figure 2.13. Streamline of a vortex in three different reference frames: a) vortex core, b) inside the core, c) out of the core [34]

2.4.2 Vorticity Magnitude

Vorticity refers to the twice the rotation of the fluid at a certain point which is also defined as the curl of the velocity. The traditional method of identifying vortical formations involves choosing a threshold for the magnitude of the vorticity and designating as a vortex any area where the magnitude of the vorticity exceeds the threshold. Vorticity vectors can be formulated as equation 2.4 [36].

$$\boldsymbol{\omega} = \nabla \times \mathbf{V} = \left(\frac{\partial}{\partial x} \quad \frac{\partial}{\partial y} \quad \frac{\partial}{\partial z} \right) \times (u \ v \ w) \quad (2.4)$$

Where:

$\boldsymbol{\omega}$: the vorticity vector

x, y, and z: coordinates

u, v, and w: velocity component

For a two-dimensional velocity field, the vorticity vector, in the absence of the z-component of velocity, is parallel to the z-axis, which can be expressed as equation 2.5

$$\omega_z = \left(\frac{\partial v}{\partial x} - \frac{\partial u}{\partial y} \right) \quad (2.5)$$

However, this method also carries some obstacles. The major problem is the fact that vorticity magnitude can not distinguish the vortex cores in a shear flow since, due to the presence of large gradients, shear layers have high vorticity magnitude [34].

2.4.3 Swirling Strength Criterion

Swirling strength (λ_{ci}) is a method based on velocity gradient tensor (VGT). Equation 2.6 expresses the relevant matrix for a 3D velocity field.

$$VGT = \nabla \mathbf{V} = \begin{bmatrix} \frac{\partial u}{\partial x} & \frac{\partial u}{\partial y} & \frac{\partial u}{\partial z} \\ \frac{\partial v}{\partial x} & \frac{\partial v}{\partial y} & \frac{\partial v}{\partial z} \\ \frac{\partial w}{\partial x} & \frac{\partial w}{\partial y} & \frac{\partial w}{\partial z} \end{bmatrix} \quad (2.6)$$

This matrix has a characteristic equation (2.7) with three invariants of P, Q, and R.

$$\lambda^3 + P\lambda^2 + Q\lambda + R = 0 \quad (2.7)$$

To see vortices, the swirling strength technique makes use of the imaginary portion of the complex eigenvalue of the velocity gradient tensor. This hypothesis is supported by the decomposition of the velocity gradient tensor in Cartesian coordinates as equation 2.8 [36].

$$VGT = [v_r \quad v_{cr} \quad v_{ci}] \begin{bmatrix} \lambda_r & 0 & 0 \\ 0 & \lambda_{cr} & \lambda_{ci} \\ 0 & -\lambda_{ci} & \lambda_{cr} \end{bmatrix} [v_r \quad v_{cr} \quad v_{ci}]^{-1} \quad (2.8)$$

Where:

$\lambda_{cr} \pm i\lambda_{ci}$: the complex eigenvalue

$v_{cr} \pm iv_{ci}$: the corresponding eigenvectors

λ_r : the real eigenvalue

v_r : the corresponding eigenvector

In a coordinate system of (y_1, y_2, y_3) , specified by $\{v_r, v_{cr}, v_{ci}\}$, the streamlines can be expressed by equation 2.9 [37].

$$y_1(t) = C_r \exp \lambda_r t, \quad (2.9a)$$

$$y_2(t) = \exp \lambda_{cr} t [C_c^{(1)} \cos(\lambda_{ci} t) + C_c^{(2)} \sin(\lambda_{ci} t)], \quad (2.9b)$$

$$y_3(t) = \exp \lambda_{cr} t [C_c^{(2)} \cos(\lambda_{ci} t) - C_c^{(1)} \sin(\lambda_{ci} t)], \quad (2.9c)$$

Where $C_r, C_c^{(1)}$ and $C_c^{(2)}$ are constants. As Figure 2.14 illustrates, Along the axis v_r , the local flow is either compressed or stretched. On the other hand, flow shows a swirling motion on the plane created by the other two vectors.

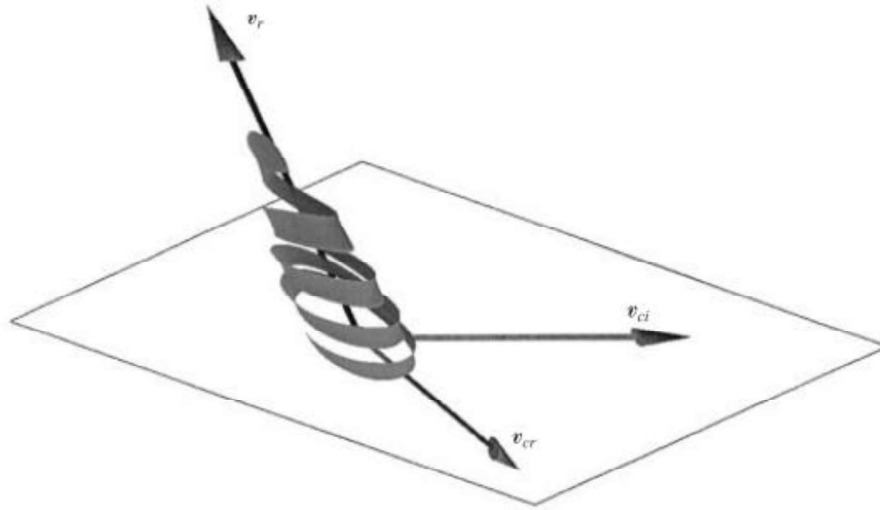


Figure 2.14. Swirling motion of the fluid [37]

The local swirling strength (λ_{ci}) of the vortex, or λ_{ci} , is a measure of the intensity of this swirling motion. There is no clear definition of the λ_{ci} threshold. Theoretically, it ought to be set to zero. However, positive values produce outcomes that are more evenly distributed [36].

For 2D velocity fields eliminated the third component of the velocity resulting in a velocity gradient tensor of 2.10,

$$\text{VGT} = \begin{bmatrix} v_{cr} & v_{ci} \end{bmatrix} \begin{bmatrix} \lambda_{cr} & \lambda_{ci} \\ -\lambda_{ci} & \lambda_{cr} \end{bmatrix} \begin{bmatrix} v_{cr} & v_{ci} \end{bmatrix}^{-1} \quad (2.10)$$

Therefore, the first equation of the streamlines, $y_1(t)$ also vanishes.

2.5 Previous Investigations

To understand the reason behind AAA creation, early experimental studies have focused on the flow structure in the normal aorta (without expansion). Ku et al.

(1989) used a realistic abdomen glass model (Figure 2.15) and reported a complex flow at the infrarenal aorta where AAA generates [38].

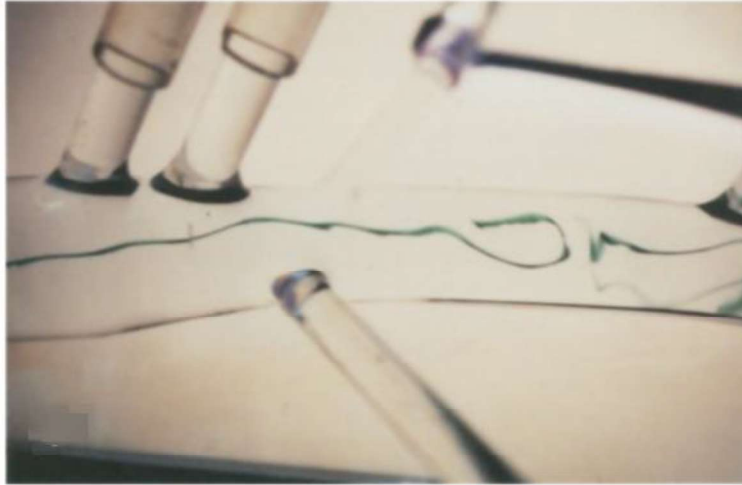


Figure 2.15. Complex flows at the anterior half of the infrarenal aorta [38]

Some studies have investigated the flow structure inside an axisymmetric AAA model under both steady and pulsatile flow. Yu. (2000) studied the flow in two rigid glass phantoms under different steady and pulsatile (sinusoidal) flow with different Reynolds and Womersley numbers. He reported a recirculating vortex covering the majority of the bulge area in steady flows. He also stated that the vortex's strength was increased by increasing the Reynolds number to a point. The vortex starts at the distal end of the bulge portion as shown in Figure 2.16.

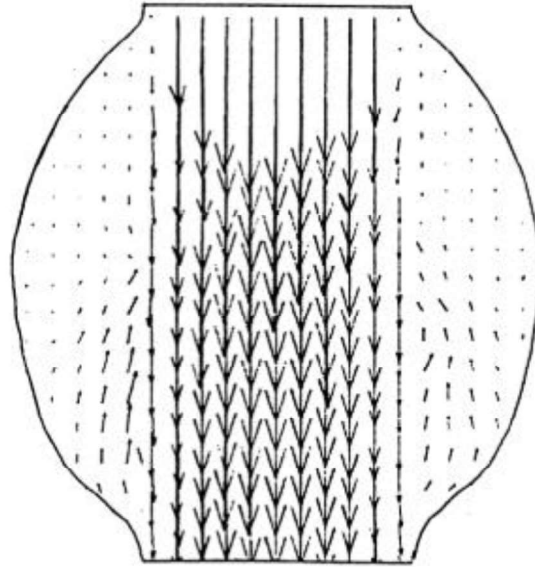


Figure 2.16. Velocity vectors in the bulge portion under a steady flow of $Re=1000$
[39]

He also reported the effect of the variation in Womersley number and the dimension of the model on the flow structure. The other discussion in this study was about the effect of steady and pulsatile flow. The vortex core location and intensity do not differ in steady flow, but on the other hand, it changes during pulsatile flow, so this observation made it quite evident that extrapolating the steady flow results to the examination of the pulsatile counterpart was not appropriate [39].

One of the primary experimental studies under physiological flow was done by Fukushima et al. (1989). They investigated flow inside four different rigid glass models, as shown in Figure 2.17.

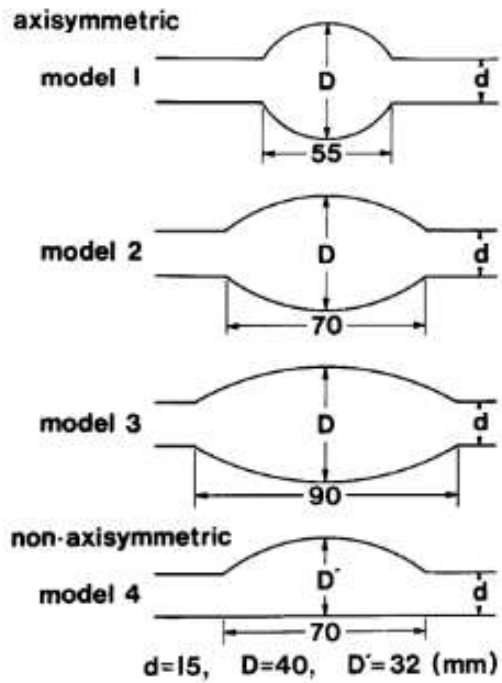


Figure 2.17. Dimensions of the glass AAA models [40]

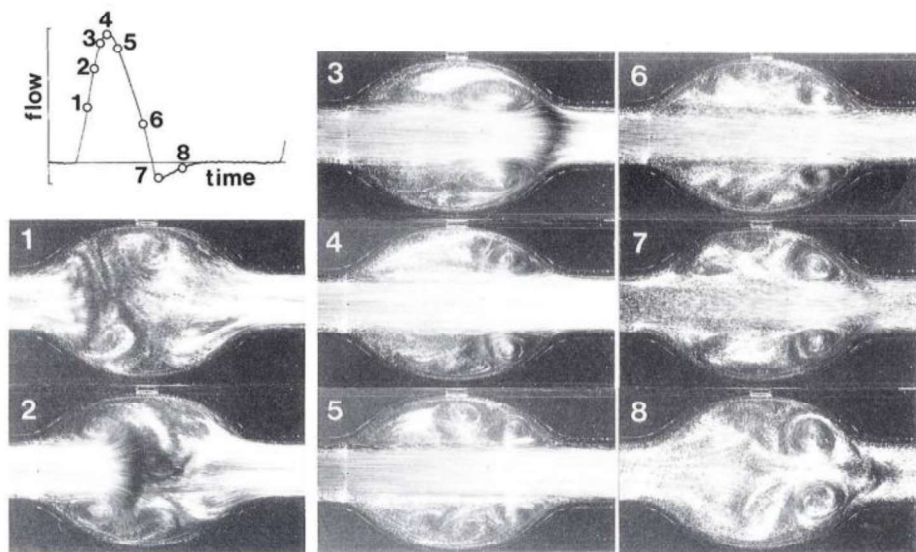


Figure 2.18. Flow progress during a cycle of physiological flow with $Re_{\text{mean}}=289$ and $\alpha=4.07$ in the model [40]

As illustrated in Figure 2.18, the flow separation happens at the acceleration part of the flow pattern. During the acceleration, also the vortex moves away from the left side of the aneurysm. The vortex strength increases in this part, which results in another vortex with opposite rotation. This vortex increases in size and hence decreases in strength at the start of the deceleration and finally disappears, but the primary vortex stands still during the deceleration, even when the velocity approaches zero. At the moment where velocity is reversed (part7 in Figure 2.18), the primary vortex is strengthened [40].

Stamatopoulos et al. (2010) studied the hemodynamics inside an axisymmetric rigid model (Figure 2.19) produced by PDMS Sylgard 184 under different steady and sinusoidal pulsatile flows. The BMF was a mixture of water and glycerol.

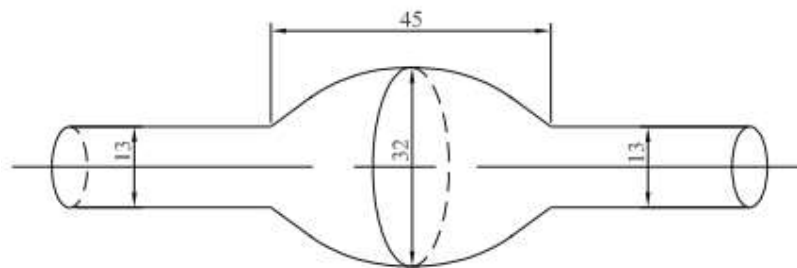


Figure 2.19. AAA axisymmetric sylgard 184 model. Dimensions in mm [41]

In this study, it has been reported that the distance between reattachment location and exit of the AAA becomes smaller when Re increases which is visible in Figure 2.20. High wall pressure gradient and high wall shear stresses occur at this location [41].

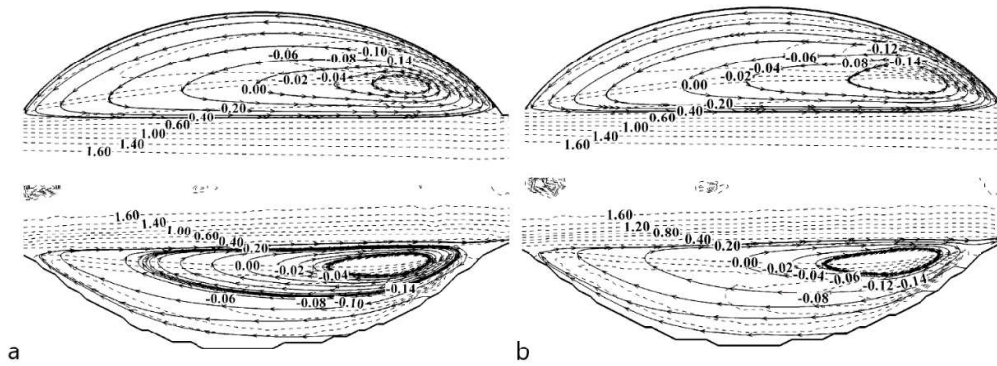


Figure 2.20. Axial velocity contours and streamline at steady flow a) $Re=584$
b) $Re=690$ [41]

Recent studies have focused on the effect of the material and the compliant property of the models on the flow structure. Deplano et al. (2007) compared the hemodynamics inside a rigid glass and a flexible model made of polyurethane. Both models had the same dimension shown in Figure 2.21.

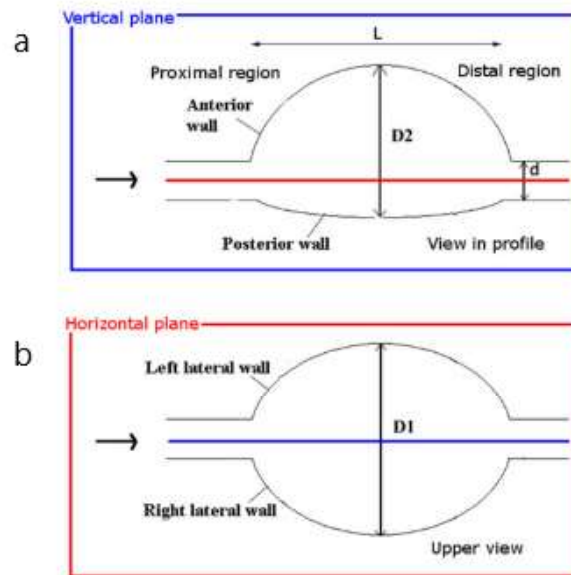


Figure 2.21. Plane definitions in the symmetric AAA model a) Vertical plane
b) Horizontal plane [42]

In the compliant model under physiological flow, a deformation of 1.5% at diameter D_2 has been reported. Generally, A shear layer is created by the jet's boundary velocity discontinuity, eventually rolling into a vortex ring in both models. In the horizontal plane, the presence of the primary vortex is visible in both models. However, in the vertical plane, as illustrated in Figure 2.22, there is only one vortex close to the anterior part in the rigid model. On the other hand, there is a second vortex happening in the posterior part of the compliant model.

This behavior difference is because the flexible walls collect the energy in the acceleration part of the physiological flow, which eases the creation of vortices. On the other hand, during the deceleration part, this energy makes the wall withdraw [42].

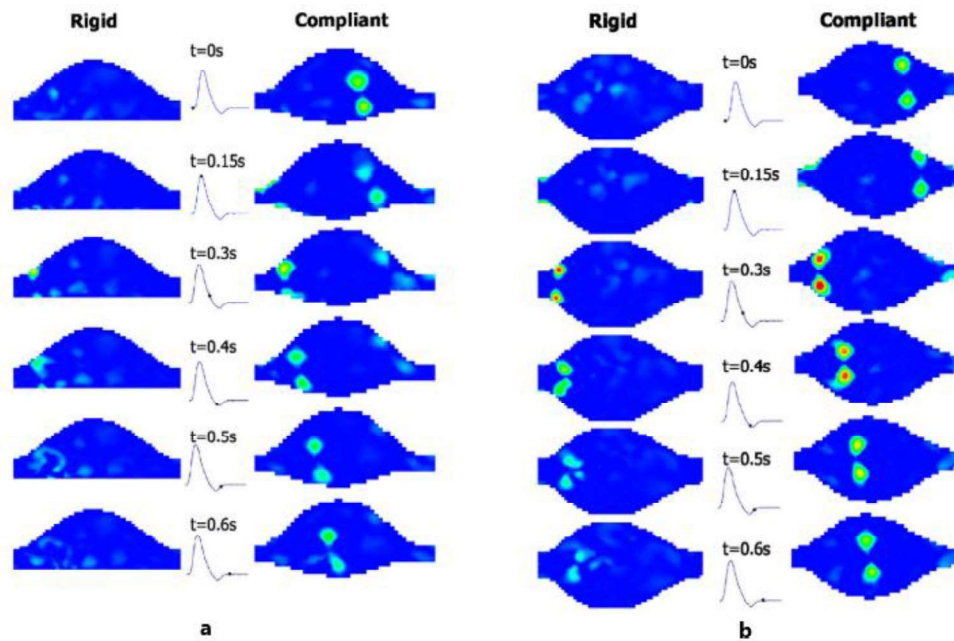


Figure 2.22. Comparison of the swirling strength (λ_{ci}) in rigid and compliant models in a) vertical plane, b) horizontal plane [42]

CHAPTER 3

EXPERIMENTAL SETUP AND MEASUREMENT TECHNIQUES

In detail, this chapter describes the experimental setup at the Fluid Mechanics Laboratory in the Mechanical Engineering Department, Middle East Technical University.

3.1 Flow Circulatory Setup

The flow circulatory setup is a closed system, where the blood mimicking fluid (BMF) runs through it. This solution is stored in a plexiglass tank. A positive displacement gear pump (Dayton 4KHH8, Grainger, Inc., Lake Forest, IL) drives the BMF through the piping. The pump's shaft is attached by coupling to an electromotor controlled by computer software. This electromotor can provide the intended flow pattern, like physiological flow. A sensitive adjustable valve is placed in the setup to control the pressure in the aneurysm. Two pressure transducers are installed upstream and downstream of the model using identical T junctions. The pipe diameter was 8mm before valve 1 and after valve 2, but the diameter between these two was adjusted based on the model's inlet and outlet diameters. Figure 3.1 is the schematic view of the blood circulatory system.

BMF is filtered before entering the reservoir to avoid contamination in the system. To avoid corrosion of the salt-based material in the BMF, the material of the components in the setup is selected to decrease the risk.

The images of this setup are provided in Figure 3.2.

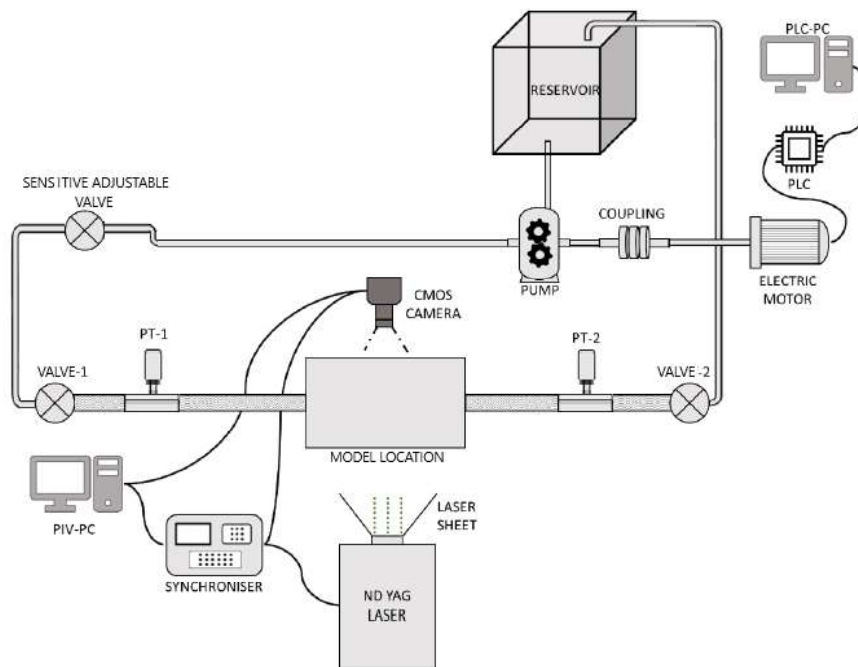


Figure 3.1. Schematic configuration of the setup in this study

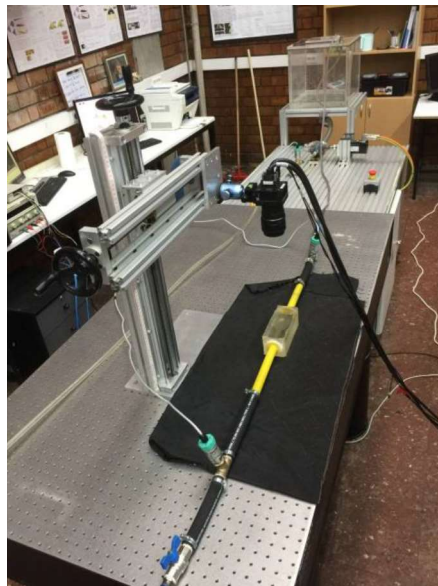


Figure 3.2. Flow circulatory system in Fluid Mechanics Laboratory, METU

3.1.1 AAA models

Hemodynamics inside two different models are investigated in this study, a simple axisymmetric model and a patient-specific one with complicated geometry. These models are produced using PDMS Sylgard184 with a refractive index of 1.4118. Figure 3.3 shows the dimensions of the simple model, and Figure 3.4 exhibits the properties of the patient-specific one. SM refers to the Simple model, and PSM refers to the patient-specific model.

The equipment and BMF were switched in the set-up to match the properties of Sylgard184 instead of glass before the experiments. Using the SM in the first step facilitated the challenges in this process. The other benefit of the SM is that it made it possible to develop the experimental matrices and processing methods according to the previous studies.

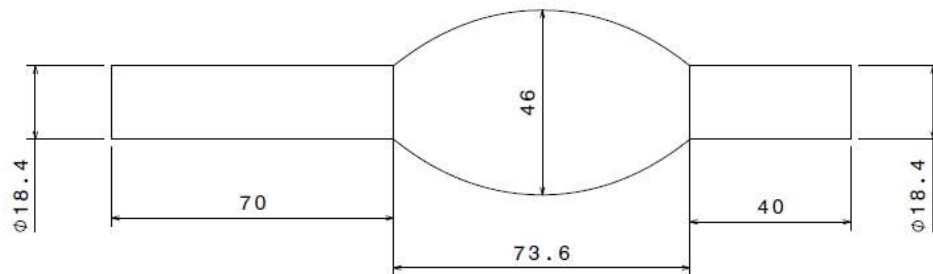


Figure 3.3. Dimension of the simple model (SM) in mm

Both of the models are produced by the lost-core casting technique with a male mold inside a casting box (Figure 2.8). Also, a minimum thickness of 12 mm for the wall of the aneurysm is provided, as Geoghegan et al. (2012) recommended for rigid behavior [43].

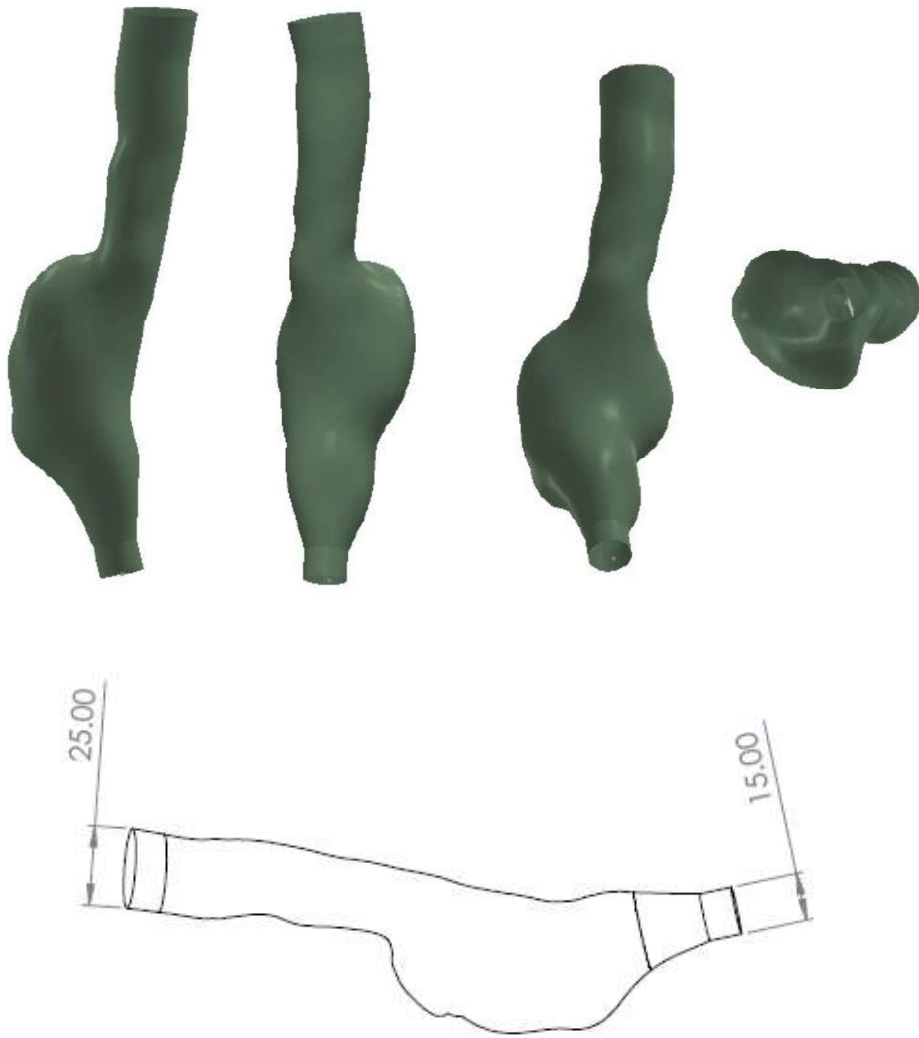


Figure 3.4. The patient-specific model: upper: 3D view, lower: the schematic view, dimensions in mm

3.1.2 Working fluid

The three component Newtonian blood mimicking fluid composed of water, glycerol, and urea is prepared for this study based on properties provided by Brindise et al. (2018) [27]. These properties are tabulated in Table 3.1.

Table 3.1 Properties of the blood mimicking fluid

<i>Material</i>	<i>Wt% water</i>	<i>Wt% Glycerol</i>	<i>Wt% additive</i>	<i>Refractive Index</i>	<i>Viscosity (Pa-s $\times 10^{-3}$)</i>	<i>Density (kg/m³)</i>
Blood; PDMS	-	-	-	1.4118	2.81-5	1060
BMF	45.64	28.77	25.58	1.4118	3.564	1130

To confirm the data, the solution's refractive index was measured at 1.4125 using a refractometer at room temperature. This property resulted in an acceptable refractive index match with the PDMS Sylgard 184, as exhibited in Figure 3.5. However, the solution discolored after almost four weeks. Hence, there was a need for frequent replacement of the fluid.

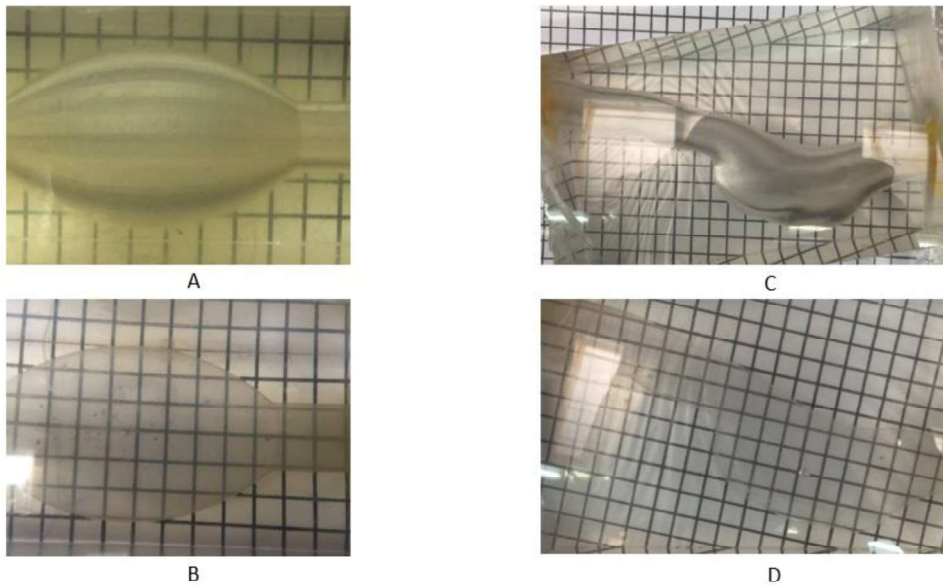


Figure 3.5. The simple model A) Empty B) Filled with blood mimicking fluid, The patient-specific model C) Empty D) Filled with blood mimicking fluid

3.2 Experimental Matrices

3.2.1 Measurement planes

As mentioned before, in 2D PIV, the target volume is studied in the planar approach. For SM, the center plane, shown in Figure 3.6, and for the PSM, three different planes, as shown in Figure 3.7, were considered.

The first plane in PDMS is the midplane of the inlet and outlet. The second plane is 1.2 cm lower than the midplane, and the third is 0.8 cm lower than the second plane.

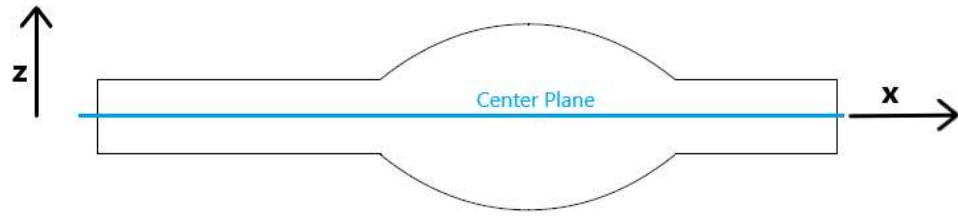


Figure 3.6. Measurement plane at SM

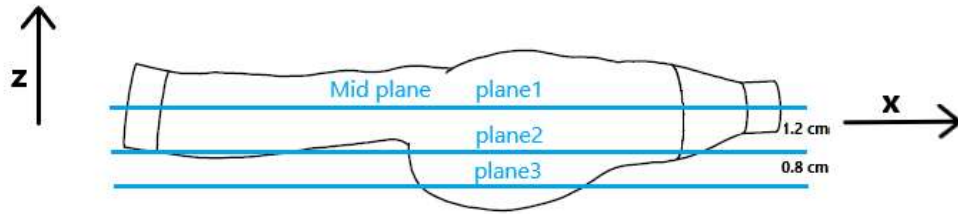


Figure 3.7. Measurement planes at PSM

Since the PSM has a more complicated geometry, the interfering area of the model and laser sheet is more complex than the SM. This interfering area is exhibited in Figure 3.8. The small area at plane #2 is not quantified due to the high optical distortion.

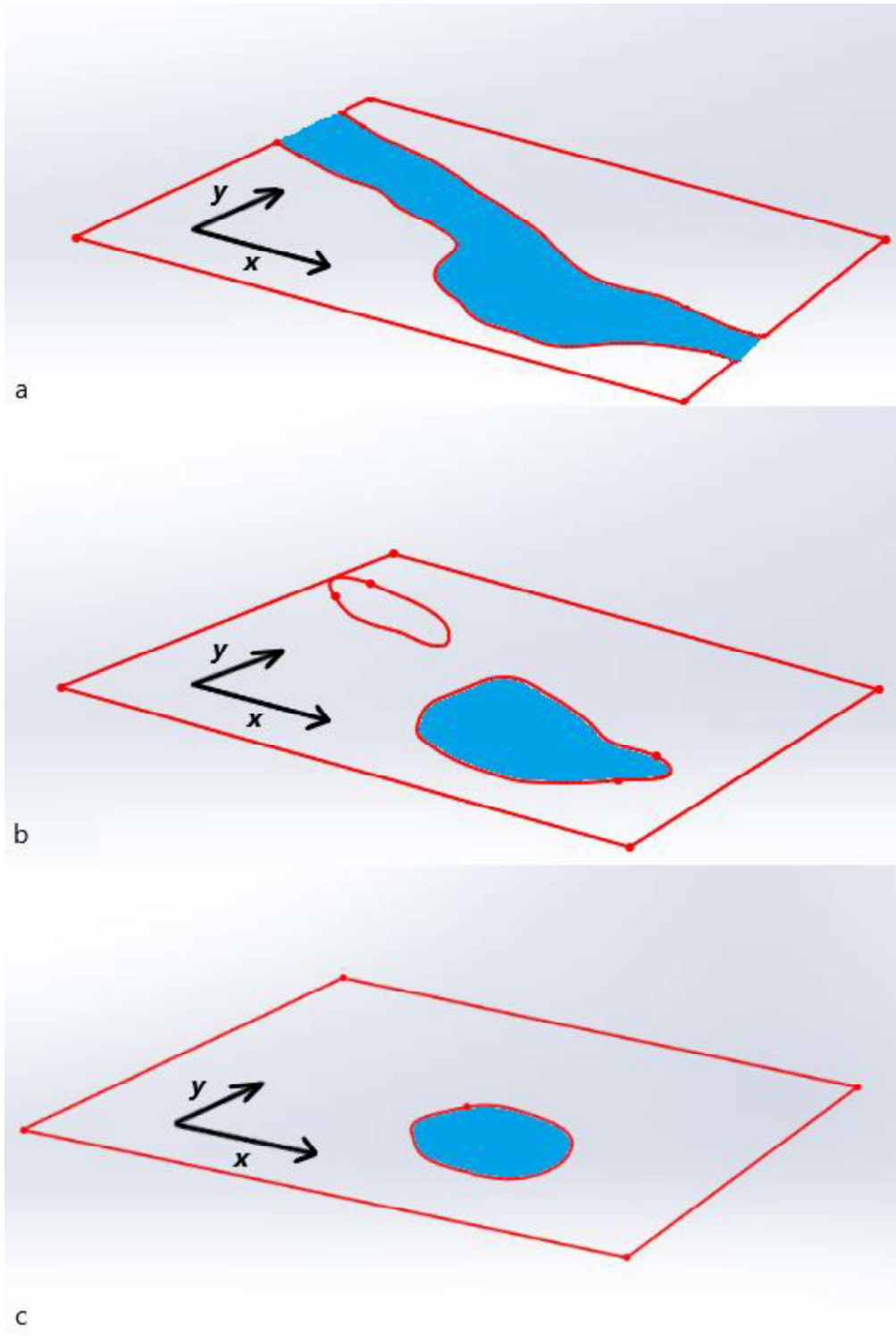


Figure 3.8. The measurement regions at PSM in; a)plane #1, b)plane #2, c)plane #3

3.2.2 Flow Arrangements

Flow structures in SM and PSM are investigated under physiological flows in the planes mentioned above. In this section, the properties of these flow patterns are presented. Both of these flow simulations have a period of 1 second. Table 3.2 provides the properties of these flow simulations. Figure 3.9 and Figure 3.10 exhibit the flow pattern of these cases

Table 3.2 Flow properties

Model	Flow type	Flow rate range (ml/s)	Re_{mean}	α
Simple Model (SM)	Physiological	4-68	345.5	12.98
Patient-Specific model (PSM)	Physiological	2.5-57	258.5	12.98

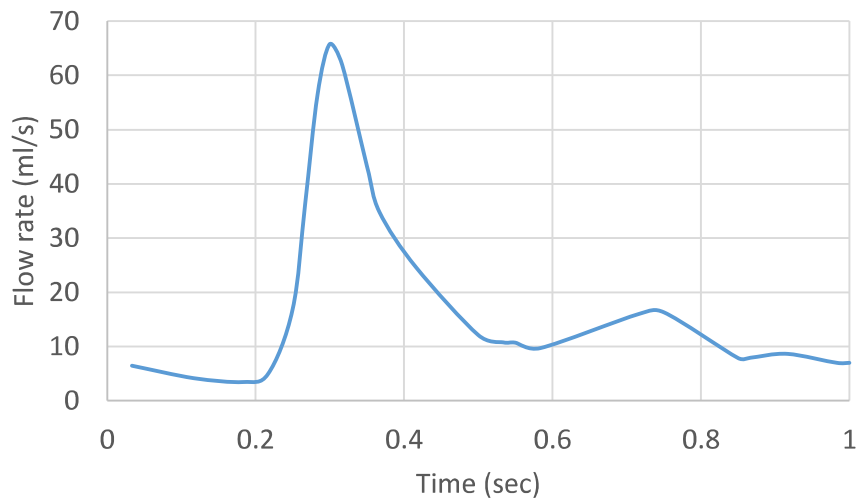


Figure 3.9. Flow rates in the physiological flow of SM

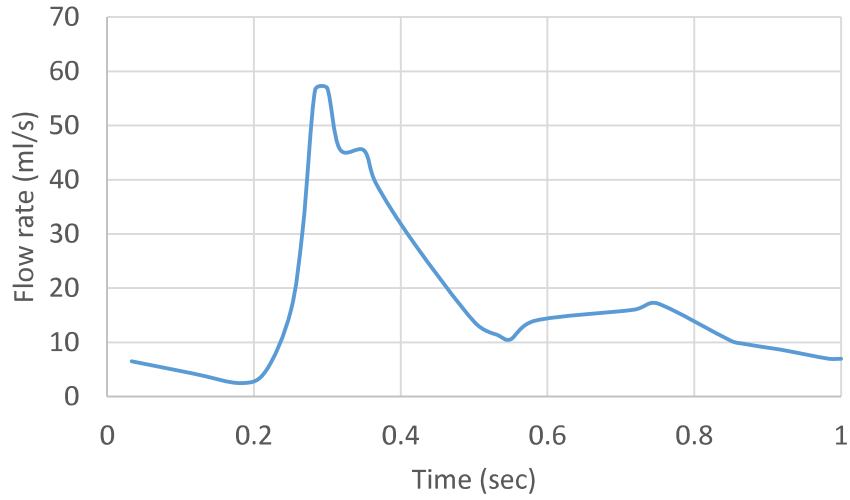


Figure 3.10. Flow rates in the physiological flow of PSM

As mentioned before, both of the models deform under unsteady flows. The maximum diameter deformations in the physiological flows are reported in table 3.3.

Table 3.3 Deformation amount of models under physiological flow conditions

Model	<i>Flow case</i>	<i>Maximum Diameter Deformation (%)</i>
Simple model	Physiological	4.1
Patient-Specific Model	Physiological	3.4

3.3 Pressure Measurements

Two identical GEFTRAN TKGNI1F2UM pressure transducers with a range of 0-2 bar and signal output range of 0-10 volts are installed at the inlet and outlet of the models. Both sensors are installed with identical T junctions to avoid complications.

The National Instrument NI6024E card and SCB-68 terminal block are used to acquire data from these sensors. The sensors have an input range of 10-30 volts and are excited by an external power supply.

PT1 refers to the pressure transducer at the inlet, and PT2 refers to the one at the outlet of the AAA models. Figure 3.11 shows the pressure distributions in SM under the physiological flow. Figure 3.12 exhibits these patterns for PSM.

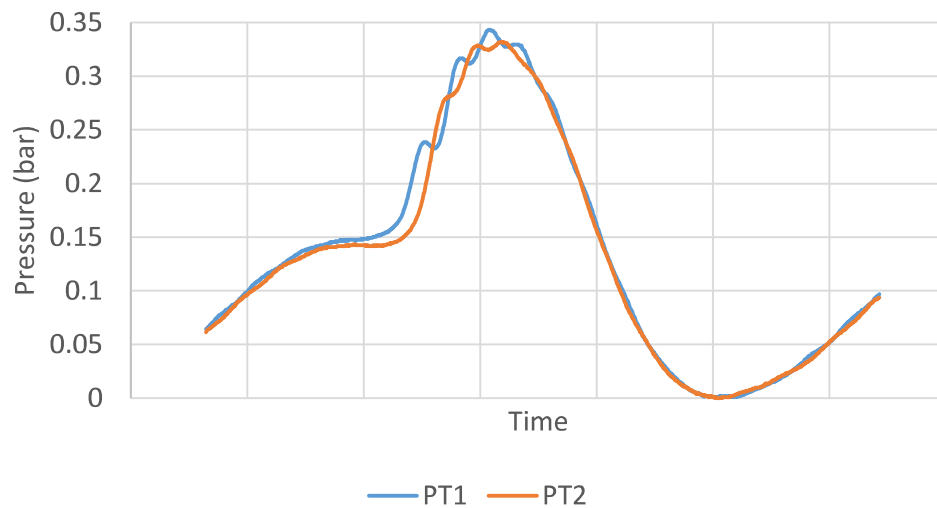


Figure 3.11. Pressure at the inlet (PT1) and outlet (PT2) in one cycle (1sec), SM

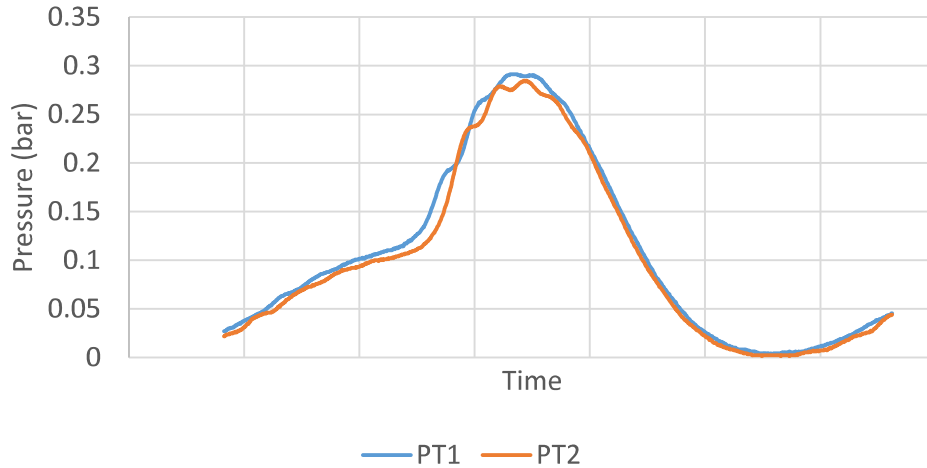


Figure 3.12. Pressure at the inlet (PT1) and outlet (PT2) in one cycle (1sec), PSM

3.4 Velocity Measurement System: Particle Image Velocimetry (PIV)

The flow inside the models is studied using particle image velocimetry. PIV is an optical measurement technique that calculates the instantaneous velocity of the flow in a cross-correlation. 2D PIV measures the velocity field in a plane and characterizes the velocity in a two-dimensional map.

This technique is based on the distance traveled by the particles floating in the fluid. First, these particles should have the same density as the fluid itself to follow the current, and second, they should scatter enough light to be detected by the camera. A pair of images is taken via a high-speed camera from the target plane, illuminated by a laser sheet. A device synchronizes laser shots and the camera's imaging instant.

The recorded image pairs are divided into small sub-regions called interrogation areas. These interrogation areas are cross-correlated in each image of a pair (frame).

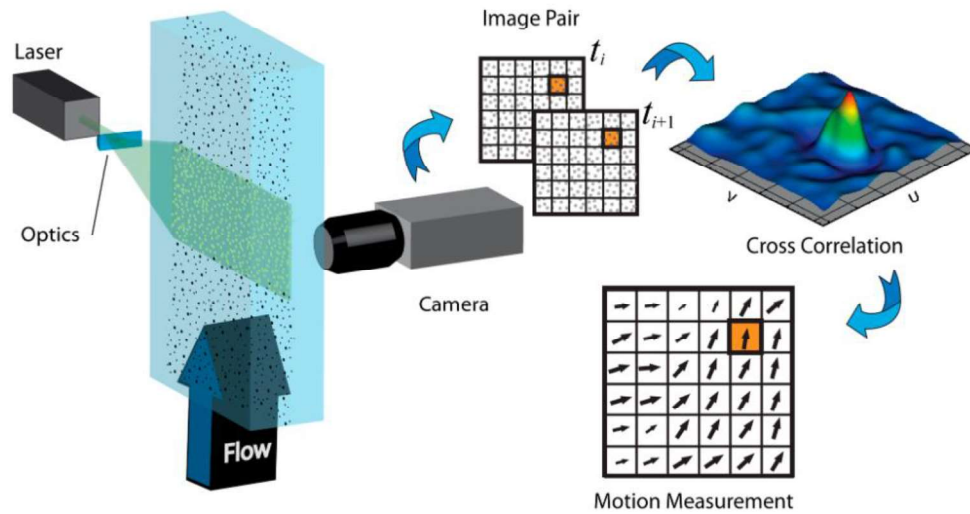


Figure 3.13. Principle of planar PIV (2D PIV)

Once the particles are distinguished in the interrogation area, the cross-correlation measures the velocity vector in that interrogation area. Once the correlation repeats for all sub-regions, a velocity map is produced. Figure 3.13 illustrates the principle of the PIV technique.

In the setup, the TSI PIV hardware is utilized and controlled by the Insight 4G software, which is also a product of the TSI company. The lasers are empowered by 15HZ double pulsed Q-switched Litron Nano L200-15 200mJ Nd: YAG. These laser beams are changed to laser sheets through a spherical lens with a focal point of 1000 mm and a cylindrical lens with a radius of -15 mm. The high-speed camera is a four mega-pixel CMOS camera with a Nikon Nikkor 50 mm lens. The laser and the camera are synchronized via the LaserPulse™ 610036 synchronizer. Silver-coated hollow glasses with a diameter of 10 microns and a density of 1.4 g/cm^3 produced by Dantec Dynamics are used to seed the fluid. Equation 3.1 and 3.2 illustrate the calculation of the Stokes number (Stk), which characterize the behavior of particles suspended in a fluid stream. This index proves that these particles can follow the current accurately.

$$Stk = \frac{\tau \times u_0}{d_p} \quad (3.1)$$

$$\tau = \frac{\rho_p d_p}{18\mu_f} \quad (3.2)$$

Where:

τ : relaxation time of the particle

u_0 : fluid velocity

d_p : particle diameter

ρ_p : particle density

μ_f : dynamic viscosity of the fluid

Considering the qualities of the particle and BMF assuming the maximum velocity of 0.2 m/s in both models, $Stk < 0.05$. Hence, it can be concluded that the employed particles can follow the stream precisely.

3.4.1 Phase Averaging Method

An automatically synchronized phase averaging method is employed in this study. In this method, several images are taken in the same instant of a flow cycle and averaged to acquire time-resolved velocity fields. To capture the images, the pomp software triggers the laser shot at the same phase of the flow pattern. The high-speed camera is synchronized with the laser shot and captures the image pair at that instant. 100-200 image pairs are captured in each phase to increase the precision. Stream properties are investigated in thirteen instants of the physiological pattern in SM. However, only ten of them are presented in this study. Figure 3.14 show these target phases.

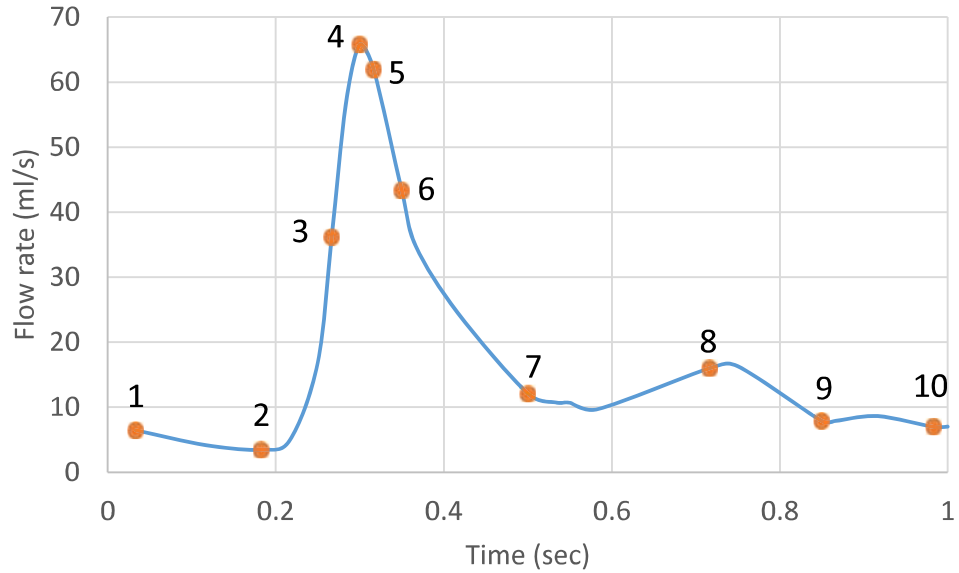


Figure 3.14. Measurement instants of physiological flow in SM

Twelve instants are studied at the physiological flow in PSM. Like the SM case, ten phases, as shown in Figure 3.15, are chosen to be presented in the latter base on their importance. In both cases, four instants at the acceleration and six at the deceleration parts are presented and discussed in the next chapter.

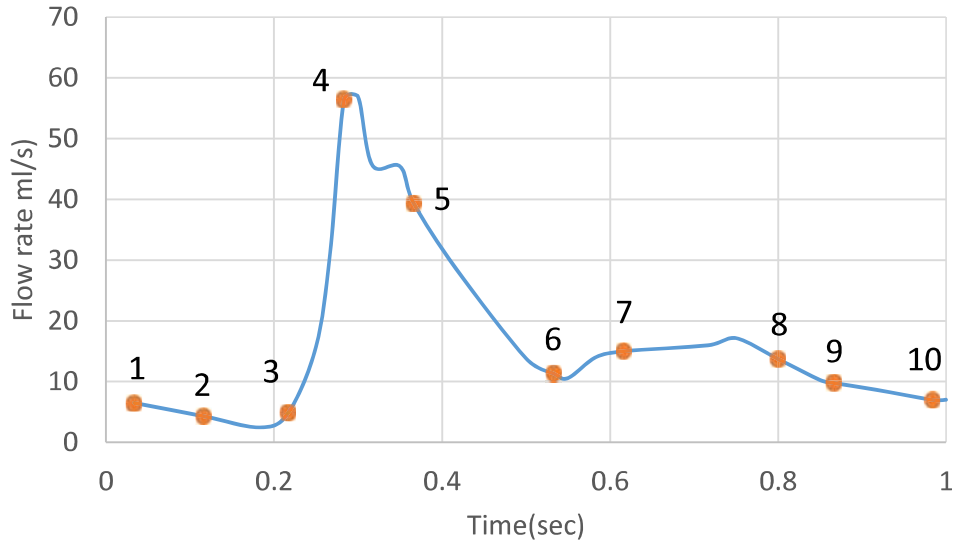


Figure 3.15. Measurement instants of physiological flow in PSM

3.5 Processing and Post-Processing

To calculate the velocity vectors inside the intended area, the Isinght 4G processor is used. The time difference between the two frames of an image pair is adjusted between 800-1700 μ s depending on the velocity magnitude. Once the images are taken (Figure 3.16) in the processing tab, spatial calibration is done with a reference length like the inlet diameter of the model in our case (Figure 3.17).

In the next step, the preprocessor specifies our background subtraction method. In this study, the average intensity technique is employed. Figure 3.18 illustrate a sample of a generated image after background subtraction. The number of particles is adjusted to be more than 8 in each interrogation area.

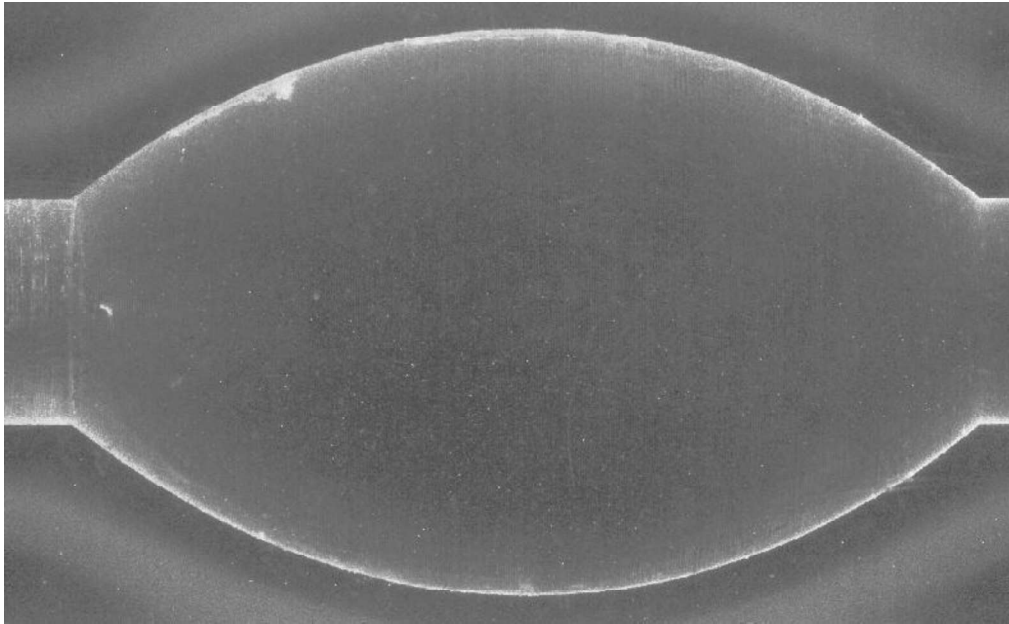


Figure 3.16. A sample of raw image

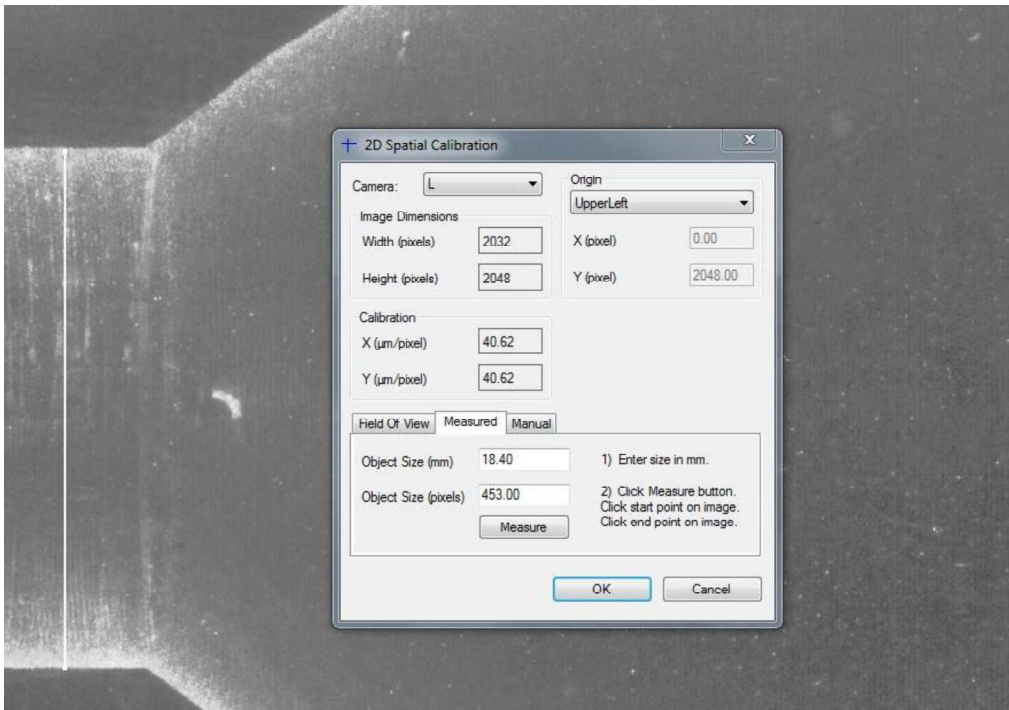


Figure 3.17. The calibration reference in SM (inlet with a diameter of 18.4 mm)



Figure 3.18. The sample image after background subtraction

Then, a processing mask is defined on the images. Due to high reflection from walls, the masks are selected in the inner area of the bulge, as shown in Figure 3.19. Next, the default processor of the Insight4G, with the Nyquist Grid engine with an interrogation area of 32×32 pixels, is selected. The grid size in the SM experiments is 1.296 mm and for PSM is 1.654 mm. However, since this method sets the x and y spacing equal to half of the grid height and width, it gives vectors with 50% overlap. Hence, the vector grid sizes are 0.648 mm and 0.827 mm. Figure 3.20 shows the interrogation area of 32×32 pixels in two frames of an image pair. Cross-correlation measures the velocity vectors in each interrogation resulting in a vector map (Figure 3.21).

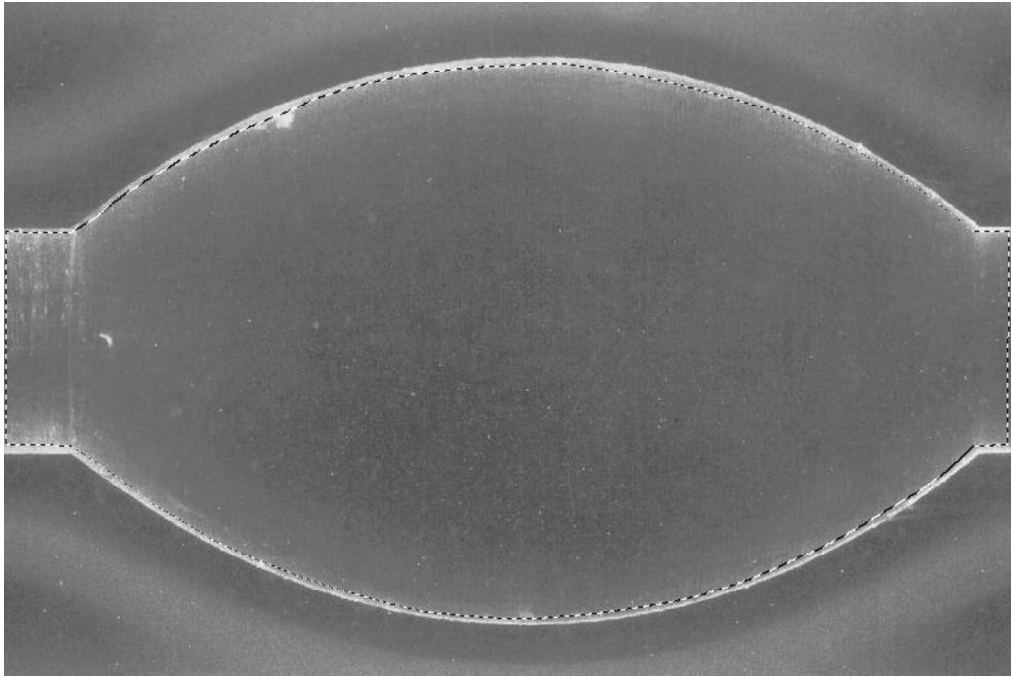


Figure 3.19. The selected mask as the processing area

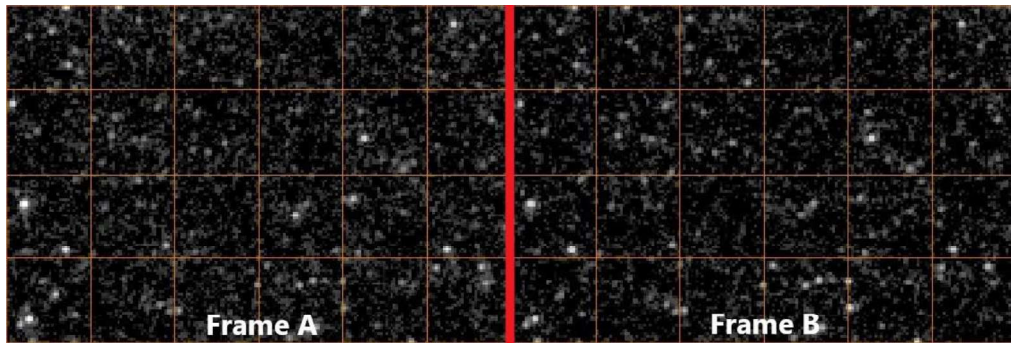


Figure 3.20. Particles in the interrogation area, two frames of an image pair

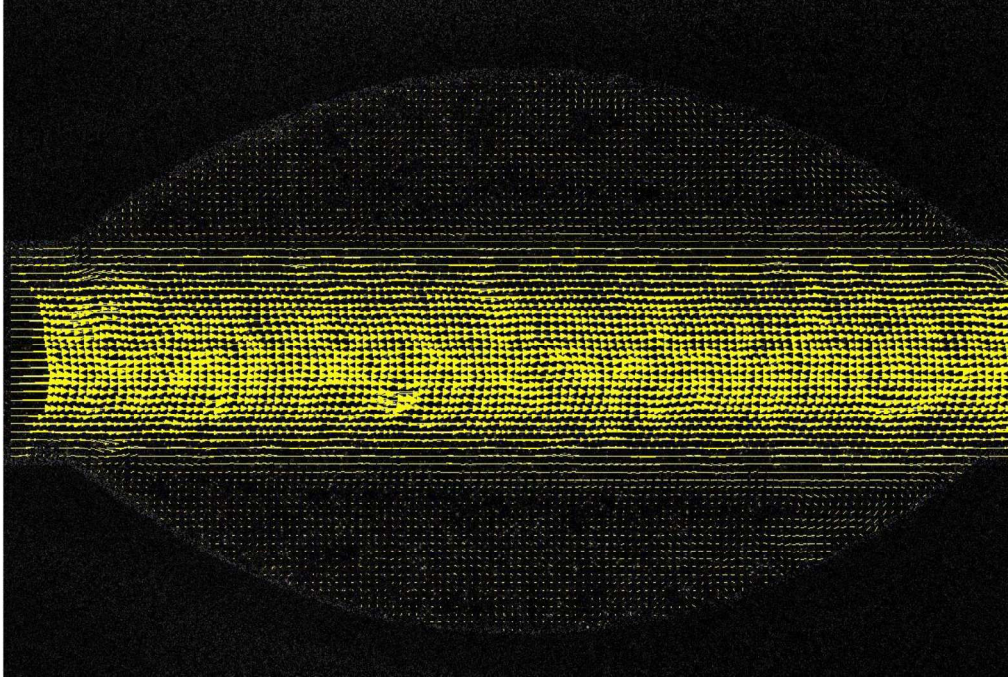


Figure 3.21. Velocity fields generated from an image pair

These vector files are transferred to the TecPlot360 software to calculate the average velocities of the images (average field). This average field consists of velocity vectors and coordinates (Figure 3.22). After assigning the field variables (velocity data in x and y direction), vorticity magnitudes, Q criterion, and swirling strength (λ_{ci}) criterion can be calculated in TecPlot360. These contours and axial velocity contour and streamline pattern are employed to identify flow structures. Also, a comparison between the results of the Q and λ_{ci} is discussed in the next chapter.

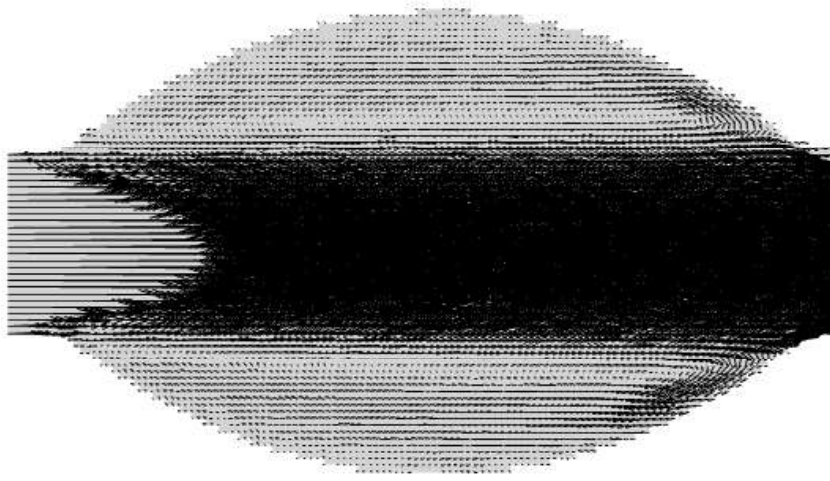


Figure 3.22. The averaged velocity map

Streamline patterns can assist us in characterizing flow structures and possible vortices; however, the most significant setback of this method is that the particles may not fully circulate in the vortex core (Figure 2.13)

Vorticity refers to twice the rotation of the fluid at a certain point which is also defined as the curl of the velocity (equation 2.4). In the method of identifying vortices by employing vorticity magnitudes, the areas which exceed a specified threshold are defined as vortices. This method also carries the challenge of failing to distinguish the shear layers and vortices.

Swirling strength (λ_{ci}) is a criterion of the intensity of the swirling motion. This index refers to the complex eigenvalue of the characteristic equation of the velocity gradient tensor (equation 2.6, 2.7, and 2.8)

Q criterion is the second invariant of the characteristic equation of the VGT (equation 2.7). This technique identifies the vortices by characterizing the flow events as streaming, convergence, and Eddie regions. This method identifies areas with Q larger than zero as vortices [44].

To check the consistency of the results, the experiments were repeated, and the deviations in flow rate measurements and the maximum values of velocities and swirling strength were reported. Considering the 12 phases of the cycle, it was found that the maximum of 4% deviations in flow rates and the maximum of 9% deviations in velocity magnitudes and swirling strength were obtained.

CHAPTER 4

RESULTS AND DISCUSSION

This chapter presents the results of the PIV measurement of the flow structures in simple and patient-specific models. Streamlines, velocity magnitudes, vorticity magnitudes, swirling strength (λ_{ci}), and Q criteria are analyzed to understand the flow fields in detail.

4.1 Simple Model

A physiological flow (presented in table 3.2 in detail) is simulated in SM for this study. This pattern has a period of 1 second with a flow range of 4-68 (ml/s), miming a close-to-real flow pattern.

Phase-averaged axial velocity contours, streamline patterns, vorticity contours, and the flow's swirling strength (λ_{ci}) are reported to identify the flow forms. Figure 4.1 and Figure 4.2 show the axial velocity contours in the phases mentioned earlier. The jet flow in the middle of the aneurysm is surrounded by lower velocity contours that can be observed in most phases.

To understand the flow better, the overall flow structure in one cycle should be considered. A high axial velocity jet flow surrounded by negative axial velocity, which can be a sign of vortex, is entered the bulge at phase 3 and moves forward until the end of the cycle. This flow continues to lose its strength and moves again forward at the beginning of the next cycle. When this high-velocity core gets to the distal end, hits the walls and gains its strength back (phase7), and vanishes at phase 8. From phase 2 to phase 3&4, the high difference between the axial velocity at the inlet is due to the high acceleration rate at the beginning of the cycle.

In some of the phases, there is a small low-velocity region at the inlet of the bulge. This flow is valid due to the high Womersley number of the flow pattern. (Figure 2 .12)

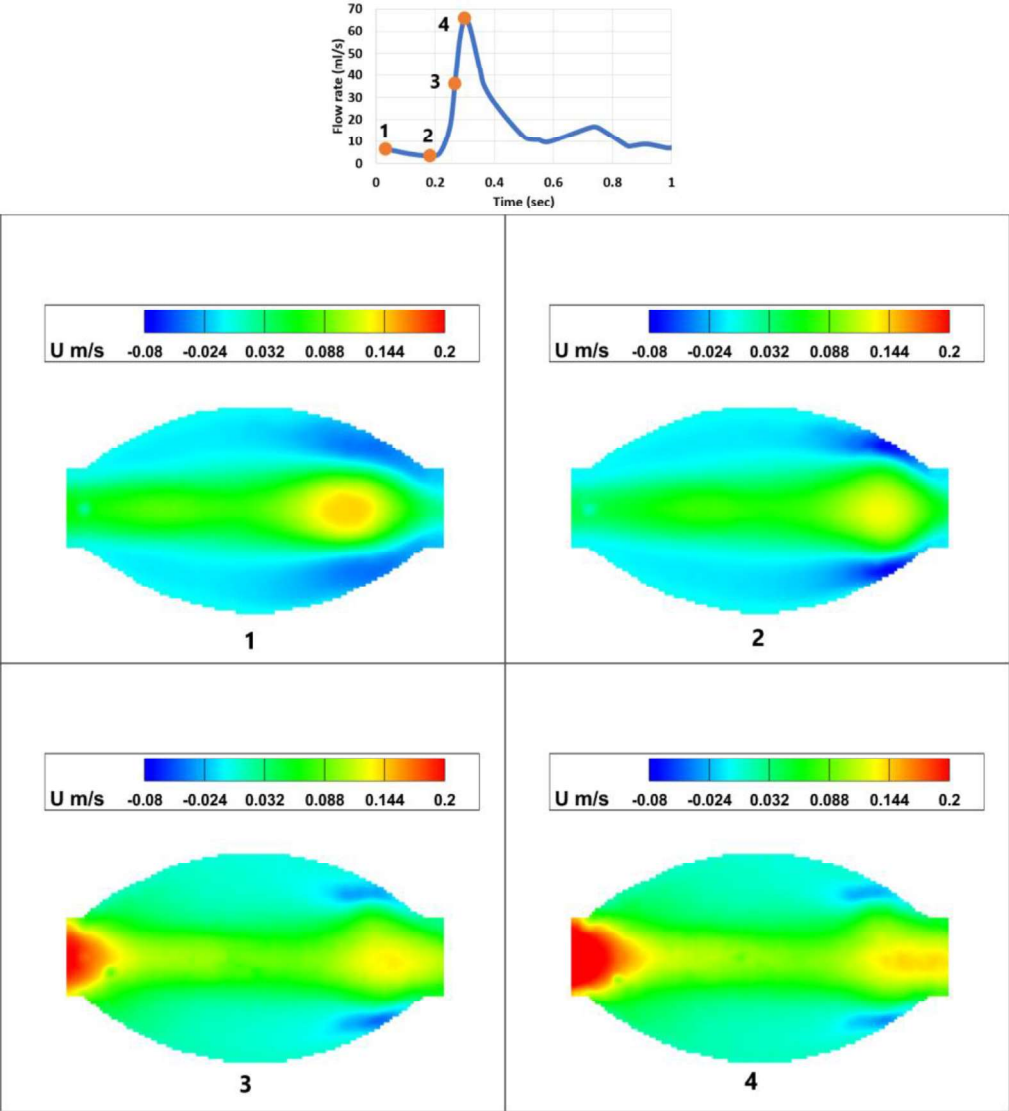


Figure 4.1. Axial velocity contours at the acceleration part, SM

Flow structures show a highly symmetric behavior in most of the phases. It can be concluded that the high axial velocity region has a lower velocity at the deceleration part of the flow. In most cases, there are two high negative axial velocity regions at the top and bottom of the jet flow.

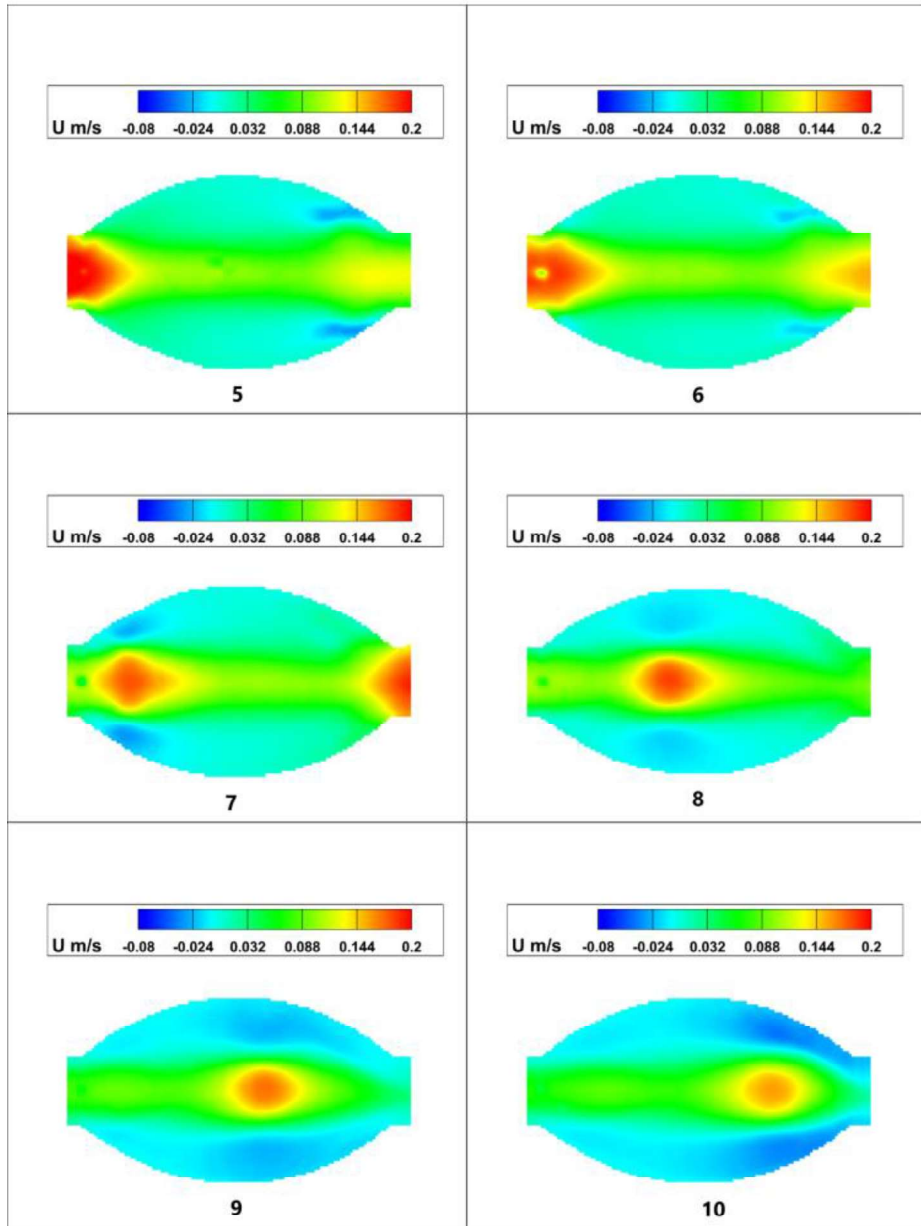
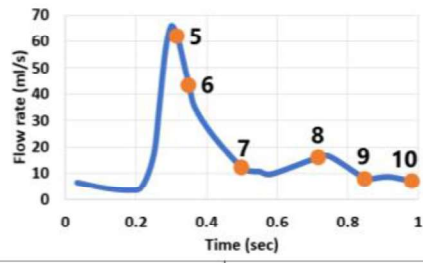


Figure 4.2. Axial velocity contours at the deceleration part, SM

To illustrate further, Figure 4.3 and Figure 4.4 exhibit the streamline patterns at the intended instants.

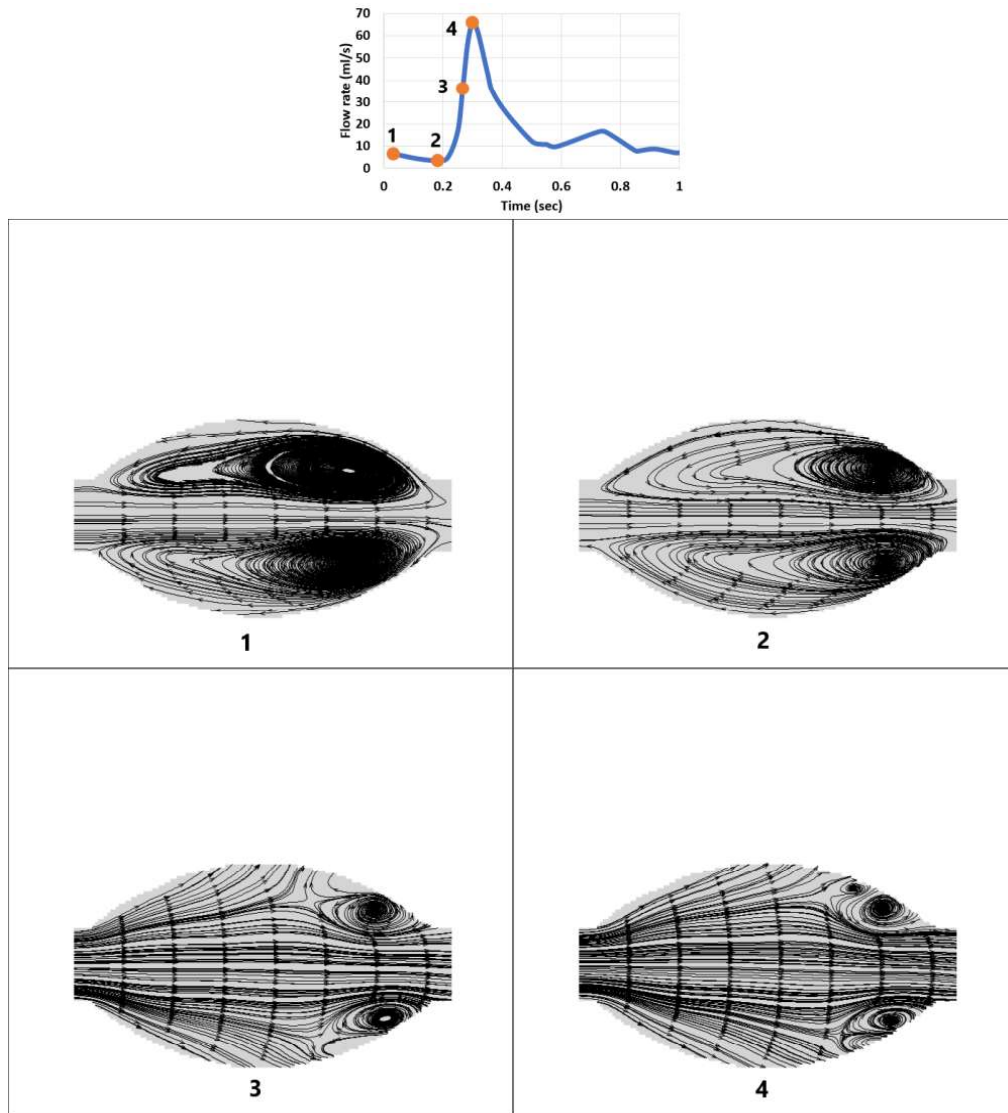


Figure 4.3. Streamline patterns at the acceleration part, SM

As predicted from axial velocity contours, two forward-moving vortical structures are distinct up and below the jet flow area. The primary whirling form initiates at phase 7 and moves downstream of the aneurysm. As this structure approaches the distal end, at the end of the cycle, phase 9, another whirling flow form is formed at the diverging part of the bulge.

The second vortical structure vanishes at the beginning of the next cycle. But when the primary one collides with the wall at the distal end in phase 2, it collapses and divides into two vortical flow forms (phases 3&4).

By deceleration starts, the upstream flow encounters these whirling forms in phases 5 and 6 and finally overcomes them. Complex flows are observed in the separation section, bulge outlet, and primary potential vortex division.

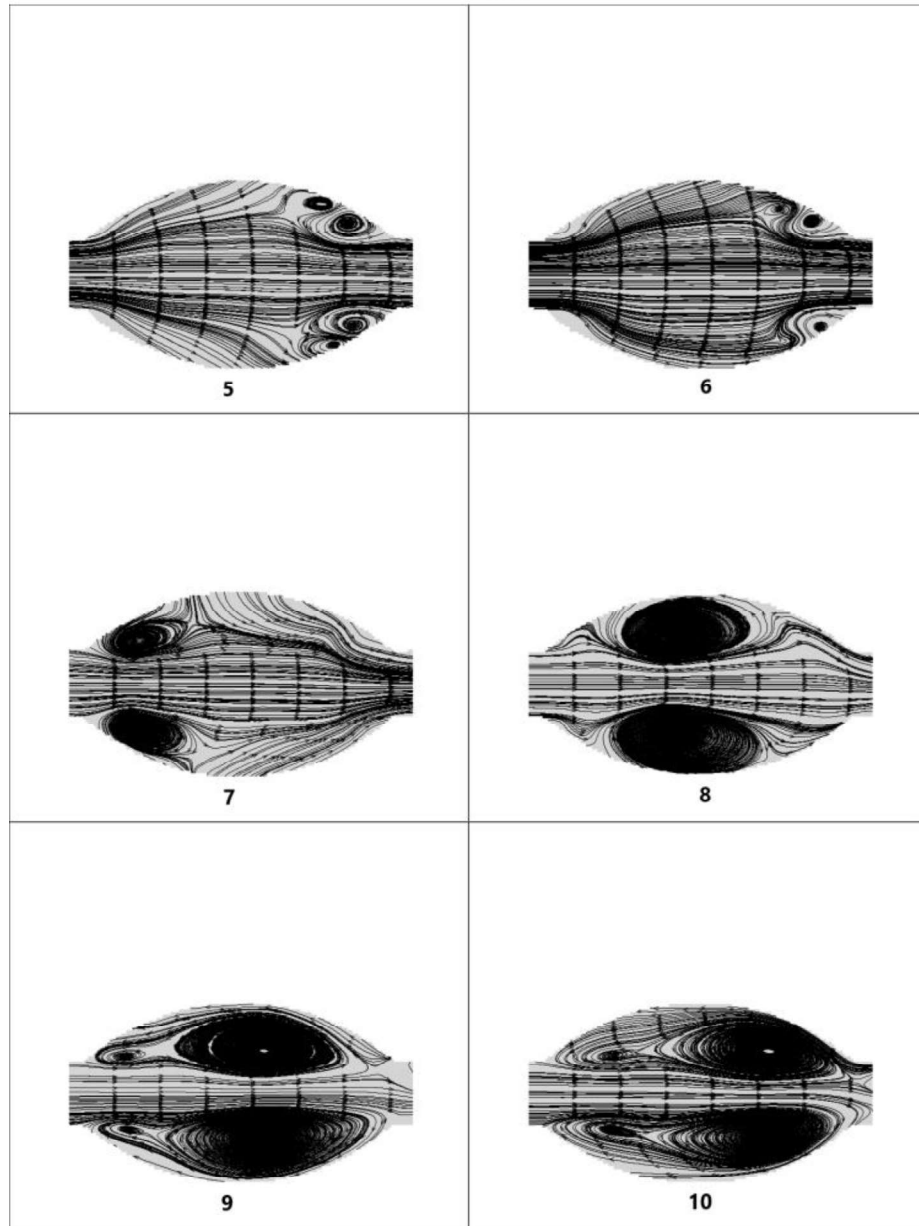
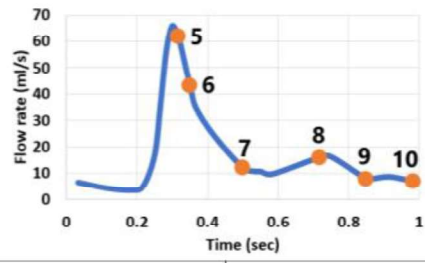


Figure 4.4. Streamline patterns at the deceleration part, SM

To investigate the flow structures further, vorticity and swirling strength (λ_{ci}) are analyzed afterward. Figure 4.5 and Figure 4.6 are the vorticity contours for the studied phases.

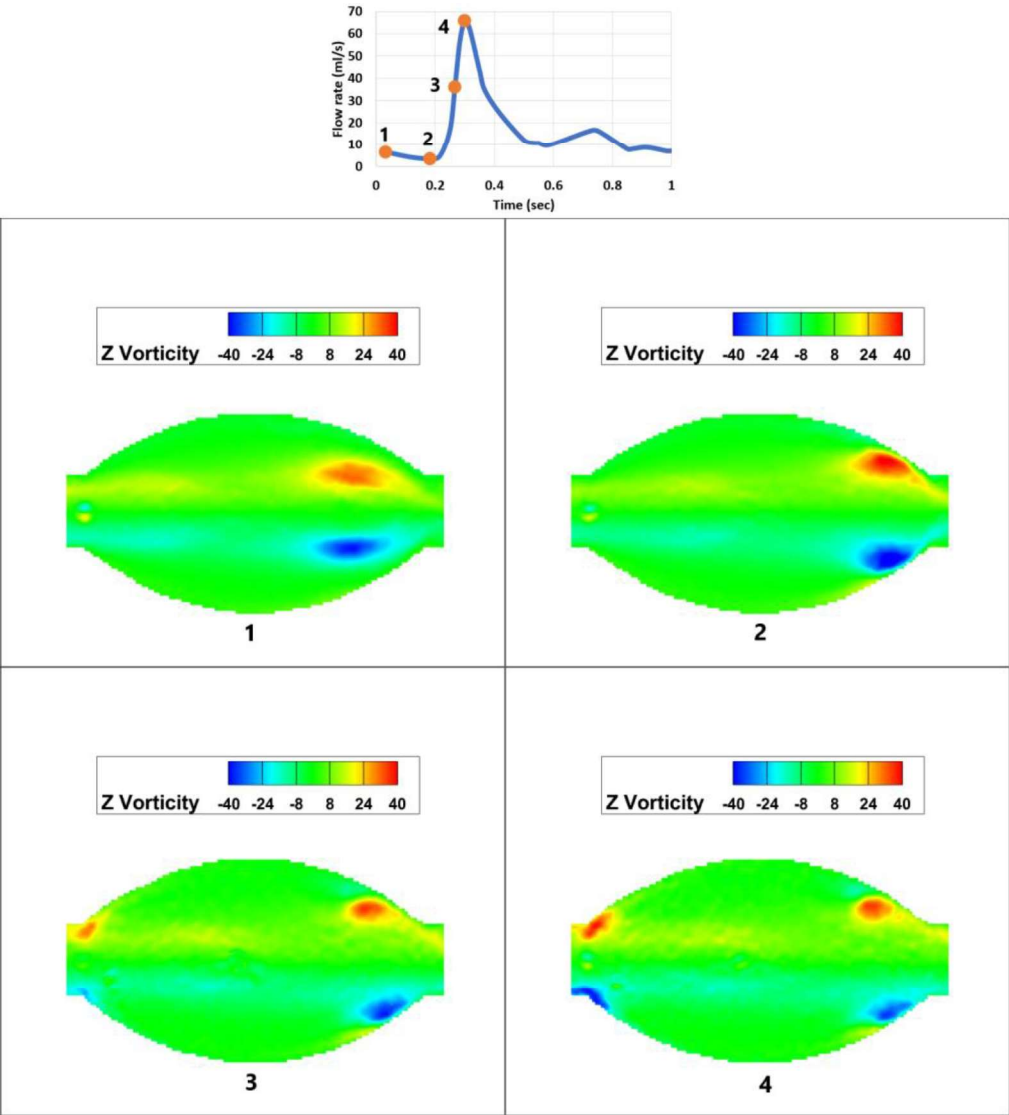


Figure 4.5. Vorticity contours at the acceleration part, SM

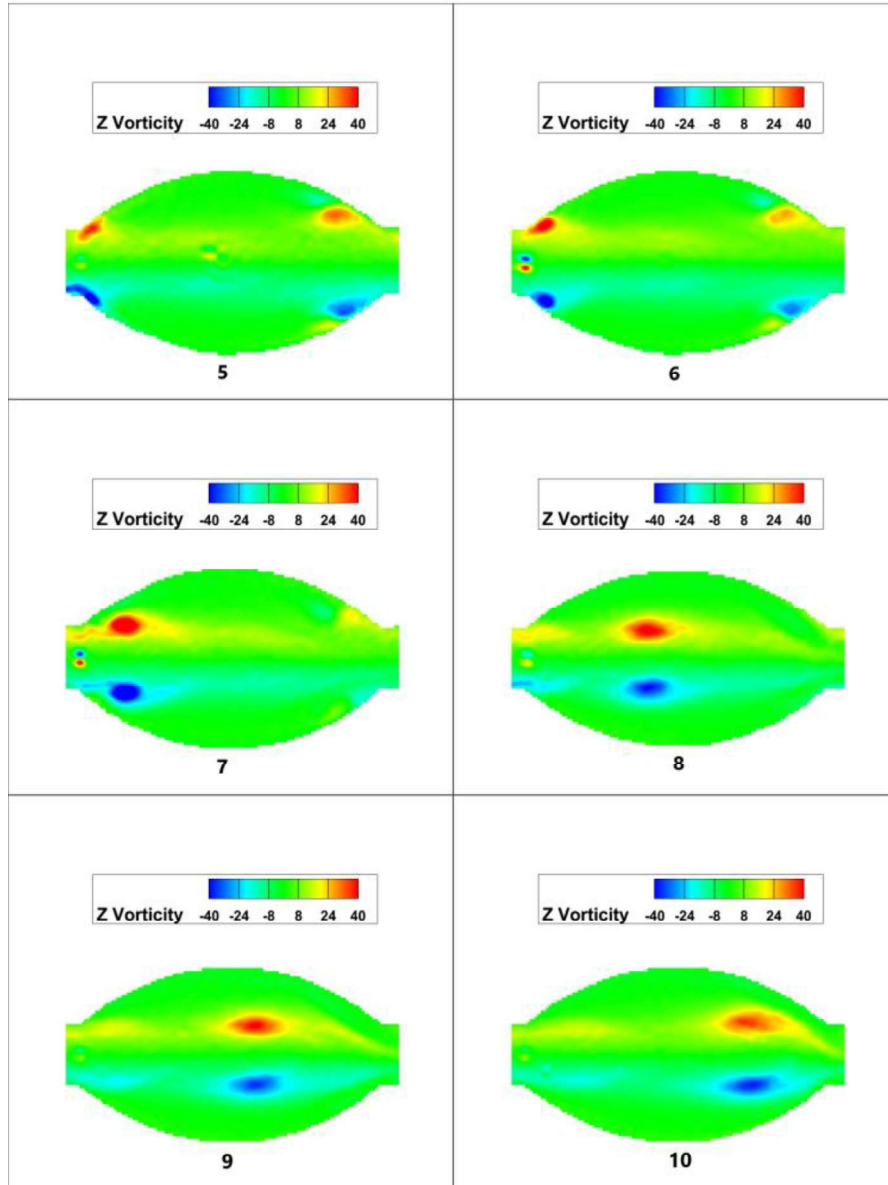
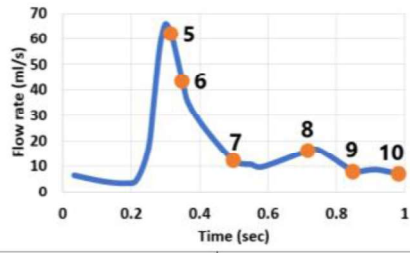


Figure 4.6. Vorticity contours at the deceleration part, SM

Despite the disadvantage of not distinguishing potential vortex cores from the shear layer, the high vorticity regions were consistent with the identified vortical structures based on streamline patterns in most phases.

In phase 3 of the acceleration part, an area with high vorticity magnitude appears at the flow separation part at the inlet of the bulge. This area increases in vorticity magnitude, and finally, during phase 7, it separates from the wall and moves forward to the distal end. These areas are consistent with the primary whirling flow's location. These vortical structures hit the converging part of the wall at phase 2 of the next cycle, and their vorticity decreases in magnitude. These primary flows are surrounded by a high vorticity area of opposite value (distal end of phases 3,4,5, and 6). In most cases, a vorticity couple in opposite directions emerges at the bulge area's entrance, consistent with the low axial velocity fields at the inlet.

A physiological flow pattern is a pulsatile flow, so the consequences of a flow structure in one cycle carry on to the next. This effect is visible when the primary vortex initiated at phase 3 vanishes in the next cycle, phase 8.

Figures 4.7 and 4.8 display the swirling strength of the flow.

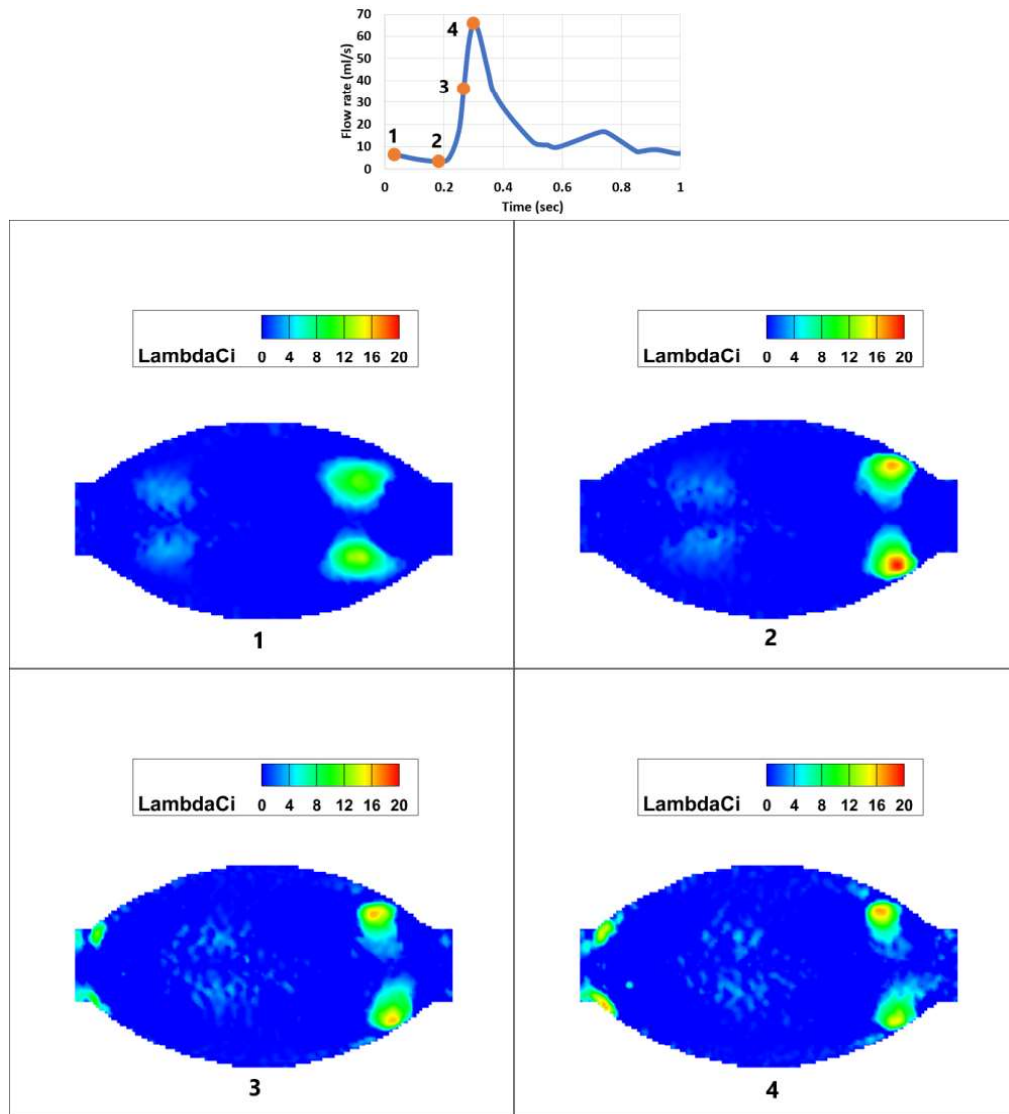


Figure 4.7. Swirling strength (λ_{ci}) at the acceleration part, SM

The first observation is that areas with high swirling strength (λ_{ci}) are similar to areas with high vorticity magnitudes. The primary vortex is initiated at the inlet of phase 3 and increases strength by phase 6. This vortex is detached from the wall at phase 7, moves forward, and hits the wall in phase 2 of the next cycle.

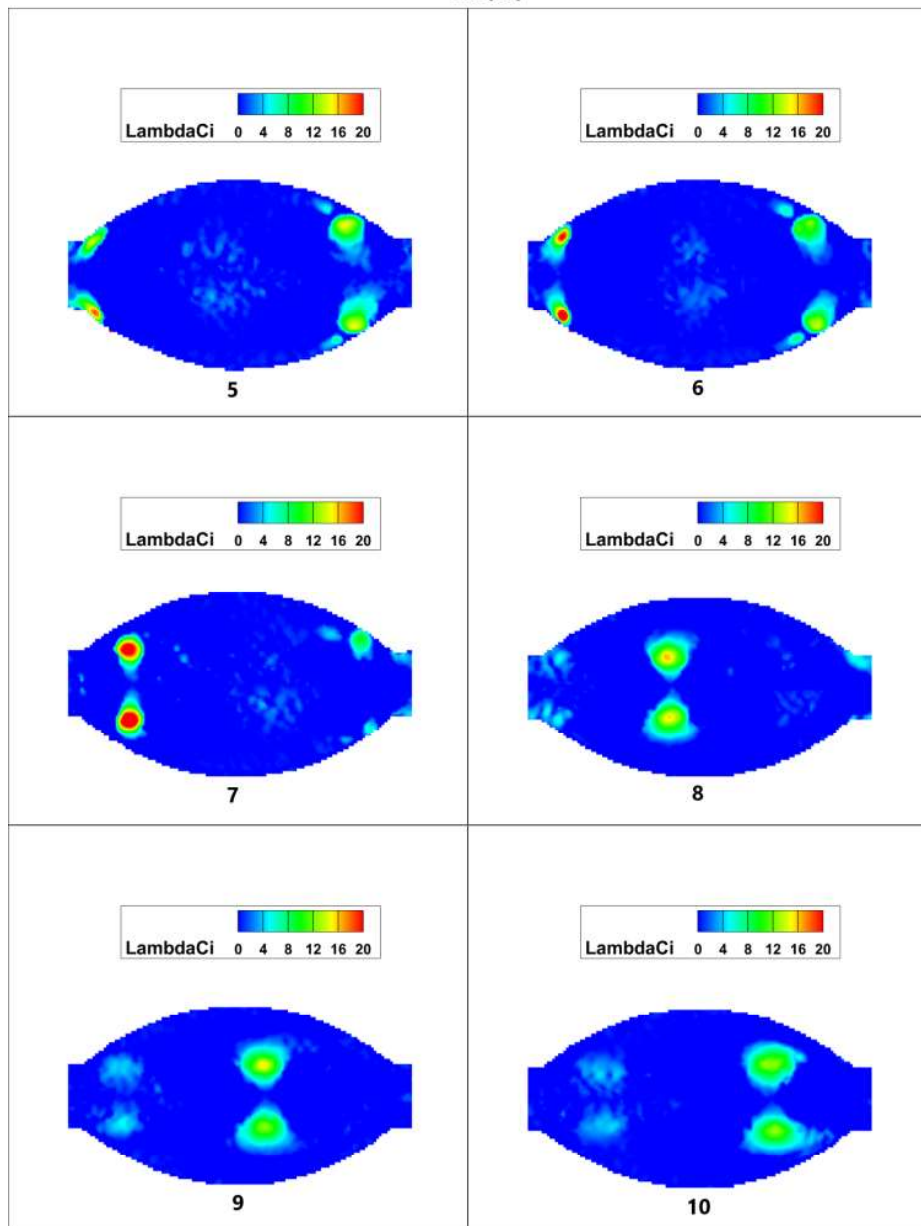
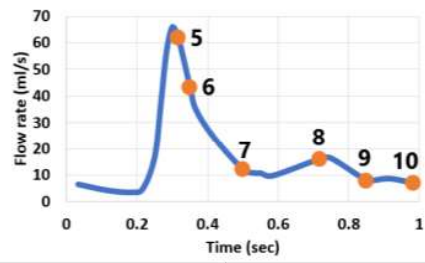


Figure 4.8. Swirling strength (λ_{ci}) at the deceleration part, SM

This collision increases the swirling strength at the center of the vortex. A reduction of the λ_{ci} occurs after the emergence of the following primary vortex in phase 3. Like vorticity contours, an area of high swirling strength is detected in the neighborhood of the vortex at the distal end (phases 4,5 &6). This area is a determiner of the second vortex. A symmetric region of high swirling strength has entered the bulge at phase 8. In the course of the deceleration part, this region moved forward. However, in the acceleration part, this region defuses in intensity and collapses from phase 2 to phase 6.

Figure 4.9 compares the λ_{ci} and Q criteria in phase 1. As illustrated in this figure, the areas with positive Q are the same as those with high λ_{ci} , indicators of vortices. This consistency is evident in the other phases too.

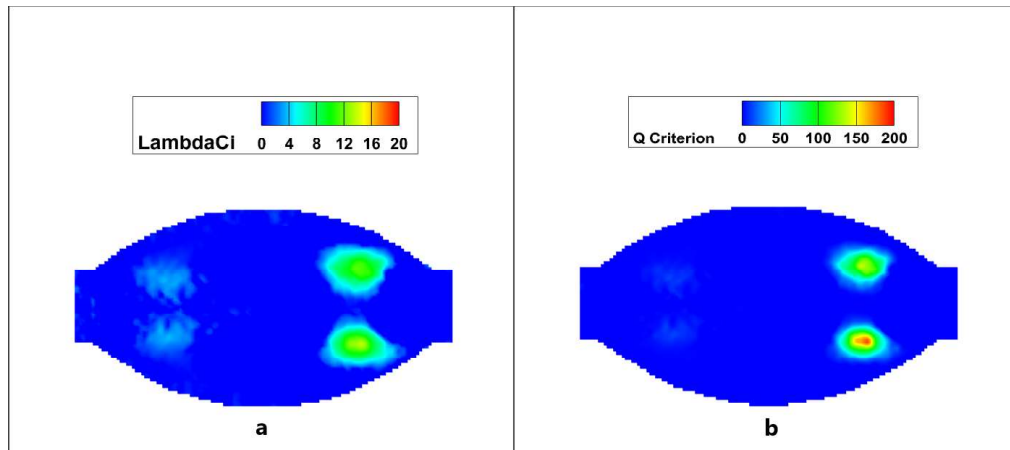


Figure 4.9. a) Swirling strength of the flow filed in the first phase b) Q criteria of the flow filed in the first phase in SM

4.2 Patient-Specific Model

In this model, flow structure in three planes (Figure 3.7) is investigated in a physiological flow. The properties of the flow pattern are tabulated in table 3.2. as mentioned before, experiments are conducted in twelve instants of the flow pattern. Based on the importance of flow evolution, only ten of them are presented below. As we expected, the velocities, vorticity magnitudes, and swirling strength (λ_{ci}) of the flow fields reduce in magnitude as the target planes proceed to the bulge. Hence, to detect the flow patterns, more minor legends are selected for plane2 and plane3, respectively, compared to plane1.

4.2.3 Plane #1

The aim area of plane #1, as shown in Figure 3.8.a, is more significant than other planes. Only the bulge portion is studied to keep the resolution high enough to capture quality images. Axial velocity contours, streamlines, vorticity contours, and swirling strength (λ_{ci}) of the flow are presented in sequence to specify the vortical structures in the flow. Figure 4.10 and Figure 4.11 show the axial velocity contours in the target instants.

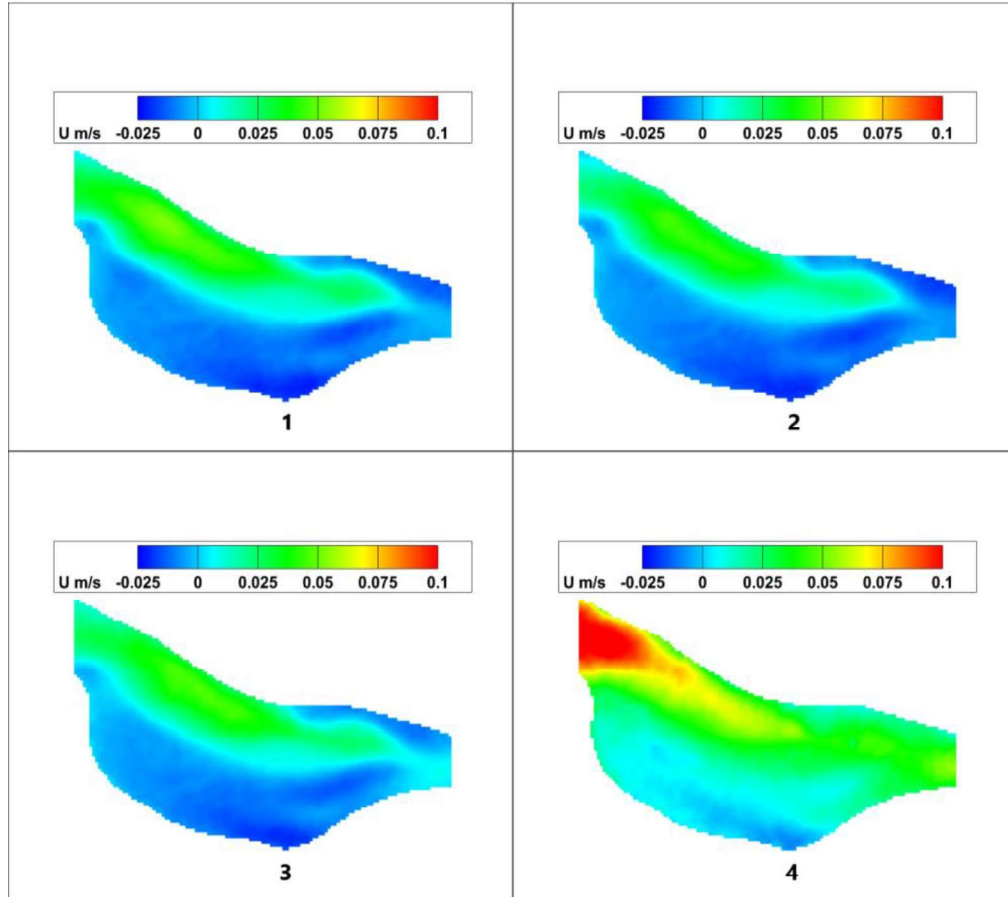
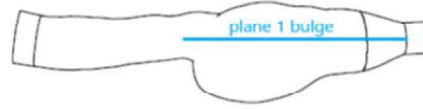
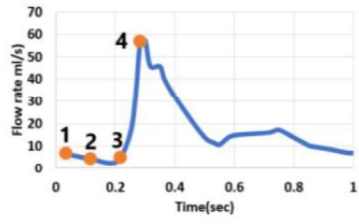


Figure 4.10. Axial velocity contours at the acceleration part, PSM, plane #1

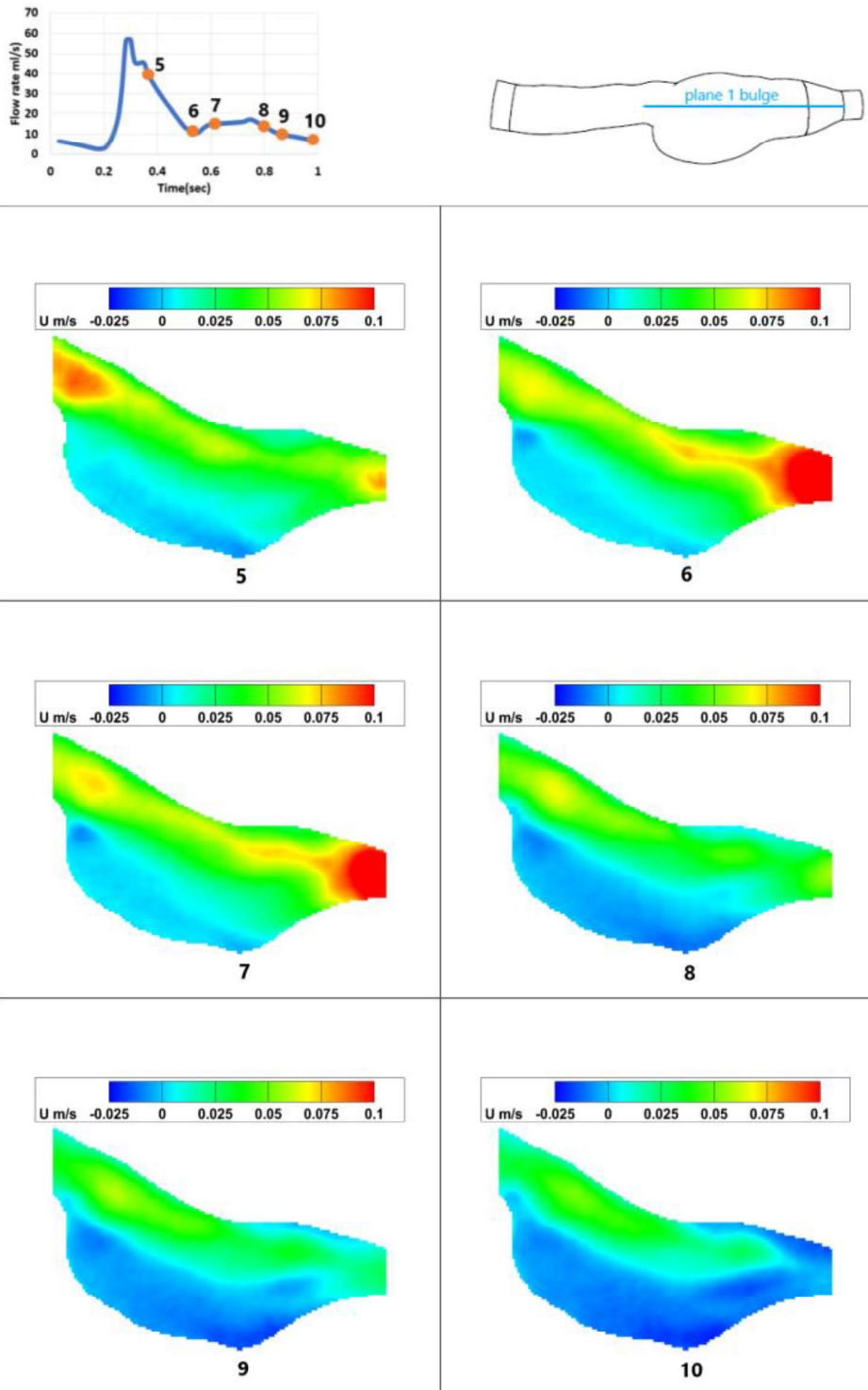


Figure 4.11. Axial velocity contours at the deceleration part, PSM, plane #1

The jet flow is crossed through the bulge portion as expected, but negative axial flows are visible at the outlet of the aneurysm. These backflows are mostly in phases with a low flow rate calculated at the inlet of the aneurysm.

A high-velocity region has entered the bulge at the top of the acceleration part with maximum flow rate, phase 4. Starting from the deceleration part, the axial velocity at the inlet decreases at phase 5. Phases 6 and 7 are the instants at deceleration, where the flow at the outlet area increases in axial velocity.

A second high-velocity region entered the bulge in phase 7. This flow does not move further, stays at the same position, and decreases in magnitude at the beginning of the next cycle. Flow separation occurs at the diverging part of the anterior wall, leading to an area of lower velocity. As mentioned, the area with a negative axial velocity at the diverging anterior and converging part of the posterior wall can signify vortical structures.

Figure 4.12 and Figure 4.13 show the streamline patterns in the intended phases.

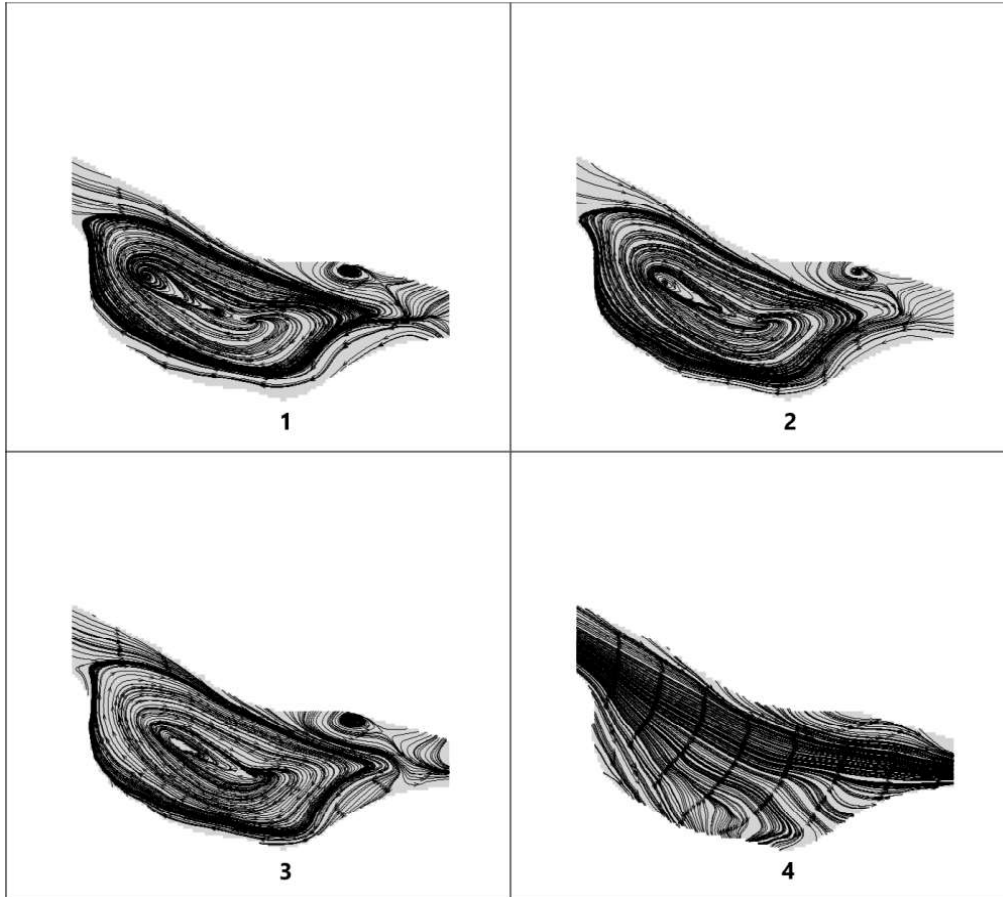
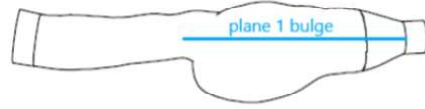
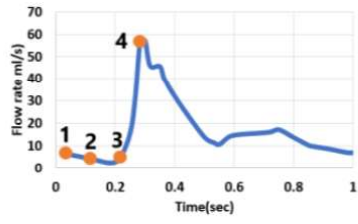


Figure 4.12. Streamline patterns at the acceleration part, PSM, plane #1

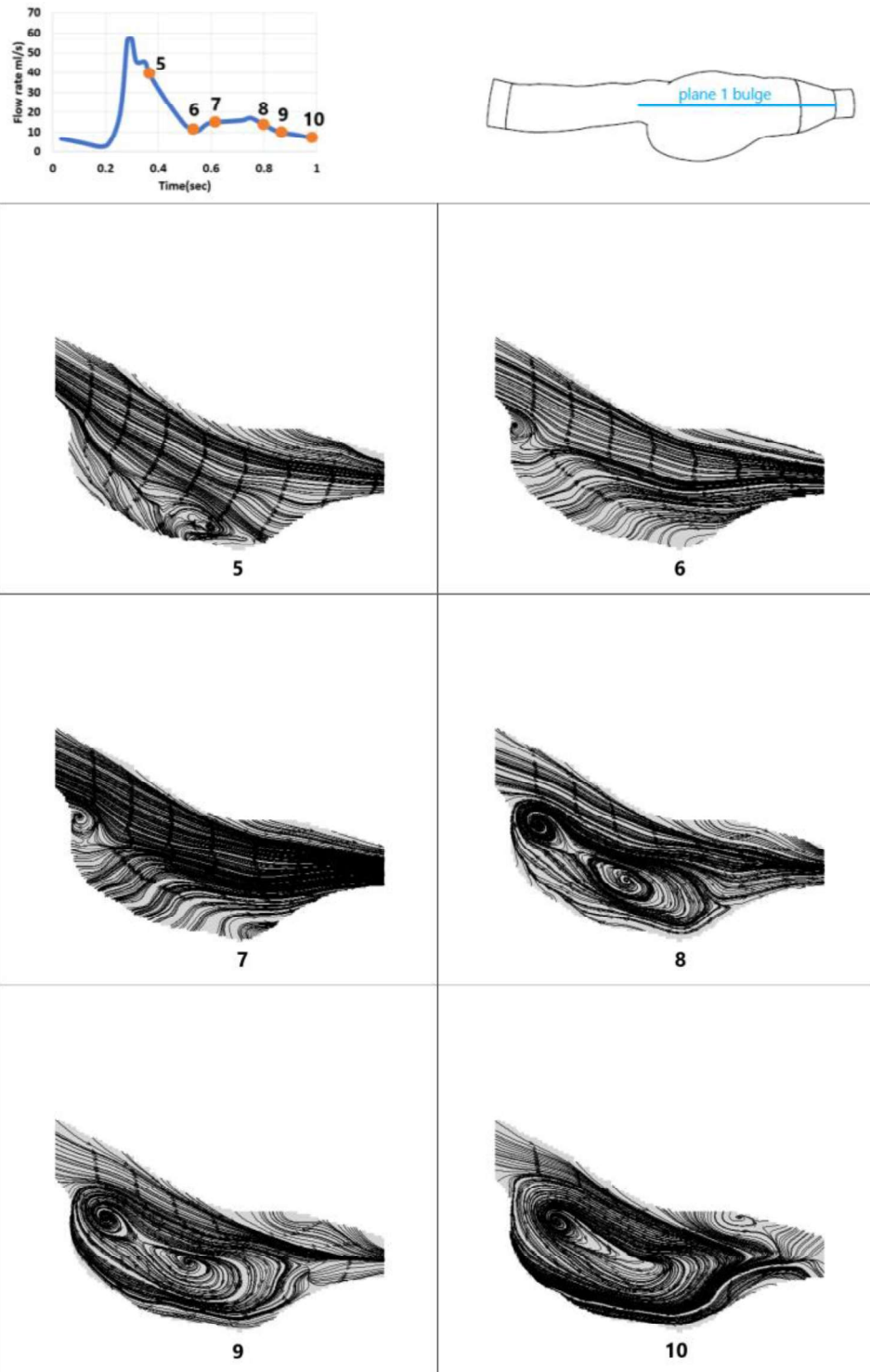


Figure 4.13. Streamline patterns at the deceleration part, PSM, plane #1

Phase 6 in Figure 4.13 shows that streamlines with a vortical pattern initiate at the separation part of the posterior inlet wall. This structure detaches from the wall in phase 8 in the presence of another whirling flow at the converging area of the rear wall. The first sign of the second whirling flow form is roughly visible in the same place in phases 6 and 7. Complicated flow patterns arise at the encountering location of these structures. The second whirling flow loses intensity at the end of the deceleration part and finally vanishes at the beginning of the acceleration part of the next cycle.

At the end of the deceleration part, phase 10, a third vortical flow structure is visible in the anterior area. This flow also vanishes at the end of the acceleration part of the next cycle. The streamlines in the opposite direction of the mainstream are consistent with the negative axial velocity areas.

In the first and last phases of the cycle, with the minimum flow rate, the backflow at the outlet of the aneurysm occurs. These are phases in which the third vortical pattern has appeared.

In the phases where two whirling flow forms are visible, the streamlines circulate in a bigger diameter around their cores. This circulation occupies most of the bulge area. Flow separation at the distal end of the bulge causes complex streamline patterns in phases like phase 1.

Vorticity magnitudes and swirling strength (λ_{ci}) will assist us in understanding the flow structure and especially vortexes. Figure 4.14 and Figure 4.15 show the vorticity magnitude contours in the discussed phases.

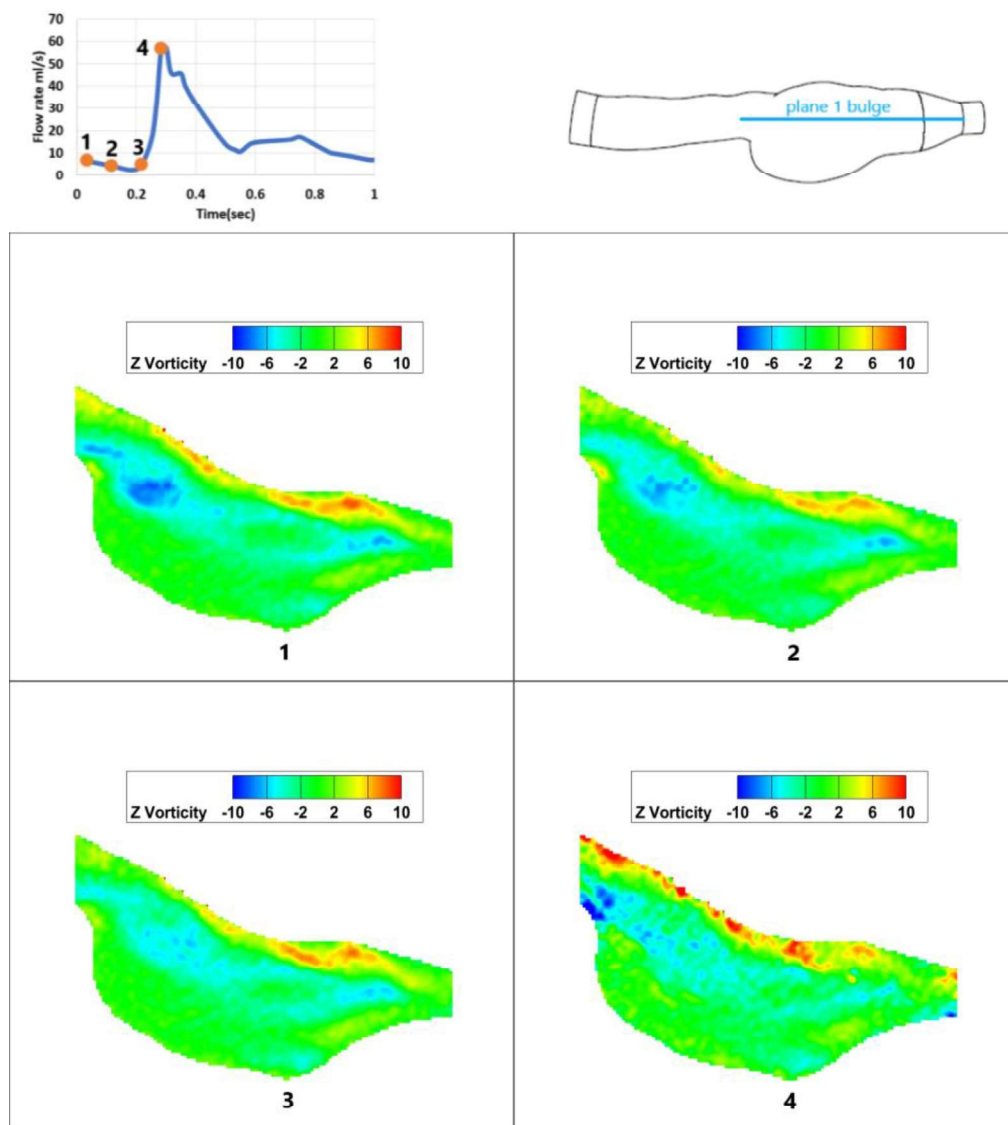


Figure 4.14. Vorticity contours at the acceleration part, PSM, plane #1

At the end of the acceleration part phase4, beside the shear layers at the anterior wall, a high vorticity region has evolved at the diverging part of the posterior wall. Along with the deceleration part, this vortex detaches from the wall, moves forward, and loses its intensity. Finally, at the beginning of the next cycle, it collapses to a larger area of lower vorticity. This area is consistent with the streamline patterns' first vortical structure in phase 6.

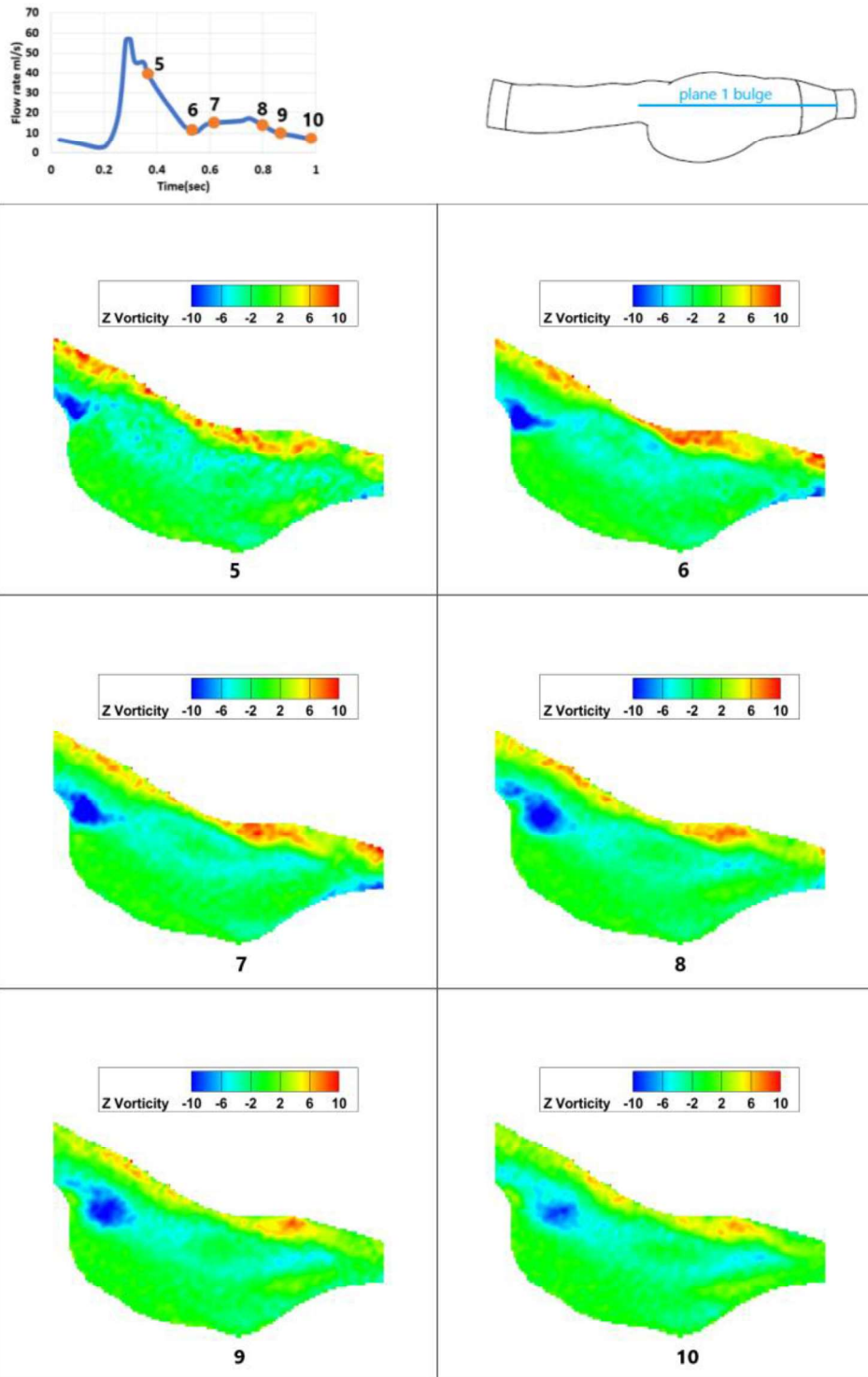


Figure 4.15. Vorticity contours at the deceleration part, PSM, plane #1

Starting from phase 6, an elliptic area with lower vorticity magnitudes surrounded by another vortical circle of high vorticity appears. This area is evident at most phases and moves forward along with the primary vortex.

It is challenging to distinguish vortices from shear layers at the separation area of the anterior wall. However, evaluation along with streamline patterns can ease this challenge. Considering this, as mentioned before, a vortical flow structure appears in this area in phases 1, 2, 3, 9, and 10 via streamlines. The high vorticity area in these phases can be a determinative factor for vortices.

At the converging part of the rear wall, during the acceleration part, and end of the deceleration part, two areas with high vorticity emerge in opposite directions. Vorticity counters also show that the primary vortex has the maximum vorticity magnitude in phases 6, 7, and 8 and almost vanished at the end of the acceleration part phase 4. In some phases, high vorticity areas close to the outlet wall appear. However, no vortical flow appears in these areas considering streamlines.

Due to the complex geometry, the flow structure is affected by the slightest change in the wall. For instance, the anterior wall has converged slightly before the diverging area. Either the streamlines or vorticity magnitude did not provide any additional information about the flow structure in this area.

Figure 4.16 and Figure 4.17 exhibit the swirling strength (λ_{ci}) contours in studied instants.

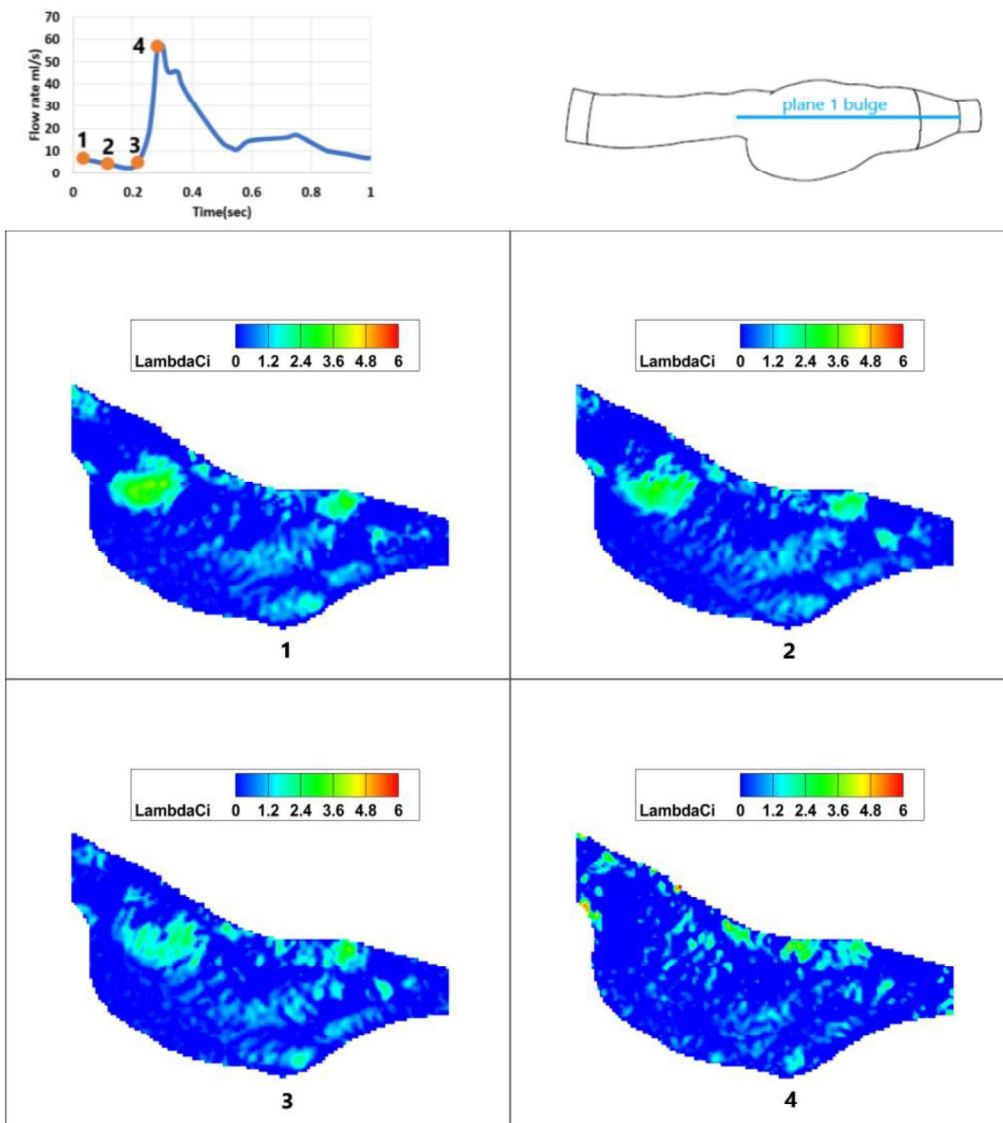


Figure 4.16. Swirling strength (λ_{ci}) at the acceleration part, PSM, plane #1

The first sign of the primary vortex develops at the point of the diverging frontal wall. This vortex is detached from the wall in phase 6 and moves farther during the cycle. This evolution is also solid based on the vorticity magnitudes. Maximum swirling strength happens at the core of the vortex in phase 7. This flow pattern loses its intensity till the next cycle's acceleration part and finally vanishes in phase 4.

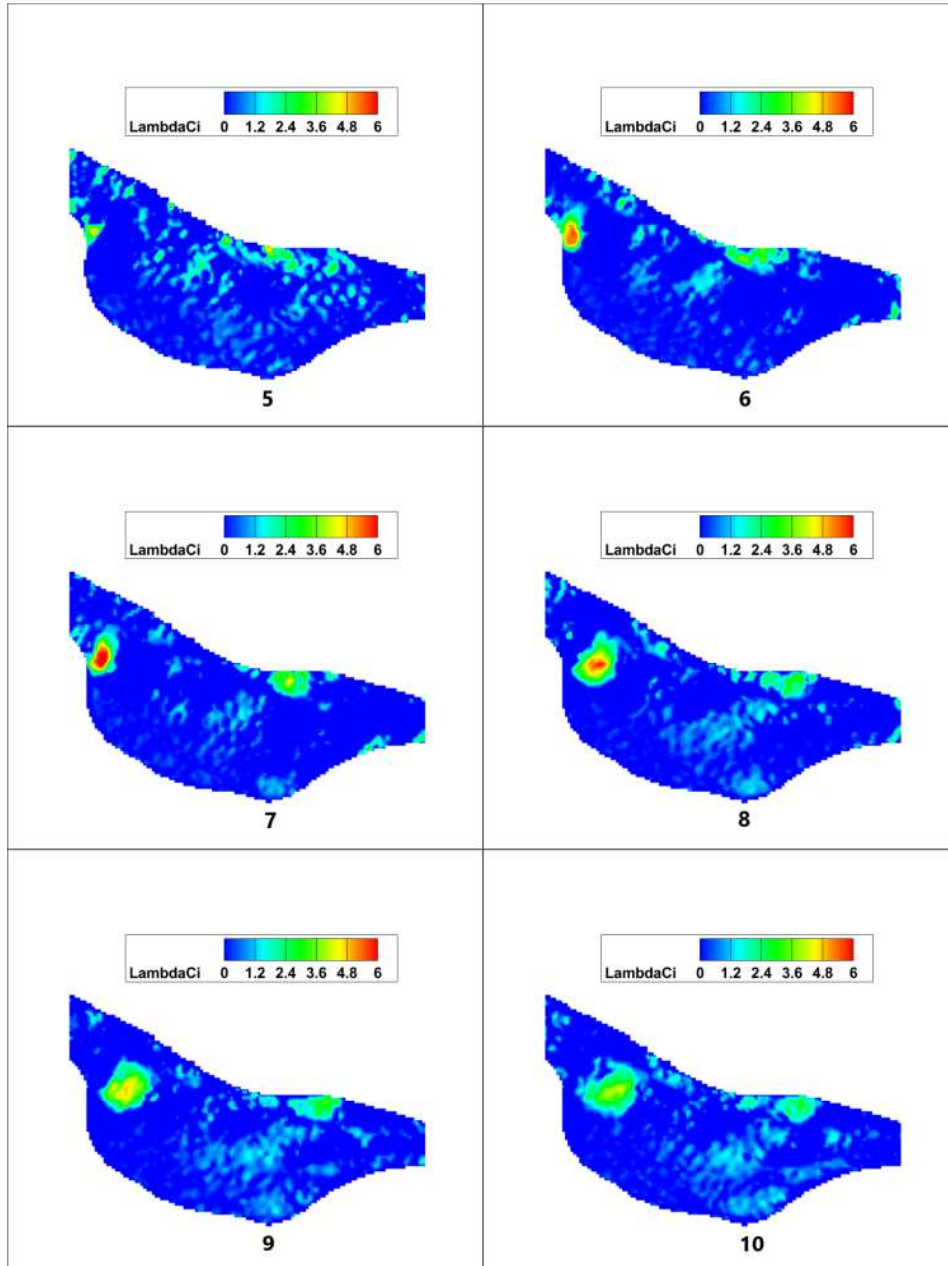
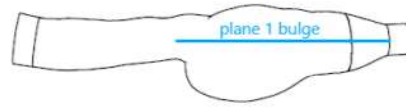
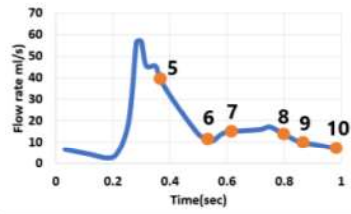


Figure 4.17. Swirling strength (λ_{ci}) at the deceleration part, PSM, plane #1

Swirling strength (λ_{ci}) is high in most cases at the diverging part of the anterior wall. But it decreases in magnitude in phases 4 and 6 when the flow starts decelerating. Maximum swirling strength in this region also happens in phase 7. The core of this whirling from stands still along the cycle. At the starting point of the posterior wall converging, a high λ_{ci} region appears in most phases. This region has the maximum intensity at the acceleration part. However, the occupied area gets more extensive during the deceleration period.

Figure 4.18 compares the Q and λ_{ci} of the flow field (plane #1) in the first phase of the physiological flow. Like the results in SM, the identified vortexes in both methods are consistent with each other. This consistency is evident in the other phases too.

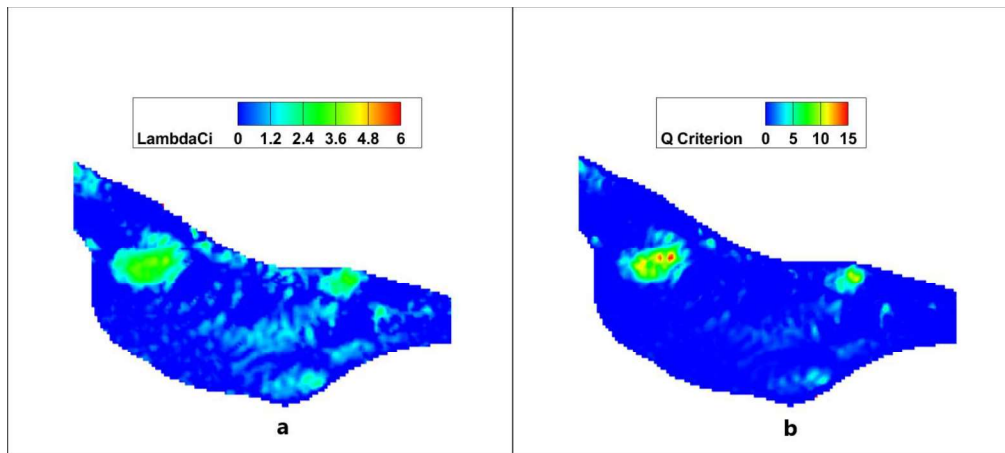


Figure 4.18. a) Swirling strength of the flow field in the first phase b) Q criteria of the flow field in the first phase in PSM

4.2.3 Plane #2

As Apparent in Figure 3.8.b, two interfering regions were formed in plane #2. However, only the highlighted area is considered due to the inadequate optical access to the small site.

Figure 4.19 and Figure 4.20 show the axial velocity contours in the studied phase. At first sight, the velocity magnitudes are lower than the ones in plane #1. A region of high positive velocities at the anterior wall appears in all phases. The core of the mentioned region saves its position during the acceleration part. Starting from phase 4 and transitioning to the deceleration part, the velocity magnitudes increase and the region moves toward the distal end. In phase8, this region vanishes, and an area with negative axial velocities surrounds the positive velocity area. The mentioned negative velocity region expands till the phase2 of the next cycle. In phases 4 and 5, negative axial velocities occur close to the rear wall across the high-velocity region. These can be an indication of a vortex ring.

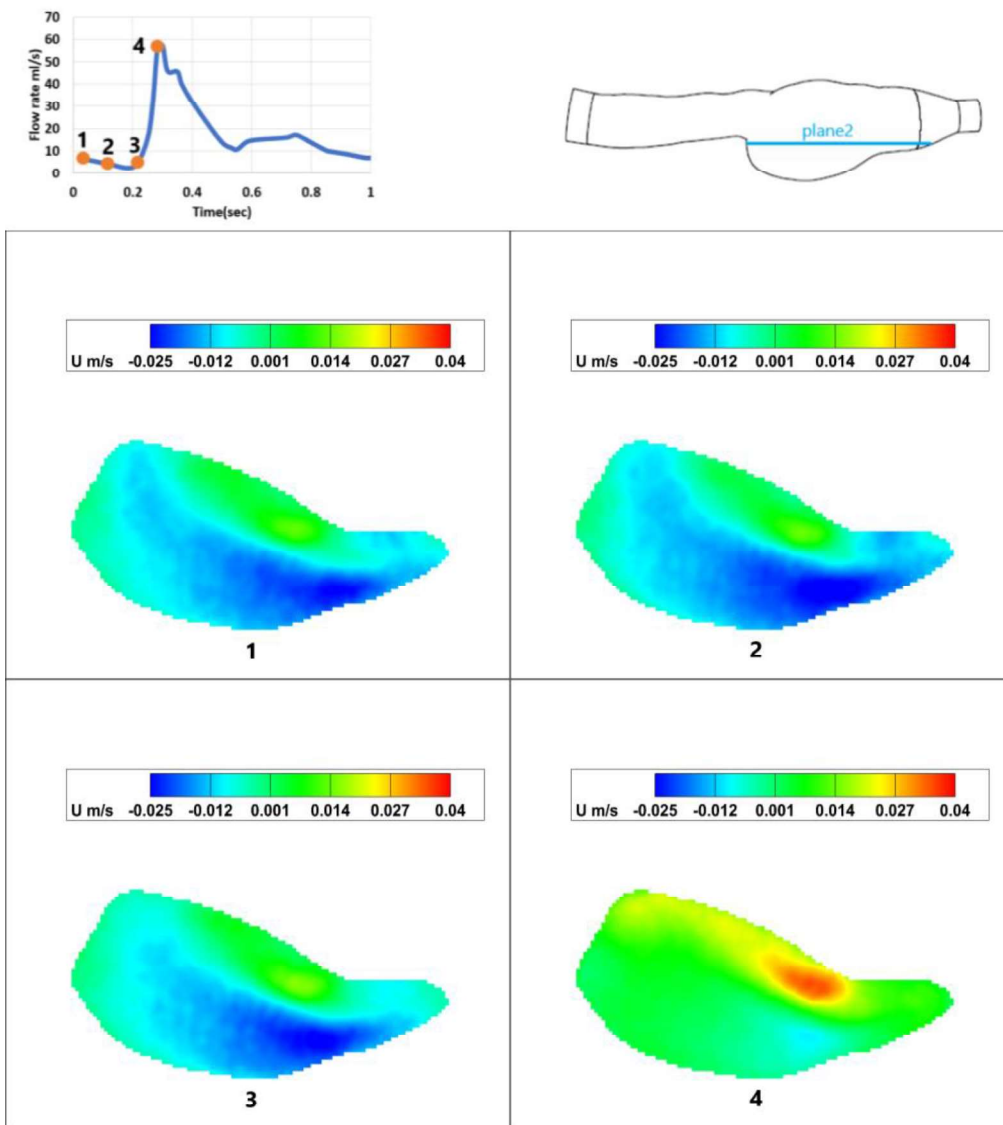


Figure 4.19. Axial velocity contours at the acceleration part, PSM, plane #2

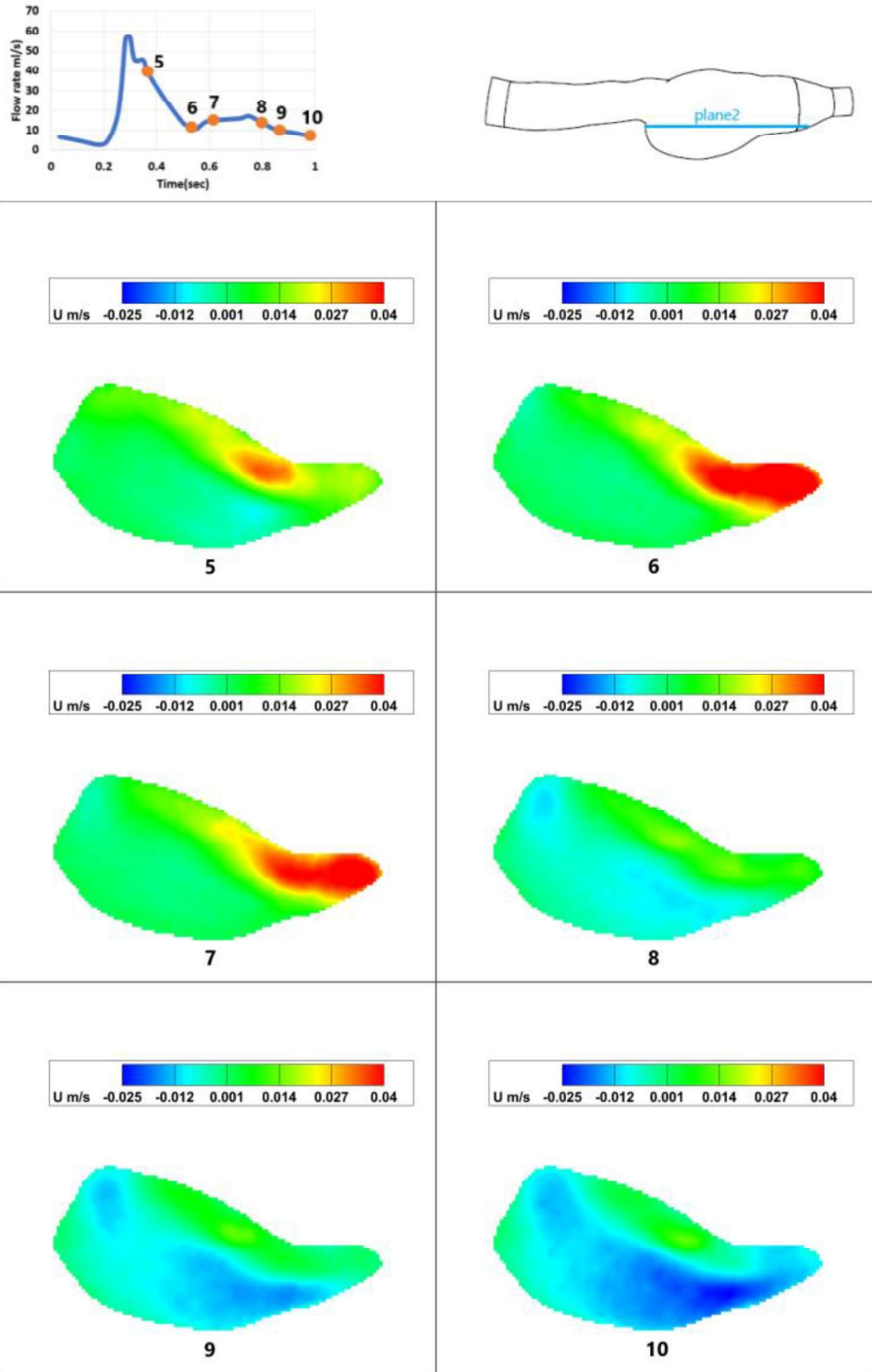


Figure 4.20. Axial velocity contours at the deceleration part, PSM, plane #2

Figure 4.21 and Figure 4.22 show the streamlines in the acceleration and deceleration part of the flow. A whirling form of flow with one core develops in phase8. The second core inside this pattern appears at the beginning of the acceleration part of the next cycle. The second core also disappears at the end of the acceleration part.

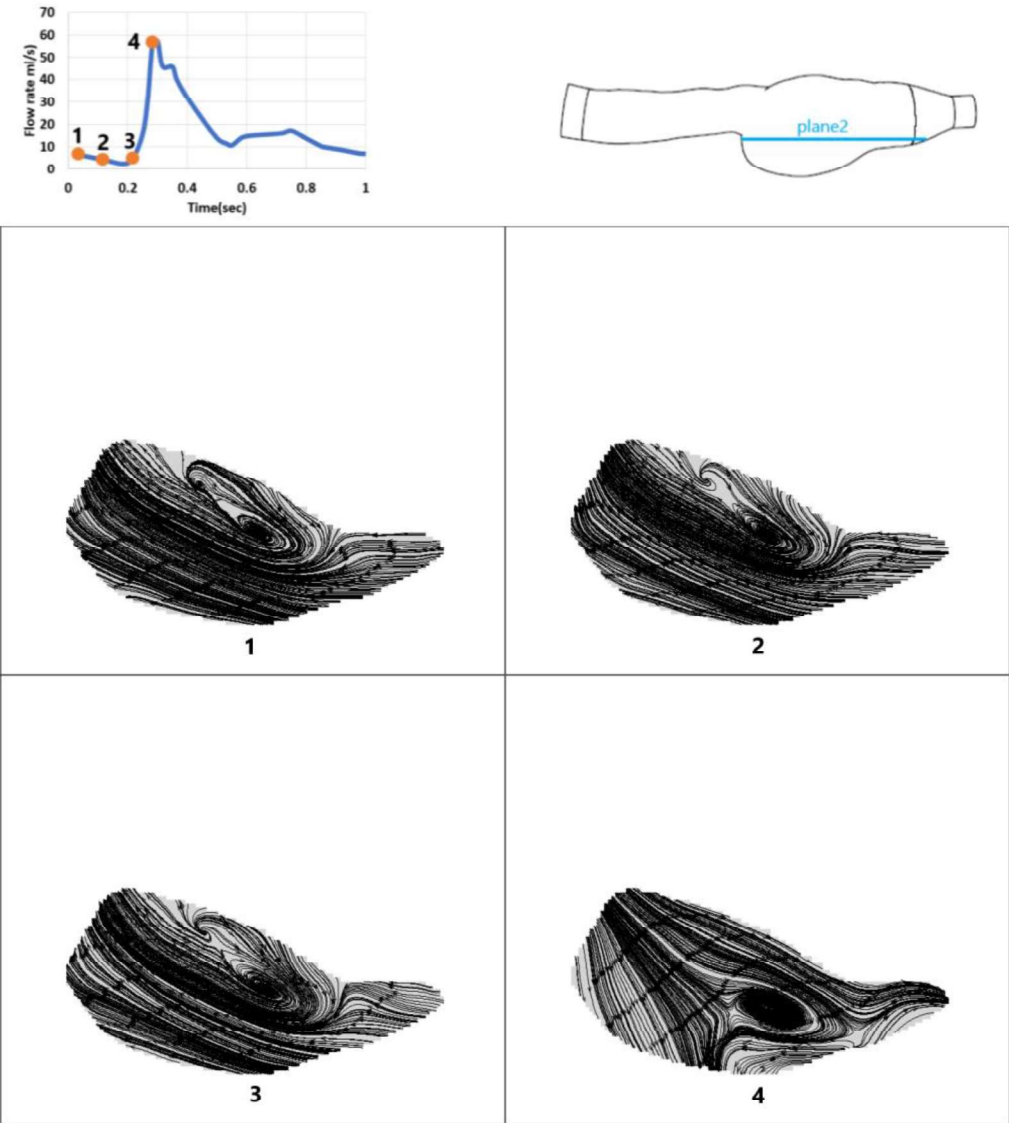


Figure 4.21. Streamline patterns at the acceleration part, PSM, plane #2

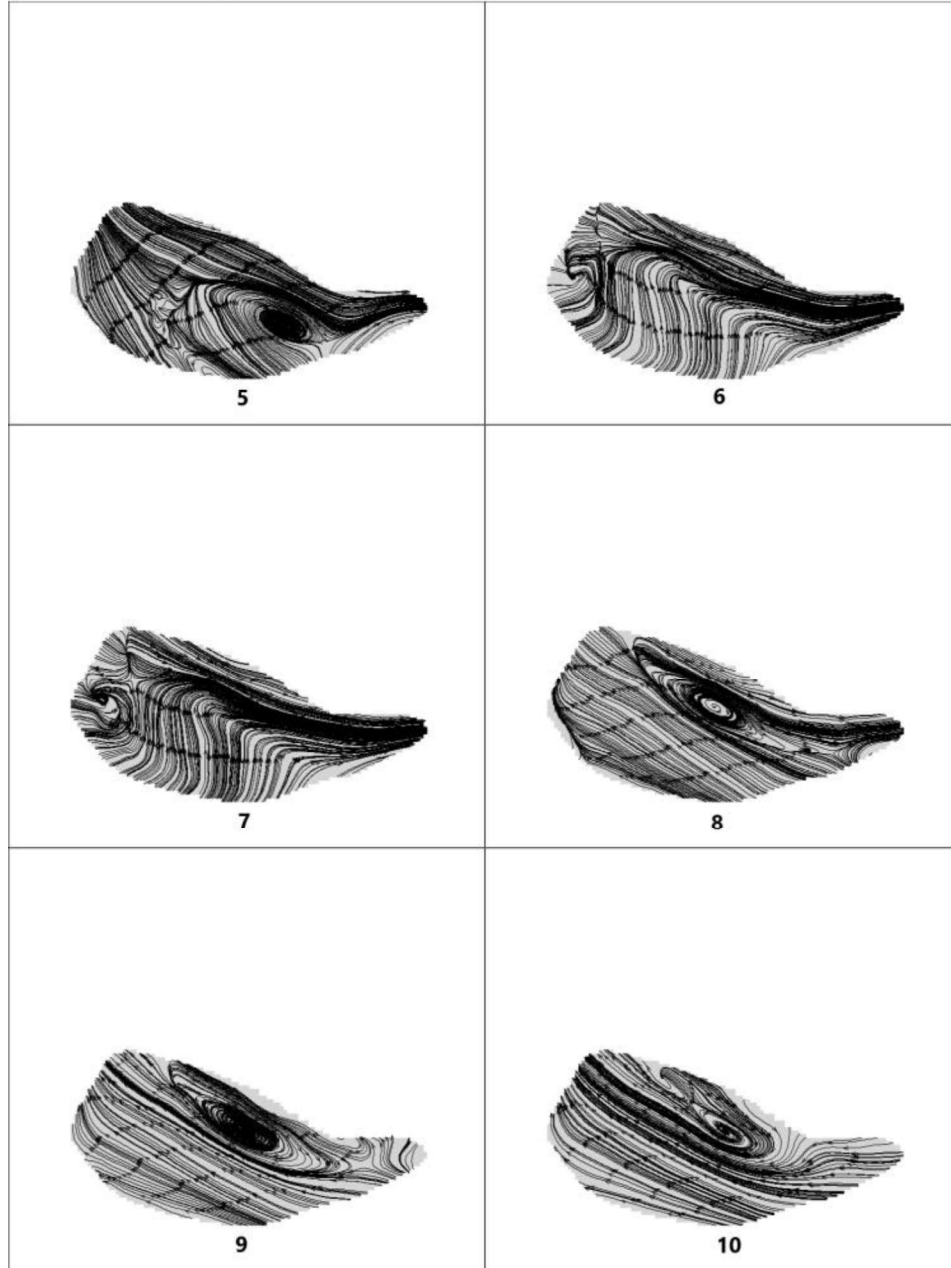
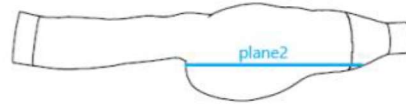
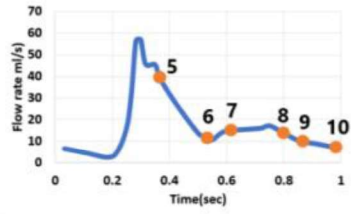


Figure 4.22. Streamline patterns at the deceleration part, PSM, plane #2

In phase 5, in the area where the left to right flow encounters the clockwise flow of the whirling region, complex streamline patterns are observed. In the area adjacent to the left wall, twisted flow forms appeared in phases 5 and 6.

Figure 4.23 and Figure 4.24 display the vorticity contours in these phases. Beginning from phase 7, the first sign of the vortex appears at the half of the bulge. This region increases in intensity and area until the end of the acceleration part of the next cycle.

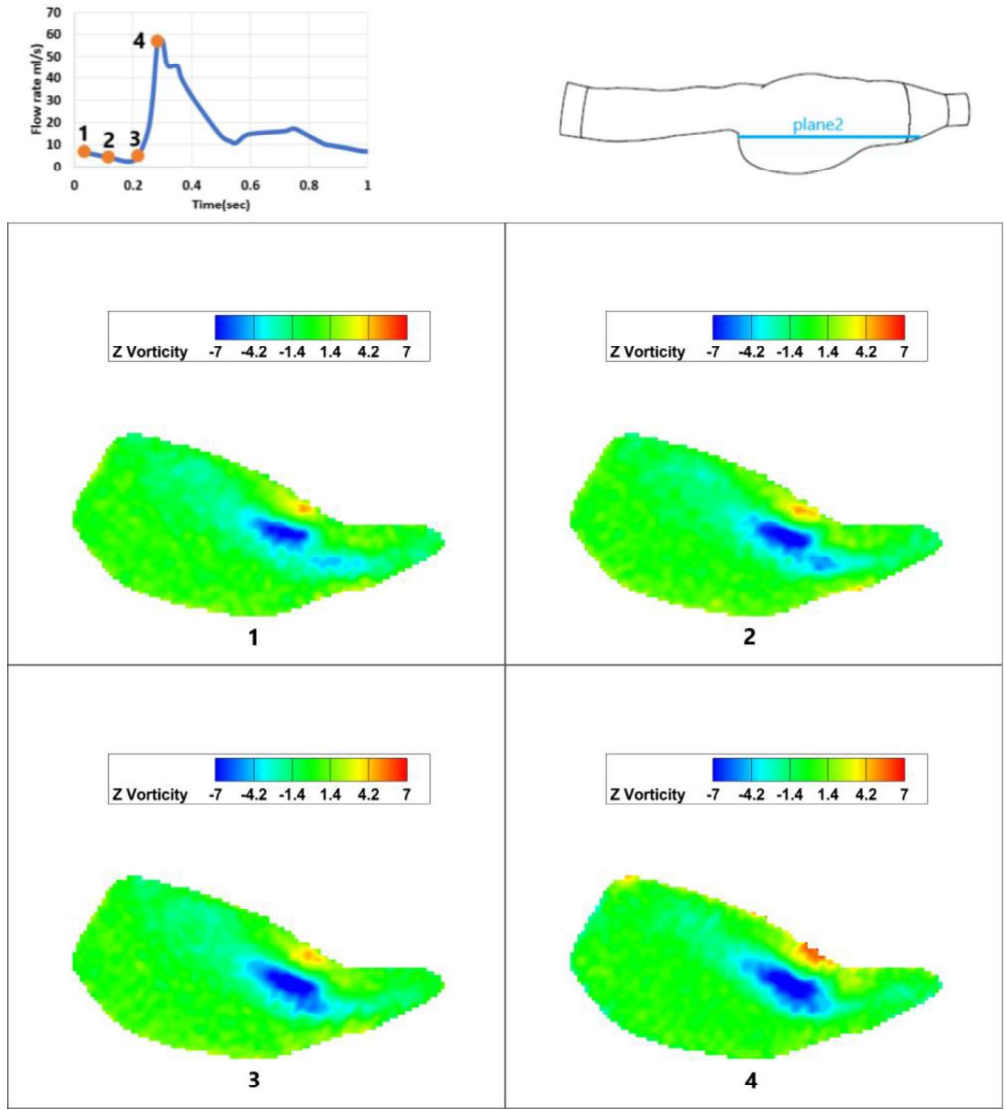


Figure 4.23. Vorticity contours at the acceleration part, PSM, plane #2

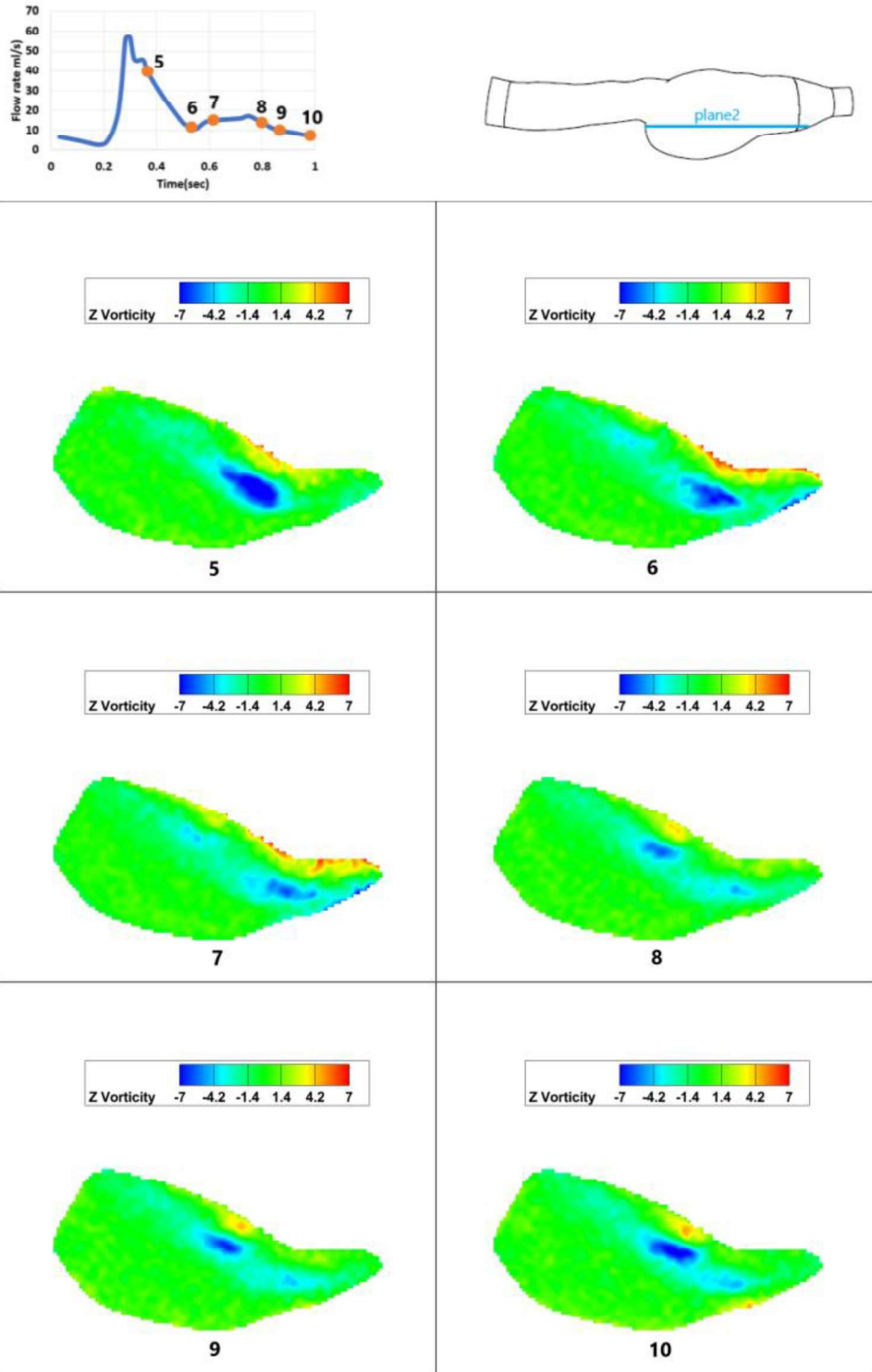


Figure 4.24. Vorticity contours at the deceleration part, PSM, plane #2

In the course of the deceleration part, the high vorticity section moves forward and, meanwhile, loses its intensity. In the close-to right wall section, this remains still from phase 8 to the next cycle's phase 2. In phase 3, this area attaches to the primary vortex initiated in the previous cycle. Another high vorticity flow in the opposite direction follows the current started at phase 7 attached to the anterior wall.

Figure 4.25 and Figure 4.26 show the swirling strength of the flow in these phases.

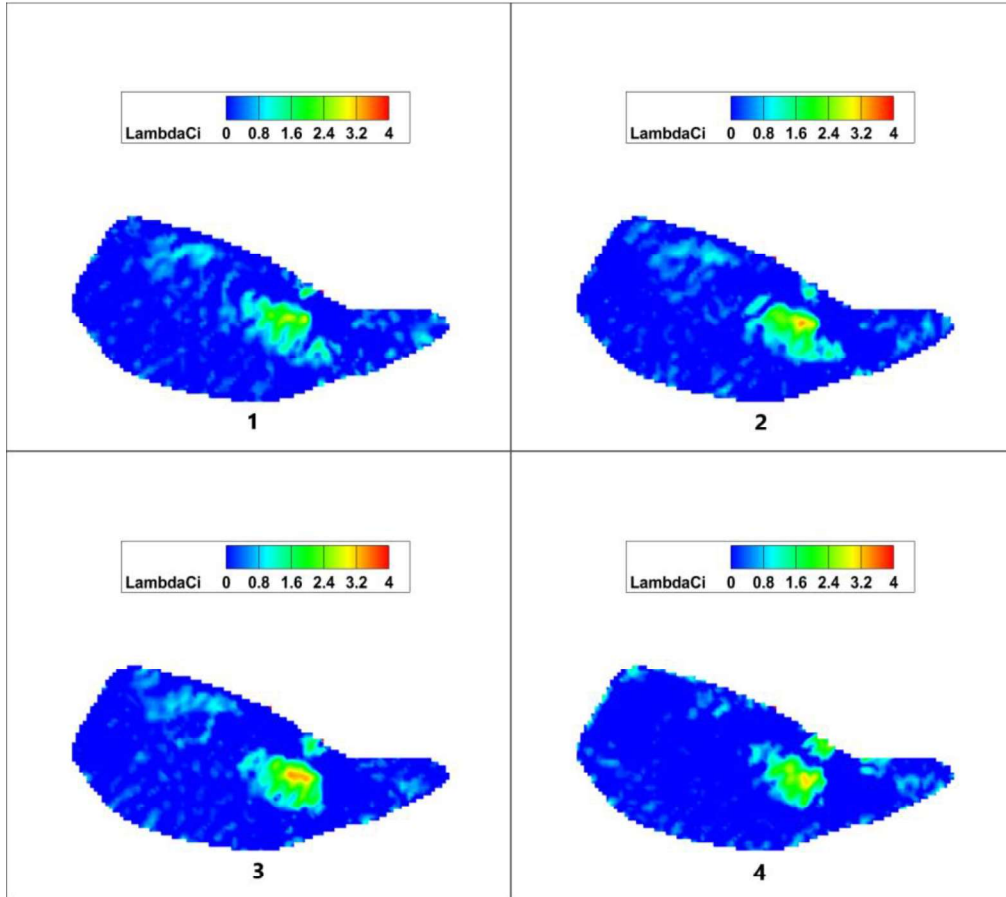
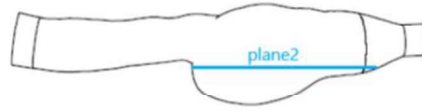
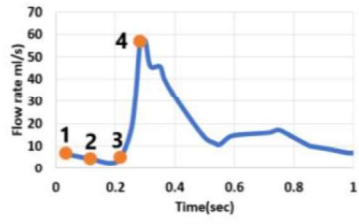


Figure 4.25. Swirling strength (λ_{ci}) at the acceleration part, PSM, plane #2

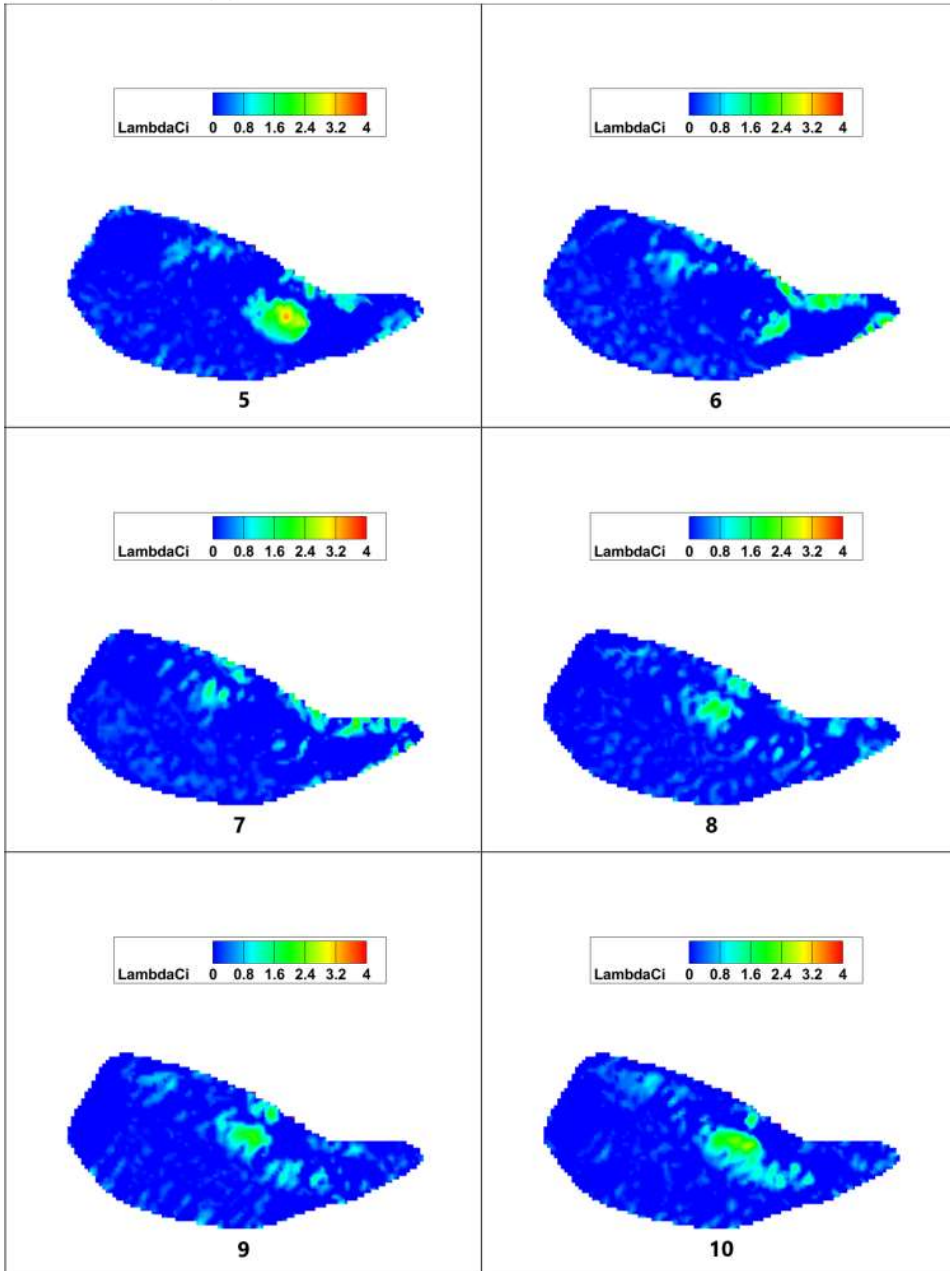
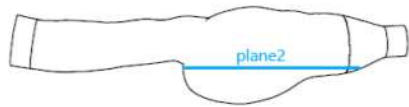
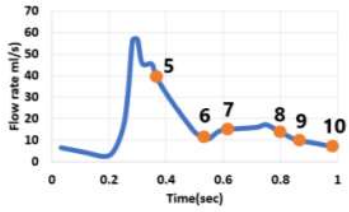


Figure 4.26. Swirling strength (λ_{ci}) at the deceleration part, PSM, plane #2

A rotary region of high swirling strength (λ_{ci}) initiates in phase7 in the half length of the bulge and close to the anterior wall. The intensity of this current's swirling strength increases along with moving forward. This flow almost vanishes when it reaches the bulge's right wall (phase6). Maximum swirling strength emerges at the primary vortex's core in phase5. Along with the primary vortex, consistent with the vorticity contours, another area of high swirling strength appears adjacent to the anterior wall.

4.2.3 Plane #3

The target area of plane #3 (Figure3.8.c) is smaller than the other planes. Figure 4.27 and Figure 4.28 display the axial velocity contours in the previous phases.

In the right corner of the anterior wall, an area of flow with a positive direction is surrounded by opposite direction flow. The positive direction flow increases in area and velocity during the acceleration part. The maximum axial velocity appears in phase 4. At the deceleration part, this area moves clockwise close to the wall region and decreases in velocity magnitude. Phase8 is when the opposite direction flow starts to dominate the site again.

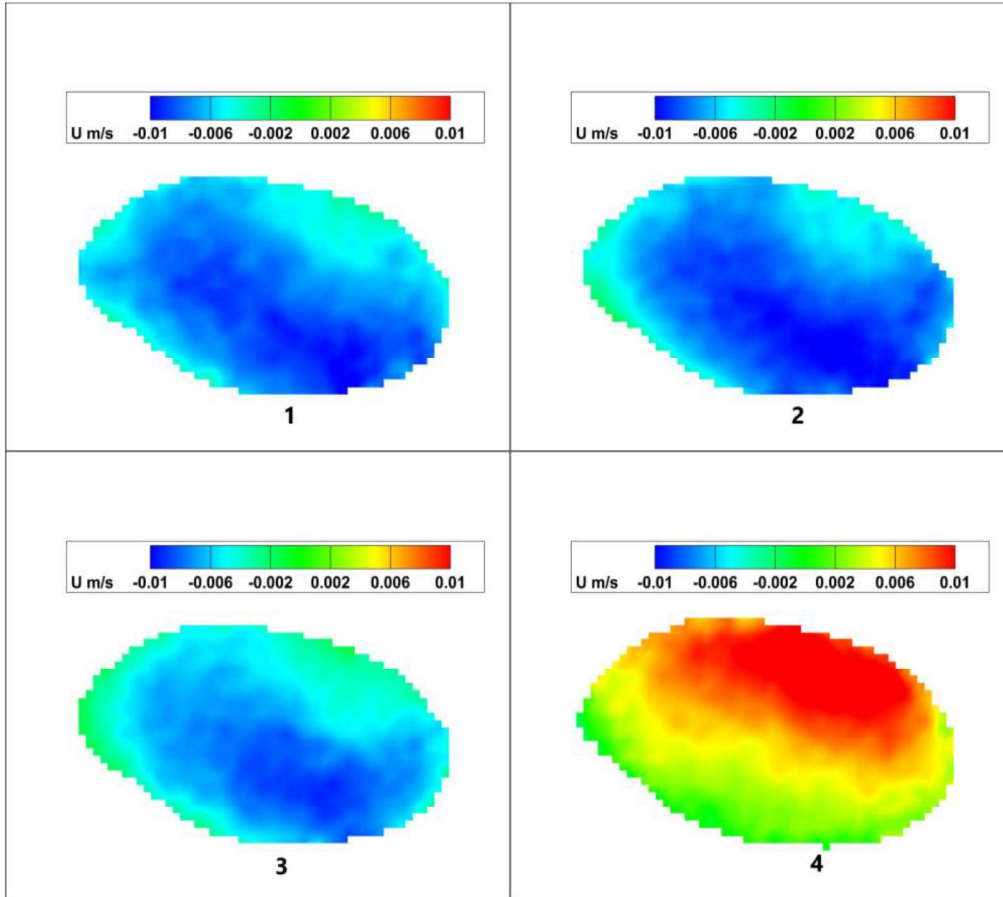
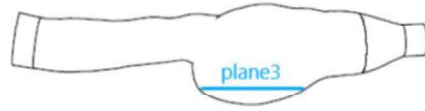
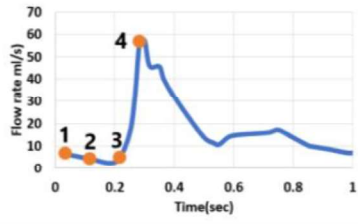


Figure 4.27. Axial velocity contours at the acceleration part, PSM, plane #3

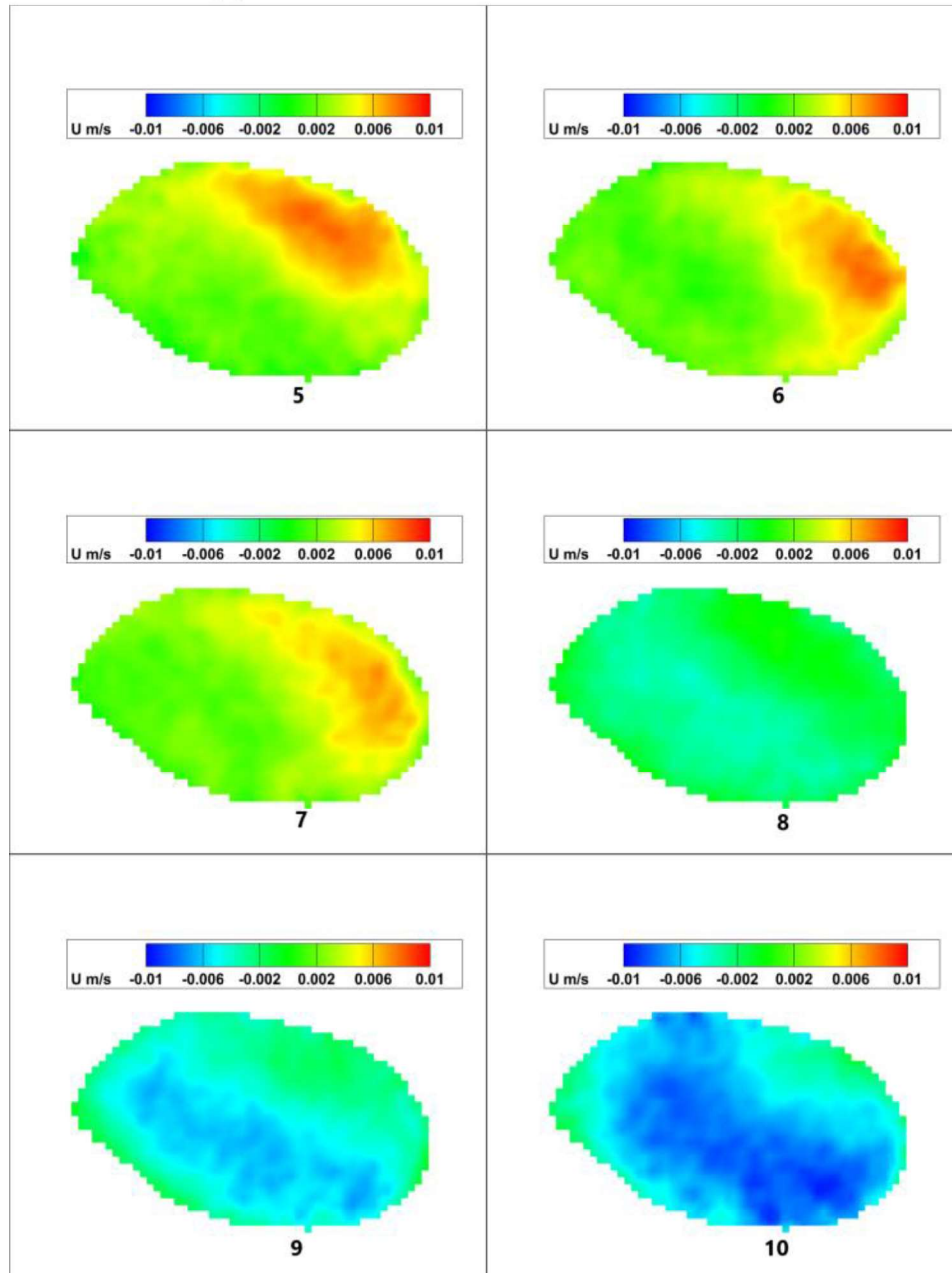
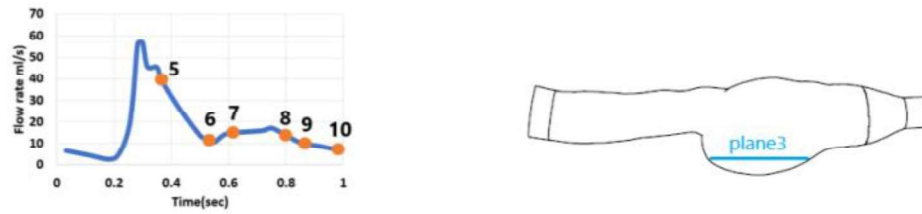


Figure 4.28. Axial velocity contours at the deceleration part, PSM, plane #3

Figure 4.29 and Figure 4.30 show the streamlines in the aimed instants. In the course of acceleration, backflow occurs. The current changes its direction starting from phase4. Flow orientation differs again in phase8, where complex streamline patterns happen close to the anterior wall region. No potential whirling from of stream is detected considering the streamline patterns.

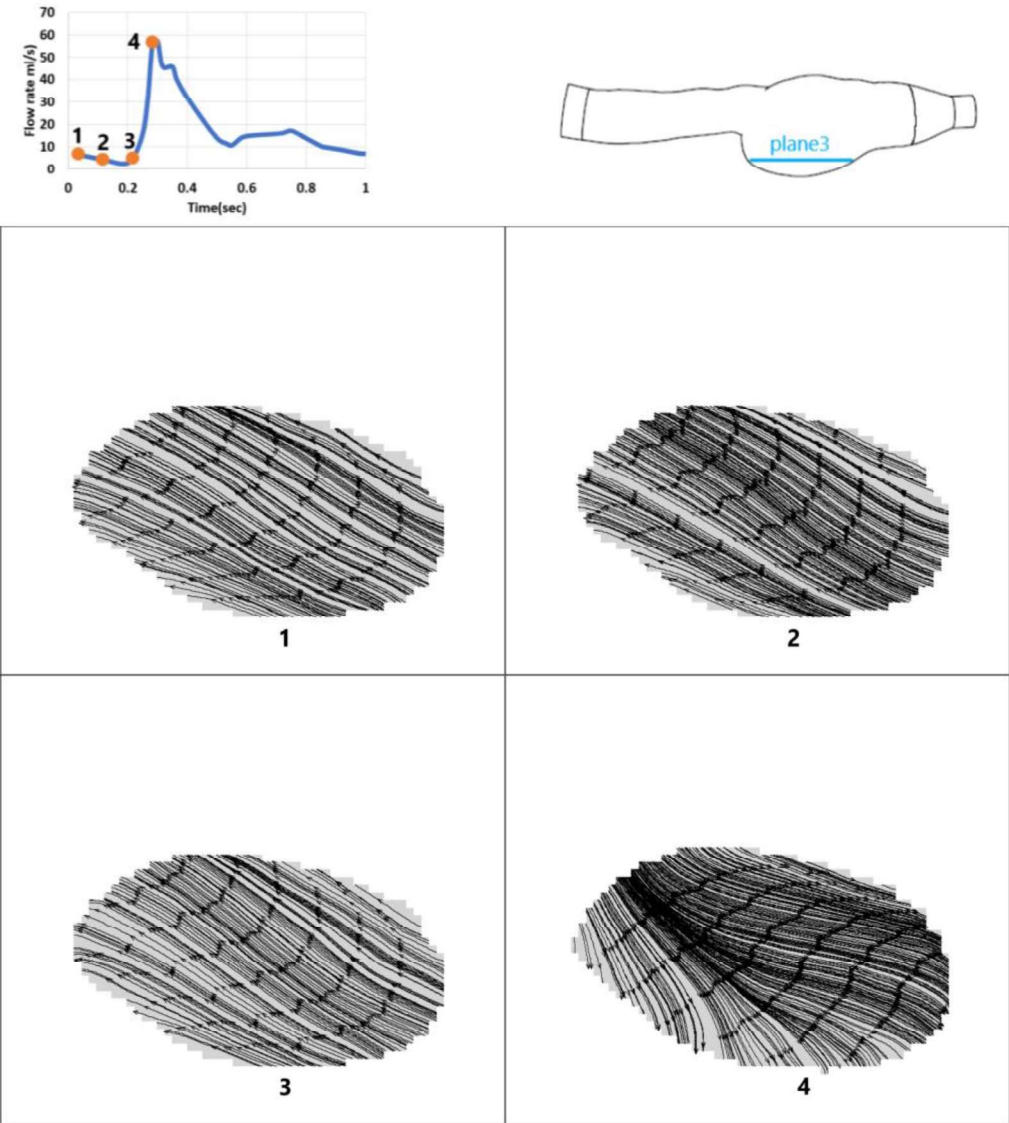


Figure 4.29. Streamline patterns at the acceleration part, PSM, plane #3

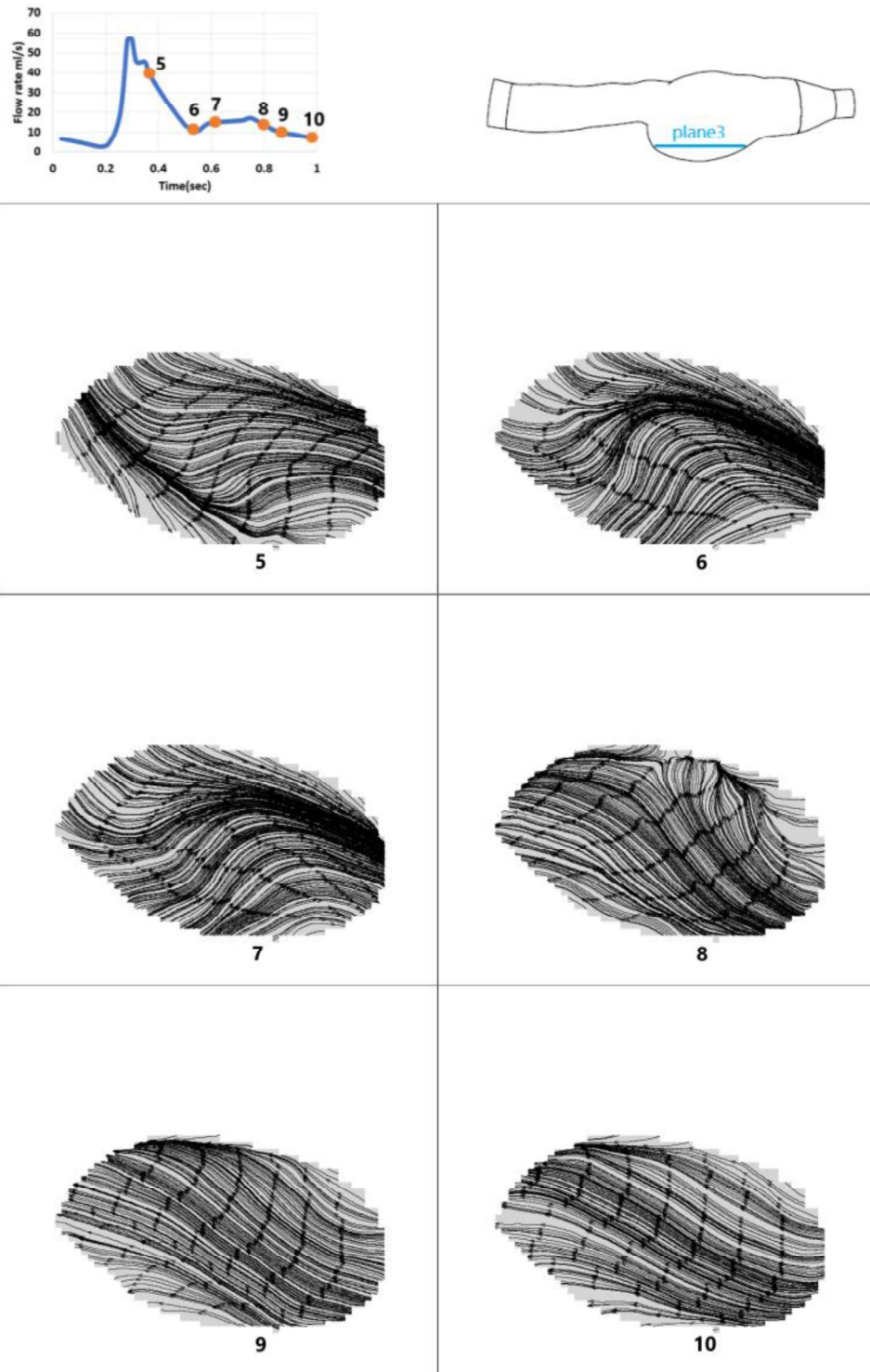


Figure 4.30. Streamline patterns at the acceleration part, PSM, plane #3

Figure 4.31 and Figure 4.32 show the vorticity contours of phases in the acceleration and deceleration part of the physiological flow, respectively. High vorticity currents appear at the reciprocal areas adjacent to the wall with opposite circulations. Consistent with streamline patterns, the vorticity directions changes in phase4. In the median area of the bulge, high vorticity regions appear, but there is no recordable evolution of these flow structures.

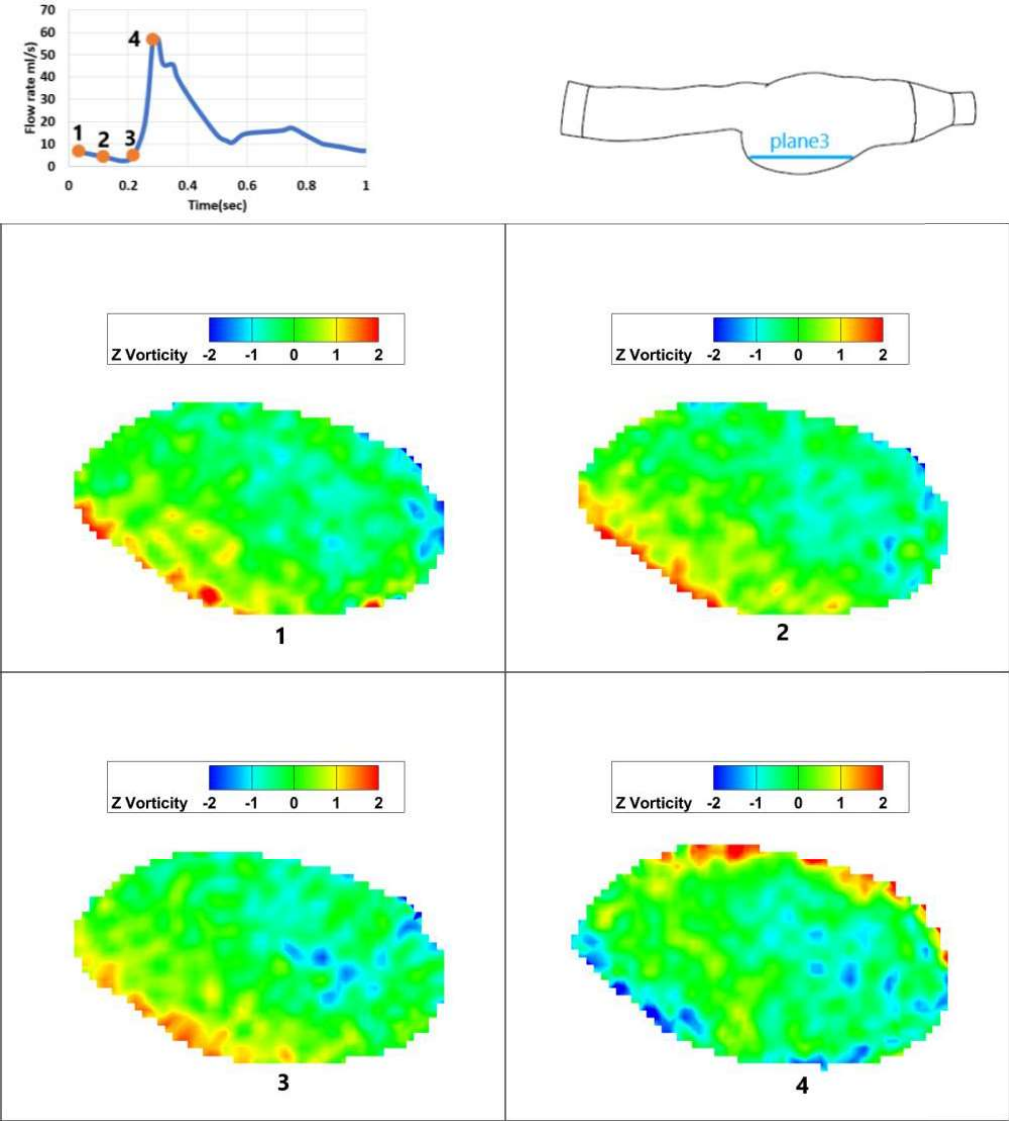


Figure 4.31. Vorticity contours at the acceleration part, PSM, plane #3

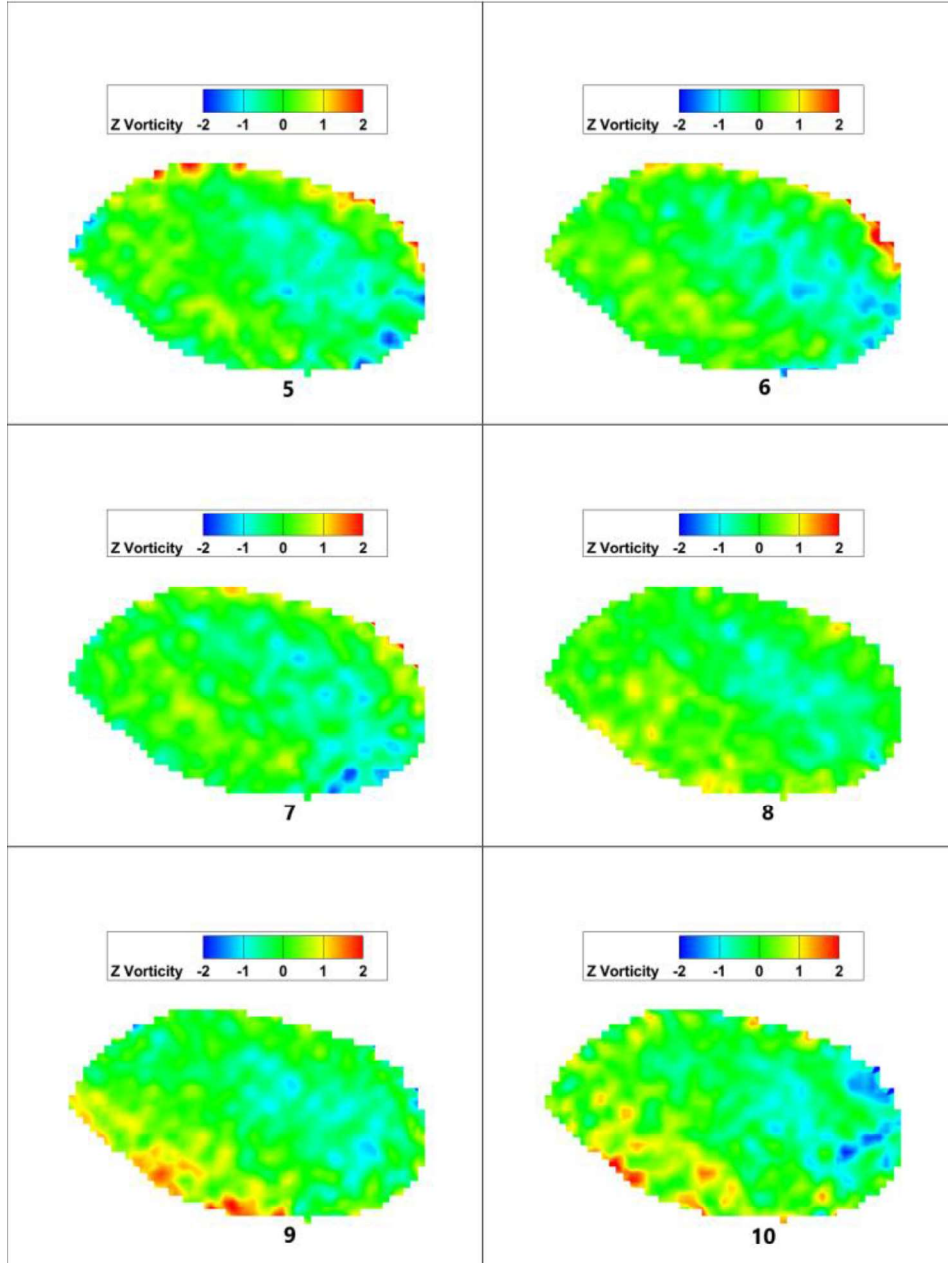
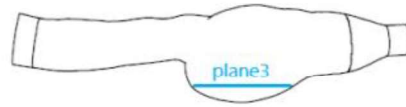
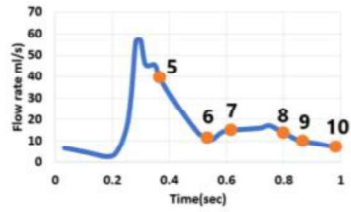


Figure 4.32. Vorticity contours at the deceleration part, PSM, plane #3

Maximum vorticity magnitudes at the median area occur in phases 3 and 4. Figure 4.33 and Figure 4.34 illustrate the swirling strength (λ_{ci}) contours in the instants. The case's general view indicates no solid emergence of a vortex ring. High swirling concentrations are consistent with vorticity magnitude contours. Maximum λ_{ci} occurs in phase4.

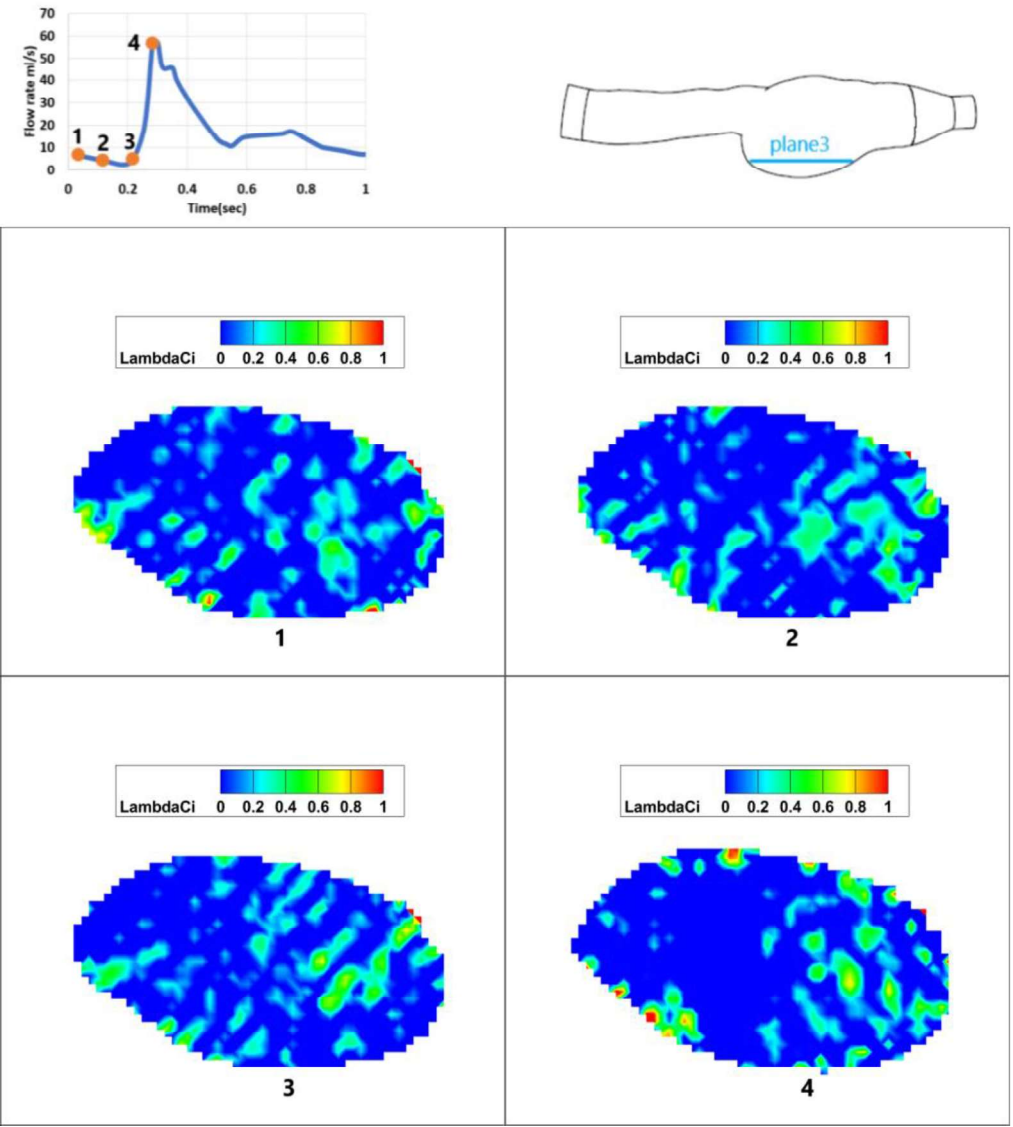


Figure 4.33. Swirling strength (λ_{ci}) at the acceleration part, PSM, plane #3

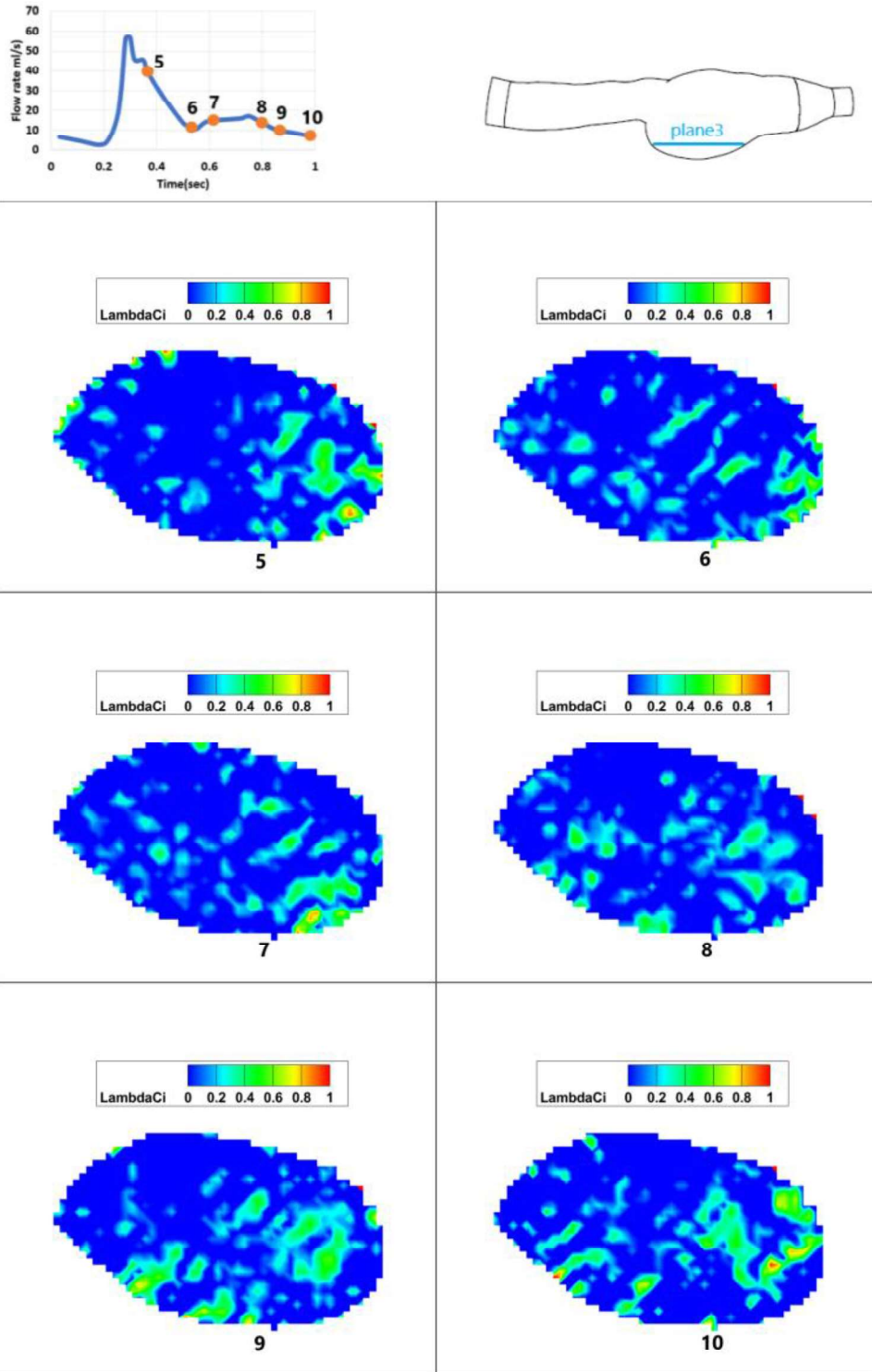


Figure 4.34. Swirling strength (λ_{ci}) at the deceleration part, PSM, plane #3

4.3 Comparison of flow characteristics is SM and PSM

The discussed indexes in both models indicate that the flow structure highly depends on the model geometry. The flow patterns are consistent with the previous studies illustrating the emergence of a particular vortex ring and the appearance of the secondary vortices in the collision area of this vortex ring with the distal end. On the other hand, the PSM has a unique geometry, provoking complex streamlines and flow patterns. Evaluating the target indexes in three planes in this model show that the velocity magnitudes are much smaller in the bulge portion. Initiation of vortices is detected in the midplane and second planes. The development of a potential vortex ring in the second plane is a remarkable incident and needs further investigation.

CHAPTER 5

CONCLUSION

This study aims to characterize the flow structure in two different abdominal aortic aneurysms models, simple and patient-specific geometry under physiological flows. An in-vitro setup is designed to simulate the physiological flows in the phantoms. The velocity fields in a single plane in the simple model and three planes in the patient-specific model are measured by using a 2D PIV device. Both of the models are produced by PDMS Sylgard 184. To match the refractive index of Sylgard 184, a mixture of water, glycerol, and urea is selected as the blood-mimicking fluid. This solution has viscosity and density close to the blood itself.

Velocity contours, streamline patterns, vorticity, and swirling strength (λ_{ci}) contours are presented based on the velocity fields. To analyze and calculate these parameters, Tecplot 360 software is used.

In each physiological case, ten different instants (four in acceleration and six in deceleration) are studied by averaging 100-200 image pairs at those instants.

The flow structures in the simple model are investigated in the physiological flow(case) with a period of one second and a flow rate range of 4-68 ml/s. Streamline, vorticity magnitudes, and swirling strength criterion reveals three vortices' appearance in a cycle. The primary one initiated at the acceleration part of the physiological pattern traveled through the bulge portion in the subsequent phases. This whirling flow form is followed by another vortical structure with high vorticity and swirling strength starting in the middle of the deceleration. The second one vanishes at the instant that the primary one hits the distal end. This collision divides the primary vortex into two small ones in opposite directions. The remainder of the primary vortex ring disappears in the deceleration of the next cycle.

The patient-specific model's simulated physiological flow has the same period as the case in SM. In but has a flow rate range of 2.5-57 ml/s. A primary vortex develops at the diverging point of the posterior wall at the beginning of the deceleration. This stream does not travel along the bulge and disappears at the end of the acceleration part of the next cycle in the first half of the bulge's length. An area of high swirling strength is visible through the rotation at the diverging part of the anterior wall.

Analyzing the results of vortex identification methods, it can be concluded that streamlining patterns can not be a precise approach for determining the vortexes. However, in most cases, the swirling strength criterion shows accurate results consistent with the potential areas in streamlines and vorticity contours.

5.1 Future work

Flow inside the aneurysm is a 3D flow. The most significant disadvantage of the 2D PIV is that it does not provide any information about the third component of the velocity vector. Stereoscopic PIV addresses this shortage by measuring the z component of the velocity vector in each plane by analyzing the flow in the thickness of the plane. This approach will help the study to have more information about the flow characteristics.

This research studies one plane in the simple model and three in the patient-specific model. However, the flow structure in other planes may carry vital characteristics, especially in the patient-specific model. Hence, alternative planes of interest could be added to the experimental matrices.

Many studies have reported a significant effect of non-Newtonian behavior on the flow structure in AAA. Experiments with the same properties could be conducted with a non-Newtonian fluid in both models to study this effect. 2 w% additives of XG to the employed blood mimicking fluid simulate the non-Newtonian property of the blood.

REFERENCES

1. Boyd AJ, Kuhn DCS, Lozowy RJ, Kulbisky GP (2016) Low wall shear stress predominates at sites of abdominal aortic aneurysm rupture. *J Vasc Surg* 63:1613–1619. <https://doi.org/10.1016/J.JVS.2015.01.040>
2. Drake RL, Vogl AW, Adam WMM (2020) *Gray's Anatomy for Students*
3. Tortora GJ, Derrickson B *Principles of anatomy & physiology*. 1200
4. Iaizzo PA (2005) Handbook of cardiac anatomy, physiology, and devices. *Handb Card Anatomy, Physiol Devices* 1–469. <https://doi.org/10.1007/978-1-59259-835-9>
5. Sochi T (2013) *Non-Newtonian Rheology in Blood Circulation*
6. Nader E, Skinner S, Romana M, et al (2019) Blood rheology: Key parameters, impact on blood flow, role in sickle cell disease and effects of exercise. *Front Physiol* 10:1329. <https://doi.org/10.3389/FPHYS.2019.01329/BIBTEX>
7. Connes P, Lamarre Y, Hardy-Dessources MD, et al (2013) Decreased hematocrit-to-viscosity ratio and increased lactate dehydrogenase level in patients with sickle cell anemia and recurrent leg ulcers. *PLoS One* 8:. <https://doi.org/10.1371/JOURNAL.PONE.0079680>
8. J W (2018) On the Rheological Properties of Human Blood. *Res Med Eng Sci* 6:. <https://doi.org/10.31031/RMES.2018.06.000644>
9. Perktold K, Karner G, Leuprecht A, Hofer M (1999) Influence of Non-newtonian Flow Behavior on Local Hemodynamics. *ZAMM - J Appl Math Mech / Zeitschrift für Angew Math und Mech* 79:187–190. <https://doi.org/10.1002/ZAMM.19990791349>
10. Tucker WD, Arora Y, Mahajan K (2021) *Anatomy, Blood Vessels*. StatPearls
11. (PDF) Abdominal aortic aneurysm: A comprehensive review.

https://www.researchgate.net/publication/51079995_Abdominal_aortic_aneurysm_A_comprehensive_review. Accessed 7 Jul 2022

12. Singh K, Bønaa KH, Jacobsen BK, et al (2001) Prevalence of and risk factors for abdominal aortic aneurysms in a population-based study : The Tromsø Study. *Am J Epidemiol* 154:236–244. <https://doi.org/10.1093/AJE/154.3.236>
13. Pistolese GR, Ippoliti A, Di Giulio L, et al (2003) Clinical practice. Small abdominal aortic aneurysms. *N Engl J Med* 348:78–83. <https://doi.org/10.1056/NEJMCP012641>
14. Wright RK (1991) The Epidemiologic Necropsy for Abdominal Aortic Aneurysm. *JAMA J Am Med Assoc* 266:1217–1218. <https://doi.org/10.1001/jama.1991.03470090051025>
15. Owens DK, Davidson KW, Krist AH, et al (2019) Screening for Abdominal Aortic Aneurysm: US Preventive Services Task Force Recommendation Statement. *JAMA - J Am Med Assoc* 322:2211–2218. <https://doi.org/10.1001/JAMA.2019.18928>
16. Chervu A, Clagett GP, Valentine RJ, et al (1995) Role of physical examination in detection of abdominal aortic aneurysms. *Surgery* 117:454–457. [https://doi.org/10.1016/S0039-6060\(05\)80067-4](https://doi.org/10.1016/S0039-6060(05)80067-4)
17. Wanhainen A, Verzini F, Van Herzelee I, et al (2019) Editor’s Choice – European Society for Vascular Surgery (ESVS) 2019 Clinical Practice Guidelines on the Management of Abdominal Aorto-iliac Artery Aneurysms. *Eur J Vasc Endovasc Surg* 57:8–93. <https://doi.org/10.1016/J.EJVS.2018.09.020>
18. Yazdi SG, Geoghegan PH, Docherty PD, et al (2018) A Review of Arterial Phantom Fabrication Methods for Flow Measurement Using PIV Techniques. *Ann Biomed Eng* 2018 46:11 46:1697–1721. <https://doi.org/10.1007/S10439-018-2085-8>

19. Kim GM, Lee SJ, Kim CL (2021) Assessment of the Physical, Mechanical, and Tribological Properties of PDMS Thin Films Based on Different Curing Conditions. *Materials (Basel)* 14:. <https://doi.org/10.3390/MA14164489>
20. Poepping TL, Rankin RN, Holdsworth DW (2010) Flow patterns in carotid bifurcation models using pulsed Doppler ultrasound: effect of concentric vs. eccentric stenosis on turbulence and recirculation. *Ultrasound Med Biol* 36:1125–1134. <https://doi.org/10.1016/J.ULTRASMEDBIO.2010.02.005>
21. Geoghegan PH, Buchmann NA, Soria J, Jermy MC (2013) Time-resolved PIV measurements of the flow field in a stenosed, compliant arterial model. *Exp Fluids* 54:. <https://doi.org/10.1007/S00348-013-1528-0>
22. Yousif MY, Holdsworth DW, Poepping TL (2011) A blood-mimicking fluid for particle image velocimetry with silicone vascular models. *Exp Fluids* 50:769–774. <https://doi.org/10.1007/S00348-010-0958-1/FIGURES/4>
23. Prajzler V, Nekvindova P, Spirkova J, Novotny M (2017) The evaluation of the refractive indices of bulk and thick polydimethylsiloxane and polydimethyl-diphenylsiloxane elastomers by the prism coupling technique. *J Mater Sci Mater Electron* 28:7951–7961. <https://doi.org/10.1007/S10854-017-6498-1>
24. MAYER GA (1964) Blood Viscosity in Healthy Subjects and Patients with Coronary Heart Disease. *Can Med Assoc J* 91:951
25. Rosenson RS, Uretz E (1994) Blood viscosity values and biochemical correlates in healthy adults. *Atherosclerosis* 109:265. [https://doi.org/10.1016/0021-9150\(94\)94059-2](https://doi.org/10.1016/0021-9150(94)94059-2)
26. Bai K, Katz J (2014) On the refractive index of sodium iodide solutions for index matching in PIV. *Exp Fluids* 55:1–6. <https://doi.org/10.1007/S00348-014-1704-X/FIGURES/3>
27. Brindise MC, Busse MM, Vlachos PP (2018) Density- and viscosity-matched

- Newtonian and non-Newtonian blood-analog solutions with PDMS refractive index. *Exp Fluids* 59:1–8. <https://doi.org/10.1007/S00348-018-2629-6>/FIGURES/4
28. Ramnarine K V., Nassiri DK, Hoskins PR, Lubbers J (1998) Validation of a New Blood-Mimicking Fluid for Use in Doppler Flow Test Objects. *Ultrasound Med Biol* 24:451–459. [https://doi.org/10.1016/S0301-5629\(97\)00277-9](https://doi.org/10.1016/S0301-5629(97)00277-9)
 29. Guo B, Ghalambor A (2005) Transportation. *Nat Gas Eng Handb* 219–262. <https://doi.org/10.1016/B978-1-933762-41-8.50018-6>
 30. Doutel E, Galindo-Rosales FJ, Campo-Deaño L (2021) Hemodynamics challenges for the navigation of medical microbots for the treatment of CVDs. *Materials (Basel)* 14:. <https://doi.org/10.3390/MA14237402>
 31. Stalder AF, Frydrychowicz A, Russe MF, et al (2011) Assessment of flow instabilities in the healthy aorta using flow-sensitive MRI. *J Magn Reson Imaging* 33:839–846. <https://doi.org/10.1002/JMRI.22512>
 32. San O, Staples AE (2012) An improved model for reduced-order physiological fluid flows. *J Mech Med Biol* 12:. <https://doi.org/10.1142/S0219519411004666>
 33. Nitsche M (2006) Vortex Dynamics. *Encycl Math Phys Five-Volume Set* 390–399. <https://doi.org/10.1016/B0-12-512666-2/00254-6>
 34. JEong J, Hussain F (1995) On the identification of a vortex. *J Fluid Mech* 285:69–94. <https://doi.org/10.1017/S0022112095000462>
 35. 17.2: Galilean Invariance - Physics LibreTexts
 36. Holmen Vivianne Methods for Vortex Identification | LUP Student Papers
 37. Zhou J, Adrian RJ, Balachandar S, Kendall TM (1999) Mechanisms for generating coherent packets of hairpin vortices in channel flow. *J Fluid Mech*

387:353–396. <https://doi.org/10.1017/S002211209900467X>

38. Ku DN, Glagov S, Moore JE, Zarins CK (1989) Flow patterns in the abdominal aorta under simulated postprandial and exercise conditions: An experimental study. *J Vasc Surg* 9:309–316. [https://doi.org/10.1016/0741-5214\(89\)90051-7](https://doi.org/10.1016/0741-5214(89)90051-7)
39. Yu SCM (2000) Steady and pulsatile flow studies in Abdominal Aortic Aneurysm models using Particle Image Velocimetry. *Int J Heat Fluid Flow* 21:74–83. [https://doi.org/10.1016/S0142-727X\(99\)00058-2](https://doi.org/10.1016/S0142-727X(99)00058-2)
40. Fukushima T, Matsuzawa T, Homma T (1989) Visualization and finite element analysis of pulsatile flow in models of the abdominal aortic aneurysm. *Biorheology* 26:109–130. <https://doi.org/10.3233/BIR-1989-26203>
41. Stamatopoulos C, Papaharilaou Y, Mathioulakis DS, Katsamouris A (2010) Steady and unsteady flow within an axisymmetric tube dilatation. *Exp Therm Fluid Sci* 34:915–927. <https://doi.org/10.1016/J.EXPTHERMFLUSCI.2010.02.008>
42. Deplano V, Knapp Y, Bertrand E, Gaillard E (2007) Flow behaviour in an asymmetric compliant experimental model for abdominal aortic aneurysm. *J Biomech* 40:2406–2413. <https://doi.org/10.1016/J.JBIOMECH.2006.11.017>
43. Geoghegan PH, Buchmann NA, Spence CJT, et al (2012) Fabrication of rigid and flexible refractive-index-matched flow phantoms for flow visualisation and optical flow measurements. *Exp Fluids* 52:1331–1347. <https://doi.org/10.1007/S00348-011-1258-0>
44. Hunt JCR, Wray AA, Moin P, et al (1988) eddies, streams, and convergence zones in turbulent flows. *Stud Turbul Using Numer Simul Databases*, 2 Proc 1988 Summer Progr